THE UNIVERSITY OF
WARWICK

University of Warwick institutional repository: http://go.warwick.ac.uk/wrap

A Thesis Submitted for the Degree of PhD at the University of Warwick

http://go.warwick.ac.uk/wrap/34612

This thesis is made available online and is protected by original copyright.

Please scroll down to view the document itself.

Please refer to the repository record for this item for information to help you to cite it. Our policy information is available from the repository home page.

Surface and Interface Structural Studies using Medium Energy Ion Scattering

by

Daniel Crispin Sheppard

Thesis

Submitted to the University of Warwick

for the degree of

Doctor of Philosophy

Department of Physics

September 2010

THE UNIVERSITY OF
WARWICK

Contents

List of Figures iv

Acknowledgments x

Declarations xii

Abstract xiv

Abbreviations xv

Chapter 1 Introduction 1

Chapter 2 Theoretical principles & experimental methodology 4

2.1 Introduction to medium energy ion scattering 4
2.2 Medium energy ion scattering - Background theory 5
    2.2.1 Collision kinematics 5
    2.2.2 Interaction potentials and the scattering cross-section 6
    2.2.3 Energy loss, straggling and neutralisation 9
    2.2.4 Shadowing and blocking 12
2.3 Simulating MEIS blocking curves 15
2.4 Instrumentation 18
2.5 Surface structure determination 21
    2.5.1 Experiment-theory comparisons using reliability factors 21
    2.5.2 Optimising the structural model 22
2.6 Supplementary experimental techniques 23
    2.6.1 Low Energy Electron Diffraction (LEED) 23
    2.6.2 Auger Electron Spectroscopy (AES) 25

Chapter 3 The structure of the Cu(410)-O surface 27

3.1 Introduction 27

3.2 Experimental details 31
3.3 Results and discussion 33
3.4 Conclusions 45

Chapter 4 Methylthiolate induced lateral distortion on the Cu(100) surface 47
4.1 Introduction 47
4.2 Experimental details 50
4.3 Results and discussion 53
4.4 Conclusions 63

Chapter 5 Methylthiolate induced modification of the Au(111) surface 65
5.1 Introduction 65
5.2 Experimental details 68
5.3 Results and discussion 70
  5.3.1 Initial evaluation and yield calibration 70
  5.3.2 Modelling the Au(111)($\sqrt{3} \times \sqrt{3}$)R30°-CH_3S system 74
  5.3.3 General discussion 80
5.4 Conclusions 81

Chapter 6 Evidence for adsorbate-induced reconstruction via backscattered ion yields 82
6.1 Introduction 82
6.2 Alanine on Cu(110) 82
  6.2.1 Introduction 82
  6.2.2 Experimental details 85
  6.2.3 Results and discussion 87
  6.2.4 Conclusions 92
6.3 Methylthiolate induced reconstruction on the Pd(111) surface 92
  6.3.1 Introduction 92
  6.3.2 Experimental details 93
  6.3.3 Results and discussion 95
  6.3.4 Conclusions 97

Chapter 7 Concluding remarks 98

List of Figures

2.1 Figure shows the binary collision of a moving particle of mass m_1 with a stationary one of mass m_2. This can be used to model the interaction of an incident ion with a target nucleus. 6

2.2 Graph shows the dependence of the final ion energy on the scattering angle, for the scattering of 100 keV H^+ and He^+ ions by a range of elemental targets. Noteworthy are the greater separation of the final energies of the heavier He^+ ions for different targets, and a greater energy separation at high scattering angles for both ion types. 7

2.3 Diagram shows the trajectory of an ion backscattered at depth d in a target material. 10

2.4 The fraction of emergent projectiles positively ionised as a function of emerging projectile energy for H^+ and He^+ ions incident on any target material is shown in graphical form, based on the empirical formulae of Kido [18]. 11

2.5 Figure shows the trajectories of a beam of parallel ions incident on a target atom nucleus, and the resulting shadow cone of radius R_M as a function of the distance d. 13

2.6 Figure shows the shadowing and blocking effects for a beam of parallel ions incident on a single crystal surface. Shaded areas within the crystal represent regions of ion flux, highlighting the unshaded regions below the scattering atoms which receive zero flux. Shown in red are the shadow cones cast as surface atoms block the backscattered ions exiting the crystal. 14

2.7 The incidence and exit directions e^1 and e^2 for an ion backscattering from atom i, shown in red. This ion will suffer a series of small angle deviations in its incidence and exit trajectories due to interactions with other atoms, taken into account by a Monte-Carlo algorithm in the VEGAS code used for simulating MEIS blocking curves [22]. 16

2.8 The layout of the accelerator, beamline and ultra-high-vacuum (UHV) scattering and preparation chambers, which all together constitute the UK National MEIS facility at Daresbury Laboratory. 18

2.9 A 2D spectrum representative of those collected in MEIS, with a characteristic high intensity surface peak. These data were obtained via the scattering of 100 keV H^+ ions from a clean Au(111) surface. Integrating the signal over a narrow angle range (shown in green), or over energy for merely the surface peak (shown in red) results in the production of an energy cut or blocking curve, respectively. 20

2.10 A schematic diagram of a standard LEED apparatus where the dotted arrows show the path of the electrons and V_E is electron source filament potential. 25

3.1 Model of the Cu(410) surface shown in a perspective and a side-sectional view. The side-sectional view is annotated with the directions of the principal axes, major crystallographic directions and the atom row numbers as described in the text. The smaller red spheres represent O atoms, and the larger spheres the Cu atoms. 28

3.2 Side-sectional and perspective views of a Cu(100)($\sqrt{2} \times 2\sqrt{2}$)R45°-O model, with the smaller red spheres representing O atoms and the larger spheres the Cu atoms. 30

3.3 The six ion scattering geometries used in the MEIS experiment. The $\langle 110 \rangle$, $\langle 110 \rangle$ and $\langle 310 \rangle$ incidence directions illuminate 1, 2 and 3 (100)-type surface layers respectively in a bulk continuation surface. 32

3.4 Experimental 100 keV H^+ fixed-calibration blocking curves (grey squares) obtained from the Cu(410)-O surface in the six different incidence geometries shown in figure 3.3 with the results of a VEGAS simulation in which all Cu atoms are assumed to occupy ideal bulk-like sites. The O atoms are situated in 4-fold symmetric hollow sites at heights of 0.06 Å and 0.65 Å at the step and terrace sites respectively (see 'Bulk' column in table 3.1). 34

3.5 Experimental 100 keV H^+ fixed-calibration blocking curves (grey squares) obtained from the Cu(410)-O surface in the six different incidence geometries shown in figure 3.3 with the results of a series of VEGAS simulations based on the LJ1, LJ2 and DFT models proposed in the recent combined SXRD/DFT study [55] (see table 3.1 for the structural parameters associated with these models). 38

3.6 Experimental 100 keV H^+ fixed-calibration blocking curves (grey squares) obtained from the Cu(410)-O surface in the six different incidence geometries shown in figure 3.3 with the results of a VEGAS simulation of the best-fit structure (see table 3.1 for the associated structural parameter values). 41

3.7 Experimental 100 keV H^+ blocking curves (grey squares) calibrated with freely optimised λ scaling factors and an overall 'skew' so as to better fit the results of a VEGAS simulation of the best-fit structure (compare with figure 3.6). 43

4.1 Plan view of the Cu(100)(2×2)-CH_3S surface, showing both the two pertinent azimuths and a superimposed square representing the (2×2) unit mesh. The short arrows highlight the proposed lateral outward radial displacements (shown here with a value $\Delta_{xy} = 0.15$ Å) of the Cu surface atoms surrounding the adsorbed methylthiolate species. 49

4.2 Side views of the [010] and [011] azimuthal scattering planes of the Cu(100)(2×2)-CH_3S surface showing the ion incidence and major bulk blocking exit directions utilised in this medium energy ion scattering study. 52

4.3 Comparison of the experimental blocking curves for both the clean Cu(100) and Cu(100)(2×2)-CH_3S surfaces in the $[\bar{2}11]$ incidence geometry, with the results of various simulated models exploring the effects of surface relaxation, including both radial lateral movement (Δ_{xy}) and perpendicular movement (Δ_z) of the surface Cu atoms. 54

4.4 Comparison of the experimental blocking curves for both the clean Cu(100) and Cu(100)(2×2)-CH_3S surfaces in the $[\bar{1}00]$ incidence geometry, with the results of various simulated models exploring the effects of surface relaxation, including both radial lateral movement (Δ_{xy}) and perpendicular movement (Δ_z) of the surface Cu atoms. 56

4.5 Comparison of the experimental blocking curves for both the clean Cu(100) and Cu(100)(2×2)-CH_3S surfaces in the $[\bar{1}10]$ incidence geometry, with the results of various simulated models exploring the effects of surface relaxation, including both radial lateral movement (Δ_{xy}) and perpendicular movement (Δ_z) of the surface Cu atoms. 59

4.6 R-factor plots for the Δ_{xy} lateral shift, Δ_z perpendicular relaxation and surface vibrational amplitude set of parameters which were optimised using the IFFCO routine. The black squares represent the calculated R-factors as a function of different parameter values, and the red lines a 2nd order polynomial fit to these data, from which the error attached to each parameter can be estimated. The blue lines represent an asymmetric fit about the optimised parameter value. 62

5.1 Plan view of the surface and 2nd atomic layers of the $(22 \times \sqrt{3})$rect. surface reconstruction of the clean Au(111) surface, showing the smooth transition between 'fcc' and 'hcp' stacking along the long axis of the surface mesh. 67

5.2 Plan and side-section views of the ideal bulk-terminated Au(111) surface. Shaded in green is one of the sheets of atoms that lie in a scattering plane used in this experiment. The figure shows the $[\overline{1}\overline{1}0]$ and $[\overline{1}\overline{1}2]$ ion incidence directions used in this experiment, which correspond to nominal illuminations of only the 1st and both the 1st and 2nd outermost atomic layers respectively. Also shown are the ion exit directions along which major blocking occurs. 69

5.3 Experimental MEIS blocking curves from both the clean and $(\sqrt{3} \times \sqrt{3})$R30° thiolated Au(111) surfaces recorded with ions incident in the $[\overline{1}\overline{1}0]$ and $[\overline{1}\overline{1}2]$ directions (see figure 5.2). Also shown are the VEGAS simulated blocking curves for the clean Au(111) surface, which include the $(22 \times \sqrt{3})$rect. herringbone reconstruction, with the simulated results from the bulk-terminated (1×1) Au(111) surface added as a useful reference. 71

5.4 Plan and side views of the models used in this study to represent the AAM (Au-adatom-monothiolate) and AAD (Au-adatom-dithiolate) reconstructions suggested to occur in the Au(111)$(\sqrt{3} \times \sqrt{3})$R30°-$CH_3S$ surface phase. For the sake of clarity the Au adatoms are shaded in blue, and the Sulphur head-group atoms in green. The S-C bond angles shown in these models are schematic only; the actual orientations are not well-established. 75

5.5 A plan and side view of the Au(111) surface exploring the adsites considered in this study. Au adatoms situated in the fcc hollow sites, hcp hollow sites and bridge sites are shown. The positions of the three inequivalent bridge sites are indicated, the **a** site being the only one that lies within the scattering planes of the substrate atoms (with adatoms in the scattering plane shaded in blue). 77

5.6 Experimental blocking curves for the clean and methylthiolate covered Au(111) surfaces, together with the results of VEGAS simulations of the (1×1) unreconstructed surface, the herringbone reconstructed clean surface and a number of simulations of the Au(111)$(\sqrt{3} \times \sqrt{3})$R30°-$CH_3S$ surface based on the AAM and AAD models shown in figure 5.4. 78

6.1 Schematic plan view of the Cu(110)(3×2)-alaninate surface structure found to give the lowest total energy in DFT calculations by Rankin and Sholl [131]. The black spheres represent C atoms, the red spheres O atoms and the blue spheres N atoms. Also shown in green is the outline of the (3×2) unit cell. 84

6.2 A side view of the Cu(110) crystal, showing the scattering plane used in the experiment together with the two distinct ion incidence directions, namely the $[0\overline{1}\overline{1}]$ and $[\overline{2}\overline{1}1]$ directions, which illuminate the uppermost 1 and 2 atomic layers respectively. Also shown are the directions which lead to major blocking of the backscattered ions. 86

6.3 MEIS experimental blocking curves for 100 keV H^+ ions backscattered from the clean Cu(110) and Cu(110)(3×2)-alaninate surfaces. Blocking curves are included for ions incident in both the $[0\overline{1}\overline{1}]$ and $[\overline{2}\overline{1}1]$ directions, corresponding to a nominal illumination of 1 and 2 surface layers, respectively. Simulations for the relaxed and unrelaxed clean Cu(110) surfaces are also shown. 88

6.4 MEIS experimental blocking curves for 100 keV H^+ ions backscattered from the clean Cu(110) and Cu(110)(3×2)-alaninate surfaces. Blocking curves are included for ions incident in both the $[0\overline{1}\overline{1}]$ and $[\overline{2}\overline{1}1]$ directions, corresponding to a nominal illumination of 1 and 2 surface layers, respectively. Simulations of scattering from the DFT model proposed by Rankin & Sholl [131] and the relaxed and unrelaxed clean Cu(110) surfaces are also shown. 91

6.5 Plan and side views of a Pd(111) surface showing the incidence directions used in this investigation. Ions incident in the $[\overline{1}\overline{1}0]$ direction will nominally illuminate only the surface layer, whilst those incident along the $[\overline{1}\overline{1}\overline{2}]$ direction nominally illuminate the top two layers. The main outgoing directions and associated scattering angles along which backscattered ions experience atomic blocking are also shown. 94

6.6 The blocking curves resulting from the investigation of the clean and methylthiolate covered Pd(111) surfaces using MEIS, with 100 keV H^+ ions incident in two distinct directions, namely the $[\overline{1}\overline{1}0]$ and $[\overline{1}\overline{1}\overline{2}]$ directions. In both geometries the large increase in the scattering signal upon adsorption of the methylthiolate species is indicative of a significant reconstruction of the Pd surface layers. 96

Acknowledgments

Firstly, I must acknowledge and thank my supervisor Prof. Phil Woodruff, for giving me the opportunity to work with him and his group, here at the University of Warwick. His relaxed and calm style of supervision has made the last four years pass by in quite a stressless manner, and I feel truly privileged to have had such excellent scientific support and tutelage.

I am particularly indebted to the people involved with MEIS at Warwick who have aided me during this PhD: Dr Amanda Window, Dr Marc Walker, Dr Agenor Hentz da Silva Jr., Dr Gareth Parkinson and Rob Johnston. It was Gareth who 'showed me the ropes' during the first six months, and I thank him especially for being a good mate as well as a mentor. A special mention must also go to Agenor, who has been a great postdoc but has also become a cherished friend. Rob Johnston deserves special thanks for preparing all of the sources and samples (often at quite short notice!) needed for use at Daresbury. Without his tireless work for the group, I am certain nothing would ever have gotten done at all!

I must also acknowledge the support of the team at the UK National MEIS facility, Daresbury Laboratory: Dr Tim Noakes, Dr Paul Bailey and Paul Whitfield. They have had to deal with a somewhat demanding group, and I am grateful for their efforts to solve the countless experimental problems which have cropped up during the last four years, an unavoidable problem at a facility such as MEIS.

A general thank you to all of the people in the Surface Science group here at Warwick, a diverse and interesting group of people, many of whom I count as good friends. The 'cast', in (general) order of appearance: Chris McConville, Jim Robinson, Gavin, Tim, Paul, Stuart, Daryl, Phil King, Tsenolo, Anindita, Matt Brown, Jim Aldous, Eeyore, Louise, Dave, Matt Bradley, Chris Burrows, Sepehr, Wojciech, Matt Butchers, Priyanka, Liam, Ian, Nessa, Dan and Andrzej. I am especially grateful to my office mates Dave and Matt Bradley who kindly offered to proof read parts of this thesis.

Finally, I will say thank you to my immediate family: Mom, Dad and Marion. Their continued support and acceptance have lead me to this point; I will forever be thankful.

Declarations

This thesis is submitted to the University of Warwick for admission to the degree of Doctor of Philosophy. This thesis contains an account of my research carried out in the Department of Physics at the University of Warwick and at the UK national MEIS facility, Daresbury Laboratory, during the period of October 2006 to September 2010, under the supervision of Prof. D. P. Woodruff FRS. No part of the material presented in this thesis has been used, either wholly or in part, in an application submitted to this or any other university.

The experimental data presented in this thesis were obtained over the period June 2005 to January 2010, with the people responsible for the data collection listed below. Unless specifically stated otherwise, all data were reduced by the author. All of the analysis and interpretation pertaining to these data was undertaken by the author.

The experimental data presented in Chapter 3 were taken by Dr. G. S. Parkinson, Dr. A. Hentz, Dr. P. D. Quinn and Dr. M. A. Muñoz-Márquez, and reduced by Dr. G. S. Parkinson. The experimental data presented in Chapter 4 were obtained by the author with the aid of Dr. M. Walker. The experimental data presented in Chapter 5 were taken in part by the author with the assistance of Dr. A. J. Window and Dr. A. Hentz, and in part by Dr. G. S. Parkinson and Dr. P. D. Quinn. The data comprising the latter part were reduced by Dr. G. S. Parkinson. The experimental data presented in Chapter 6 , section 6.2 were taken by the author with the assistance of Dr. A. J. Window. The experimental data presented in Chapter 6, section 6.3 were collected by Dr. G. S. Parkinson and Dr. A. J. Window.

Daniel Crispin Sheppard

September 2010

Parts of this work have been published or are in preparation:

1. D. C. Sheppard, G. S. Parkinson, A. Hentz, P. D. Quinn, M. A. Muñoz-Márquez, D. P. Woodruff, P. Bailey, and T. C. Q. Noakes, *"Surface relaxation in Cu(410)-O: A medium energy ion scattering study"*, Surface Science 604, 788 – 796 (2010).
2. D. C. Sheppard, M. Walker, C. F. McConville, D. P. Woodruff, T. C. Q. Noakes, and P. Bailey, *"Thiolate-induced lateral distortion of the Cu(100) surface"*, Surface Science 604, 1727 – 1732 (2010).
3. D. C. Sheppard, G. S. Parkinson, A. Hentz, A. J. Window, P. D. Quinn, D. P. Woodruff, P. Bailey, and T. C. Q. Noakes, *"Medium energy ion scattering investigation of methylthiolate-induced modification of the Au(111) surface"*, *Submitted for publication.*

Additionally the author has contributed to the following publication during his PhD studies:

1. A. J. Window, A. Hentz, D. C. Sheppard, G. S. Parkinson, D. P. Woodruff, T. C. Q. Noakes, and P. Bailey, *"Silver sulphide growth on Ag(111): A medium energy ion scattering study"*, Surface Science 604, 1254 – 1260 (2010).

Abstract

The technique of medium energy ion scattering (MEIS) can be used to elucidate the structural details of surfaces, both in general terms and in a more qualitative manner, in order to help solve a number of outstanding uncertainties relating to the structures of a number of surface systems. MEIS, involving the back-scattering of light ions from a material of interest, in this case 100 keV H^+ ions from adsorbate covered single crystal metal surfaces, can potentially be a powerful tool for obtaining either depth-dependent compositional information or quantitative structural details.

MEIS has been used to study the surface relaxations at the Cu(410)-O stepped surface. The results have been compared to a number of models favoured by previous studies, and an optimisation of the structural parameters associated with the outermost Cu atoms was undertaken so as to determine the positions of these atoms to a reasonable degree of precision.

In this thesis, MEIS has also been used to probe the surface reconstructions triggered by the adsorption of the methylthiolate species on the Cu(100), Au(111) and Pd(111) surfaces. Methylthiolate is derived from the n-alkylthiol molecule methylthiol, the simplest molecule of a species which ubiquitously form so called self-assembled monolayers (SAMs) on single crystal metal surfaces. In the case of Cu(100), our study confirms the existence of a radial lateral distortion of the outermost Cu layer, and we quantify this distortion. For Au(111), two competing structural models for the methylthiolate overlayer have been proposed, namely the Au-adatom-monothiolate (AAM) and Au-adatom-dithiolate (AAD). MEIS has been used to compare these two models, and we find in favour of the AAD model. Additionally, evidence has been found for a significant reconstruction of the Pd(111) surface triggered by adsorption of methylthiolate.

We have carried out a MEIS investigation of the (3×2)-alaninate phase formed by adsorption of the chiral molecule alanine on Cu(110). Evidence is found for a small degree of lateral surface distortion.

Abbreviations

AAM	The Au-adatom-monothiolate model for thiolate induced reconstruction on the Au(111) surface
AAD	The Au-adatom-dithiolate model for thiolate induced reconstruction on the Au(111) surface
AES	Auger electron spectroscopy
DFT	Density functional theory
LEED	Low energy electron diffraction
MEIS	Medium energy ion scattering
ML	Monolayer
NEXAFS	Near-edge X-ray adsorption fine structure
NIXSW	Normal incidence X-ray standing waves
RBS	Rutherford backscattering
STM	Scanning-tunneling microscopy
SXRD	Surface X-ray diffraction
TEA	Toroidal electostatic analyser
UHV	Ultra-high vacuum

Chapter 1

Introduction

The structure of a crystalline material is of fundamental importance, as this structure plays a major role in determining the electronic and chemical properties of the material in question. At the surfaces of such crystals, however, the three dimensional periodicity of the bulk is lost, and as such the atomic structure in the surface region is in general different from that of the bulk. Many phenomena such as oxidation, heterogeneous catalysis, molecular self-assembly and corrosion take place at the surface, and these processes depend heavily on the structure of the surface region and the electronic and chemical properties that this structure influences. A major aim of surface science is to develop a predictive understanding of surface structure, and in turn develop an understanding of how this structure relates to surface properties. Surface science employs a wide armoury of experimental and theoretical techniques to probe surface structure, and the combined use of several such techniques to concentrate on a particular problem of interest has lead to insights being gained into ever more complex systems [1].

In this thesis the focus is on one surface science technique in particular, known as medium energy ion scattering (MEIS). This technique, a variant of the more common Rutherford backscattering (RBS) technique, was developed in the 1980s at the FOM-AMOLF institute, where it was primarily utilised to study the surface structure of clean metal crystals and semiconductor materials. In more recent times MEIS has been mainly used as a depth-dependent compositional probe of materials such as high-k dielectrics, studied extensively for use in the microelectronics industry. That being said, in this thesis MEIS has been used exclusively to gain not only qualitative but also quantitative insights into the structure of the near surface region of noble metal surfaces whose structure is modified by the presence of an adsorbed molecular species. The fact that MEIS is based on totally different physical principles than the diffraction-based techniques more commonly used in surface science makes information gained by MEIS an ideal complement to that obtained from other surface techniques.

The surface studies presented in this thesis can be broadly summarised as *adsorbate-induced* modifications of clean single crystal metal surfaces. The majority of the work in this thesis concerns the formation of self-assembled monolayers (SAMs) of n-alkylthiolates on a variety of clean metal surfaces. SAMs of this kind have been a major subject of scientific interest for the past two decades. These thiolates tend to form highly dense and stable bio-compatible structures which have great potential for use in a wide range of applications; to name but a few: chemical sensing, molecular recognition, nano-scale electronics and non-linear optical devices. Despite the fact that such systems have been the focus of many studies, fundamental questions remain concerning the structures which these systems adopt, and MEIS is an ideal technique for gaining insight into these structural details. In addition to the phenomenon of SAMs, other systems studied in this thesis include a stepped surface and the chiral molecule alanine adsorbed on Cu(110). The surface studies which comprise this thesis will be outlined subsequently.

In chapter 2 the background theory behind MEIS is laid out, which is then followed by a description of the general experimental methodology employed in the data gathering, reduction and analysis pertaining to the systems studied in this thesis. Also included are brief descriptions of the common surface science techniques of low energy electron diffraction (LEED) and Auger electron spectroscopy (AES) which have also been used in the work presented in the thesis.

Chapter 3 details a MEIS investigation of the Cu(410)-O stepped surface. There have been relatively few quantitative studies which have focused on the detailed atomic structure at the step sites, and some doubt remains regarding the structural details of this surface. The MEIS data have been initially compared to a range of existing surface structural models using a chi-square R-factor to objectively judge the quality of fit. Further analysis has been conducted in the form of a structural optimisation to uniquely determine the set of key structural parameters which best describe the data.

The structure of the interface formed between methylthiolate SAMs in the (2×2) phase and Cu(100) is the subject of chapter 4. Methylthiolate adsorbed on the Cu(111) surface triggers a pseudo-(100) reconstruction of the outermost layers, with this reconstruction characterised by a lattice spacing enlarged with respect to that of Cu(100). This has led to the suggestion of the presence of stresses in the outermost Cu layer of the Cu(100)(2×2)-CH_3S phase, which might result in localised strain. MEIS experiments have been performed in the hope of identifying whether such strain exists and so as to quantify this strain should it be found. The data do provide clear evidence of a local radial lateral distortion centred around the sulphur head-group bonded in the 4-fold coordinated hollow sites. Values have been found for the parameters which describe this surface distortion.

The high coverage $(\sqrt{3} \times \sqrt{3})R30^\circ$ phase formed by methylthiolate on Au(111) has been the subject of numerous theoretical and experimental studies. It is widely believed that the adsorbed thiolate induces a reconstruction of the Au(111) surface, but the exact nature of this reconstruction remains controversial. Two different models have been proposed, namely the Au-adatom-monothiolate (AAM) and the Au-adatom-dithiolate (AAD). However, as both models involve the same local adsorption site, diffraction techniques such as photoelectron diffraction and near-edge X-ray absorption fine structure (NEXAFS) have failed to distinguish these two models. A key difference between these two models, however, is the coverage of the Au adatoms which characterise the reconstruction. MEIS has been used as an ideal tool to probe the buried interface of this system, and distinguish between these two models, as related in chapter 5. The MEIS data clearly show the presence of an Au surface reconstruction, and despite a number of challenges in quantifying the information, this study finds in favour of the AAD model.

In chapter 6 the results of two additional studies using MEIS are presented, in which a lack of information in the literature regarding specific structural models has limited the conclusions to identifying only more general features of the surface structures. In the case of the chiral amino acid alanine on Cu(110), the data seem to indicate that outermost Cu layers are involved in a modest degree of lateral distortion, as had been proposed in the literature. For methylthiolate adsorbed on Pd(111), MEIS shows clear evidence for a substantial adsorbate-induced surface reconstruction. Unfortunately, due to the dearth of information concerning even the basic structural details of this phase, further insight cannot be achieved.

Chapter 2

Theoretical principles & experimental methodology

2.1 Introduction to medium energy ion scattering

The MEIS technique, first developed by researchers at the FOM-AMOLF institute in Amsterdam [2] in the 1980s, is a variant on the more well known Rutherford backscattering (RBS) method for probing material structure. The main difference between these techniques is the energies of the ions used to probe the material of interest, with $\sim 100\,\mathrm{keV}$ H^+ or He^+ ions used in MEIS as opposed to energies in the $1\,\mathrm{MeV}$ range for RBS.

In both techniques a beam of light ions is fired at a sample of interest with some of these ions being backscattered in the direction of an energy sensitive detector. The energies of the detected ions depend both on the mass of the atom from which they were scattered and the depth within the sample material at which this scattering event occurred, thus both techniques serve as depth-dependent compositional probes. The lower energies in MEIS, however, allow the use of a dispersive electrostatic analyser as opposed to the silicon barrier-detectors used in conventional RBS. This analyser has a much greater energy resolution, and the combined effect of this resolution enhancement and the greater electronic stopping of the medium energy ions results in a much greater depth resolution.

Both techniques, whilst not intrinsically surface specific, can be rendered so for single crystal samples by the alignment of the incident beam along a major crystallographic direction, such that the majority of the subsurface atoms become shadowed by the atoms in the near surface region. In the work presented in this thesis this shadowing effect is exploited both in the ingoing direction and the outgoing direction, the latter shadowing effect (more commonly called blocking for the sake of clarity) allowing the determination of the relative positions of the surface atoms.

Another related technique is LEIS (Low Energy Ion Scattering), although for ions in this energy range (typically a few keV), the interaction with the target material differs in a number of important ways. The large shadow cones cast at these energies give rise to an intrinsic surface specificity, but ion neutralisation effects, together with the fact that the ion/atom interaction potential is less well-understood, limit the accuracy of LEIS as a probe of surface structure. By contrast, the interaction potentials in MEIS are well known, enabling not only accurate determination of surface atomic positions but also allowing the scattering signal to be directly related to the number of atomic layers contributing to this scattering.

The remainder of this chapter will firstly be focused on the fundamental theory of medium energy ion scattering, after which the specific experimental details related to the work presented in this thesis will be given. At the end of the chapter a brief description is included of the standard surface science techniques of LEED (Low Energy Electron Diffraction) and AES (Auger Electron Spectroscopy). These have been used to aid in the characterisation of all of the surfaces which are investigated in this work.

2.2 Medium energy ion scattering - Background theory

2.2.1 Collision kinematics

One of the principal advantages of medium energy ion scattering (MEIS) is that the interaction between the ions and the nuclei of the target atoms is well known, and thus can be quantified. In fact, this interaction can be understood in terms of a binary collision between two free classical particles [3]. This is in part because of the large energies used in MEIS (ions with energies in the range $100 - 200\,\mathrm{keV}$), which means that both the momentum possessed by the incident ion, and the momentum transfer upon collision with the target nucleus is far greater than the quantum-mechanical uncertainty (due to Heisenberg) in the momentum. It is also the case that for light ions at these energies the associated De Broglie wavelength is far too short for the particles to manifest wave-like behaviour (such as diffraction) in their interactions with the target atoms. In addition, the time scale of the collision (in the order of 10^{-15} seconds) is far less than the typical thermal vibration period of the atoms (10^{-13}), thus the target nucleus can be effectively considered stationary. It is also the case that the local binding energy of the atom to the surrounding solid is so much smaller than the energy transfer associated with a scattering event that the target atom can be considered free.

Modelling the ion/atom interaction as a binary collision, one can derive, using the principles of the conservation of energy and momentum, the following equation, which

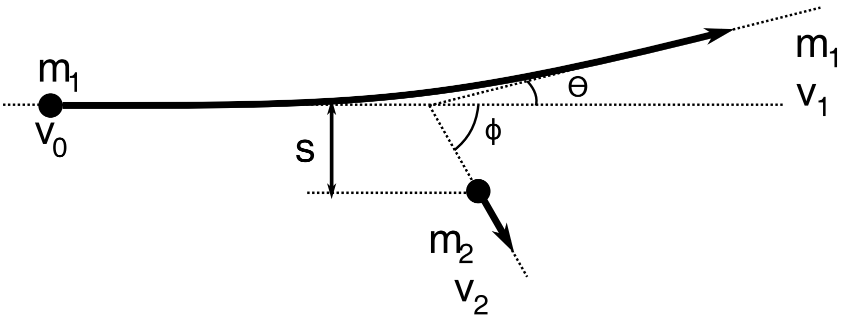

Figure 2.1: Figure shows the binary collision of a moving particle of mass m_1 with a stationary one of mass m_2. This can be used to model the interaction of an incident ion with a target nucleus.

describes the elastic energy loss suffered by the incident ion

$$\frac{E_1}{E_0} = k^2(\theta) = \left[\frac{(m_2^2 - m_1^2 \sin^2\theta)^{1/2} + m_1 \cos\theta}{m_1 + m_2}\right]^2 . \tag{2.1}$$

Here m_1 and m_2 are the mass of the ion and target nucleus, respectively, and E_0 and E_1 the energies of the ion before and after the binary collision. The scattering angle upon which the final ion energy depends is denoted θ (see figure 2.1). The ratio E_1/E_0 is most often referred to as the kinematic factor, k^2.

Figure 2.2 evinces the dependence of the final scattered ion energy on both the scattering angle and the mass of the target nucleus, for H^+ and He^+ ions initially at an energy of 100 keV. Notice how scattering from a range of target species of differing mass results in different final ion energies. Given a well defined mono-energetic beam of ions and a detector at a known angular position capable of detecting both the ions and their energies, one can determine the species of the scattering atom. This gives the MEIS technique its elemental specificity. Targets of similar mass are often difficult to resolve energetically, but switching to a heavier ion, or to a geometry with a higher scattering angle could potentially solve this problem.

2.2.2 Interaction potentials and the scattering cross-section

Using equation 2.1 from the previous section one can establish the final energy of the elastically scattered ions as a function of the scattering angle, but there is a lack of information concerning the intensity of the ions scattered through a given angle. For this one must determine the relationship between the scattering angle and the scattering cross-section, a relationship which can only be derived given an accurate knowledge of the

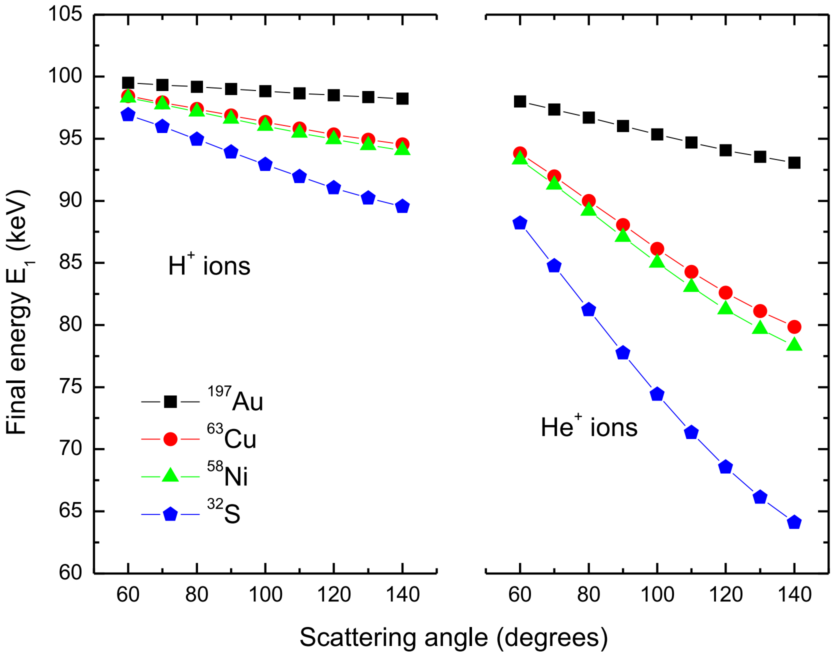

Figure 2.2: Graph shows the dependence of the final ion energy on the scattering angle, for the scattering of 100 keV H$^+$ and He$^+$ ions by a range of elemental targets. Noteworthy are the greater separation of the final energies of the heavier He$^+$ ions for different targets, and a greater energy separation at high scattering angles for both ion types.

ion/atom interaction potential. The remainder of this subsection concerns the scattering cross-section used in MEIS and the interaction potentials upon which it is based.

The interaction between the ion and the target nucleus is Coulombic, and in the simplest case this can be described using the bare Coulomb potential,

$$V(r) = \left(\frac{1}{4\pi\epsilon_0}\right)\left(\frac{Z_1 Z_2 e^2}{r}\right), \tag{2.2}$$

where Z_1 and Z_2 are the atomic numbers of the incident ion and target atom respectively, e being the elementary charge and r representing the distance between the target nucleus and the ion. Using such a potential, one can arrive at an analytical expression [4] for the scattering cross-section of a beam of particles of energy E, which in the case of the bare Coulomb potential is given as

$$\frac{\mathrm{d}\sigma_R}{\mathrm{d}\Omega} = \left(\frac{1}{4\pi\epsilon_0}\right)^2 \left(\frac{Z_1 Z_2 e^2}{4E}\right)^2 \left(\frac{1}{\sin^4(\theta/2)}\right). \tag{2.3}$$

Here $\mathrm{d}\sigma_R/\mathrm{d}\Omega$ is properly referred to as the *differential* cross-section, and its dependence on the scattering angle θ is that famously found empirically by Rutherford [5]. Unfortunately, this expression is an unsuitable one for the ion energies used in MEIS, for which the screening of the bare nuclear charge by the surrounding electron cloud [6] must be taken into account. A more accurate interaction potential which incorporates Coulombic screening must therefore be used to correctly describe the scattering process. Several such potentials have been developed; these take the general form

$$V(r) = \left(\frac{1}{4\pi\epsilon_0}\right)\frac{Z_1 Z_2 e^2}{r}\Phi\left(\frac{r}{a}\right), \tag{2.4}$$

where $\mathit{\Phi}(r/a)$ is the screening function, this function in effect reducing the bare Coulomb potential so as to account for the electronic screening. The parameter a is referred to as the Thomas-Fermi screening length, the value of which defines the range of the screening effects. Previous studies have assessed the applicability of several screening functions over a range of incident ion energies (e.g. [7]), with investigations which use ion energies and target materials typical to this thesis (100 keV H$^+$ ions incident on transition metal surfaces) most often using the screened Coulomb potential due to Molière [8], for which

$$\Phi\left(\frac{r}{a}\right) = \sum_{i=1}^{3} \alpha_i e^{-\beta_i r/a}, \tag{2.5}$$

with $\{\alpha_i\} = \{0.10, 0.55, 0.35\}$, and $\{\beta_i\} = \{6.0, 1.2, 0.3\}$. Firsov [9] has demonstrated that the Thomas-Fermi screening length in the case of a partially ionised projectile (see section 2.2.3) can be obtained thus

$$a = 0.88534 a_0 \left(Z_1^{1/2} Z_2^{1/2}\right)^{-2/3}. \tag{2.6}$$

Here a_0 is the Bohr radius (0.529 Å). The 'Rutherford' differential cross-section expressed in equation 2.3 can be corrected for the electronic screening of the Molière potential by the inclusion of a suitable prefactor F, with the correction factor proposed by L'Ecuyer et al. [10] found to appropriately describe experimentally derived results in the medium energy ion regime [11]. This screening factor is expressed as follows

$$F = 1 - \frac{0.042 Z_1 Z_2^{4/3}}{E\,[keV]}. \tag{2.7}$$

Thus the final equation for the differential cross-section is given below as

$$\frac{\mathrm{d}\sigma}{\mathrm{d}\Omega} = F\left(\frac{1}{4\pi\epsilon_0}\right)^2 \left[\frac{Z_1 Z_2 e^2}{4E\sin^2(\theta/2)}\right]^2 g(\theta, m_1, m_2), \tag{2.8}$$

with an additional angle dependent correction factor for the transformation from the centre-of-mass to the laboratory frame of reference,

$$g(\theta, m_1, m_2) \approx 1 - 2(m_1/m_2)^2 \sin^4(\theta/2) \quad \text{for} \quad m_1 << m_2, \tag{2.9}$$

for which m_1 and m_2 are the ion and target masses. It is noteworthy that the strength of the scattered ion signal scales with the squares of the ion and target atomic numbers, thus we expect to see stronger scattering when using He^+ ions over H^+ ions. More significant, however, is the strong dependence of the scattering cross-section on the atomic number (and hence mass) of the target atom. This has the practical effect of rendering ions in the medium energy regime (energies of $\sim 100\,\mathrm{keV}$) largely insensitive to the lighter atomic species, due to the low cross-sections of such targets and the resultant poor statistics in the backscattering signal. Another feature of equation 2.8 worth mention is the characteristically large 'Rutherford' dependence of the cross-section on the scattering angle, with much of the Coulombic scattering in the forward direction, and a far lower probability associated with an ion scattering through a large angle.

2.2.3 Energy loss, straggling and neutralisation

As discussed previously, ions incident on a target material have a low probability of a nuclear encounter which leads to scattering through a large solid angle, with most of the ions suffering only minor deflections and travelling deep into the material. The accumulation of successive weak nuclear encounters serves to slow the incident ions as they travel through the crystal, with this loss of energy being referred to as nuclear stopping. Ions will also interact with the electron clouds surrounding the target nuclei, as these electrons have comparable velocities to those of the ions, resulting in high probabilities associated with excitation and ionisation of the target atoms [12, 13]. These electronic processes will also serve to slow the ions, an effect known as electronic stopping. These cumulative effects are combined into a quantity known as the 'stopping power', which depends on the exact combination of target species, ion type and ion energy. For the ion energies used in MEIS the electronic processes dominate; this is because the cross-section for the ion/electron interactions is very strong for medium energy ions.

As the processes which contribute to the stopping power accumulate in a steady manner as the ion traverses the target material, the energy lost by the ion is a function of the total distance travelled within the crystal. This enables the determination of the depth d of a backscattering event, if the initial and final energies of the scattered ion are known, together with angles which describe the scattering event (see figure 2.3). The

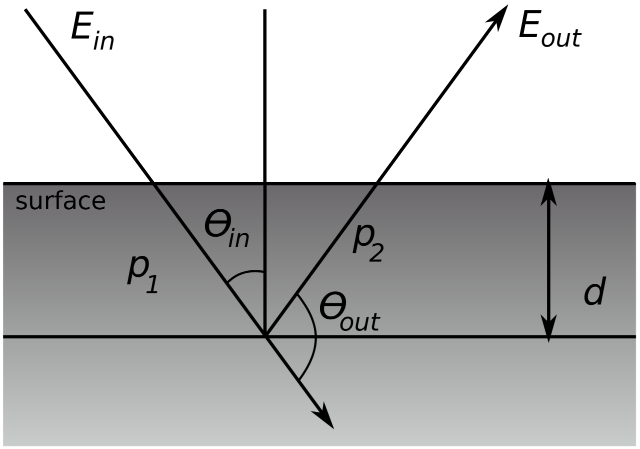

Figure 2.3: Diagram shows the trajectory of an ion backscattered at depth d in a target material.

final energy E_{out} of the emerging ion is given by

$$E_{\text{out}} = k^2 \left(E_{\text{in}} - Sp_1\right) - Sp_2, \tag{2.10}$$

where S is the stopping power, and the total path length within the material $p_1 + p_2$. One can then easily find the depth to be

$$d = \frac{\left(k^2 E_{\text{in}} - E_{\text{out}}\right)}{S} \left[\frac{\cos\theta_{\text{in}} \cos\left(\pi - \theta_{\text{in}} - \theta_{\text{out}}\right)}{\cos\theta_{\text{in}} + k^2 \cos\left(\pi - \theta_{\text{in}} - \theta_{\text{out}}\right)}\right]. \tag{2.11}$$

The SRIM database (Stopping and Ranges of Ions in Matter) and associated SRIM code of Ziegler, Biersack and Littmark [14] is most commonly used to obtain empirically derived values for the average stopping power per unit length S for particular ion/target combinations.

The stopping power is expressed as an average due to the spread in the losses of individual ions, with considerable effort being directed at characterising this spread, described by a Gaussian distribution of width Ω. This phenomenon is known as 'straggling', first treated theoretically by Bohr, in the case of fully ionised projectiles as

$$\Omega^2_{\text{Bohr}} = 4\pi Z_1^2 Z_2 e^4 N L, \tag{2.12}$$

where N is the density of atoms per unit volume and L the target thickness. This early work was subsequently built upon by Chu [15], and more recently Yang et al. [16] have developed empirical expressions for the energy spread based on the work of Chu and a wide range of experimental data

$$\Omega^2_{\text{Chu}} = \frac{\Omega^2_{\text{Bohr}}}{1 + A_1 E^{A_2} + A_3 E^{A_4}}. \tag{2.13}$$

Here the parameters A_1 to A_4 are target dependent, and are listed in [16].

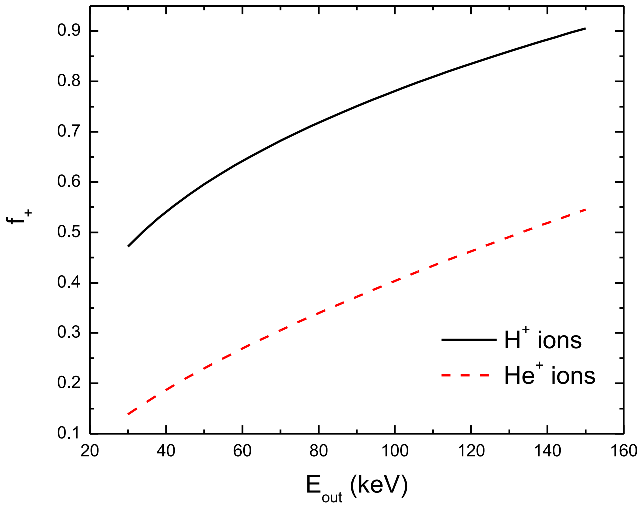

Figure 2.4: The fraction of emergent projectiles positively ionised as a function of emerging projectile energy for H^+ and He^+ ions incident on any target material is shown in graphical form, based on the empirical formulae of Kido [18].

As mentioned previously, electronic stopping involves the successive excitation and ionisation of the target atoms by the ion as it travels through the material. These processes can result in the incident ion capturing an electron and becoming neutralised. This possibility is of considerable importance in techniques such as MEIS and LEIS (Low Energy Ion Scattering), as they utilise electrostatic analysers which will fail to detect any neutralised projectiles. As such there exists large body of work concerned with quantifying this effect, particularly in the LEIS energy regime where this problem is more severe. Due to the difficulties involved in evaluating the well known cross-section for electron capture [17], the approach has instead focused on the derivation of empirical formulae from the experimentally measured neutral fractions of backscattered projectiles from many target materials. For the energies used in MEIS, Kido and Koshikawa [18] have obtained empirical formulae based on the data published by Marion and Young [19], given below as

$$f_+\left(E_{\text{out}}\right) = 0.17442\left(E_{\text{out}} - 10.2087\right)^{1/3} \text{ for } \quad 30 \rightarrow 150\,\text{keV H}^+ \text{ ions} \tag{2.14}$$

$$f_+\left(E_{\text{out}}\right) = 0.02045\left(E_{\text{out}} - 12.3388\right)^{2/3} \text{ for } \quad 30 \rightarrow 200\,\text{keV He}^+ \text{ ions,} \tag{2.15}$$

where f_+ represents the fraction of the total number of backscattered projectiles which are positively ionised, and E_{out} is expressed in keV. Here the important point worth noting is that this ionised fraction depends not on the target material but on the energy of the projectiles as they exit the material. This is because the projectile is constantly neutralised and re-ionised as it travels through the target, with the energy of the emerging projectile determining the final ionisation state. Equations 2.14 and 2.15 are shown graphically in figure 2.4, where it becomes clear that for the 100 keV H^+ ions used in the work presented in this thesis the fraction of positive ions is $\sim$ 80%, with roughly 20% of the backscattered projectiles therefore going undetected.

2.2.4 Shadowing and blocking

The medium energy ion scattering technique is not intrinsically surface specific. The low probability of a nuclear encounter coupled with the energy of the incident ion ensures that most of the ions will travel deep into the target material, thus the vast majority of the ions emerging from the target will have been backscattered from atoms located within the bulk of this material. Surface sensitivity can be achieved, however, in the case of a single crystal target if one exploits the existence of 'shadow cones' to create a channelling effect, in which the backscattered yield from the bulk of the crystal is dramatically reduced.

For any flux of parallel ions incident on a target nucleus, the ions are deflected such that a region of zero flux forms behind the nucleus, a region referred to as the 'shadow cone'. This effect is illustrated in figure 2.5. If the incident ion beam is oriented so as to be aligned with a major crystallographic direction, then the subsurface atoms in successive atomic layers are shadowed by the atoms in the surface region. Those ions not backscattered in the surface region suffer small deflections, and are steered away from the atomic rows in a process known as 'channelling' (a phenomenon discussed in more detail in [20]). These channelled ions thus travel deep into the crystal but remain undetected as they do not undergo backscattering events. In fact, whilst the non-backscattered ions in the near surface region are channelled strongly, as these ions travel deeper into the crystal the successive small deflections suffered give rise to an increase in their momentum perpendicular to the main direction of travel. Eventually this transverse momentum leads to a dechannelling effect [20], resulting in steady rise in the number of backscattered ions

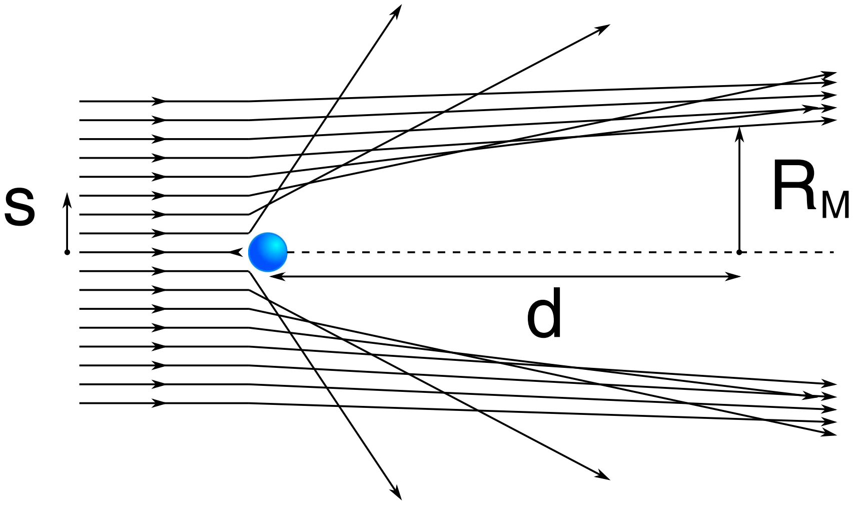

Figure 2.5: Figure shows the trajectories of a beam of parallel ions incident on a target atom nucleus, and the resulting shadow cone of radius R_M as a function of the distance d.

with increasing penetration depth. If, however, any of these ions emerge from the crystal and are subsequently detected, they are at a much lower energy than those scattered from the surface region (due to increased electronic stopping) and thus can be differentiated from these surface ions with an energy sensitive detector.

In practice, the shadowing effect is not perfect, even in the case of an ideal crystal with an unreconstructed surface; this is due to the thermal vibrations of the target atoms. As the ion transit time through the surface region ($\sim 10^{-15}$ seconds) is much smaller than the period of the atomic vibrations ($\sim 10^{-12}$–10^{-13} seconds) [2] the ions encounter an effectively static lattice with each atom randomly distributed around its lattice position. This inevitably leads to a reduction in the shadowing of the near subsurface layers, and the ions backscattering from these subsurface atoms will contribute significantly to the overall detected yield. For a typical beam/sample alignment geometry used in this thesis, the signal from all subsurface scattering is in the order of half the magnitude of that arising from scattering from the unshadowed surface atoms alone. Increased illumination of the subsurface atomic layers will also occur if the clean surface is reconstructed due to the presence of a foreign species. Given these displacements, be they random (due to vibrations) or static, it is often useful to accurately determine the radius of the characteristic shadow cones at the position of the first subsurface atom to be shadowed. The radius of a shadow cone cast by a bare Coulomb potential is easily calculated [2] as

$$R_C = 2\sqrt{bd}, \tag{2.16}$$

where R_C and d are the Coulombic shadow cone radius and distance behind the scattering atom respectively, as shown in figure 2.5, and b is given by

$$b = \left(\frac{1}{4\pi\epsilon_0}\right)\frac{Z_1 Z_2 e^2}{E}.$$

No such simple expression exists for the screened Coulomb potential due to Molière, but the ratio of R_M/R_C can be derived from empirical fits to experimental data obtained from a wide variety of ion/target combinations [21], so that

$$R_M = \xi R_C \tag{2.17}$$

$$\xi = \begin{cases} 1.0 - 0.12\alpha + 0.01\alpha^2 & 0 \leq \alpha \leq 4.5 \\ 0.924 - 0.182\ln\alpha 0.008\alpha & 4.5 \leq \alpha \leq 100 \end{cases}, \tag{2.18}$$

where α is a dimensionless parameter given as

$$\alpha = \frac{R_C}{a}.$$

Here a is the aforementioned Thomas-Fermi screening length.

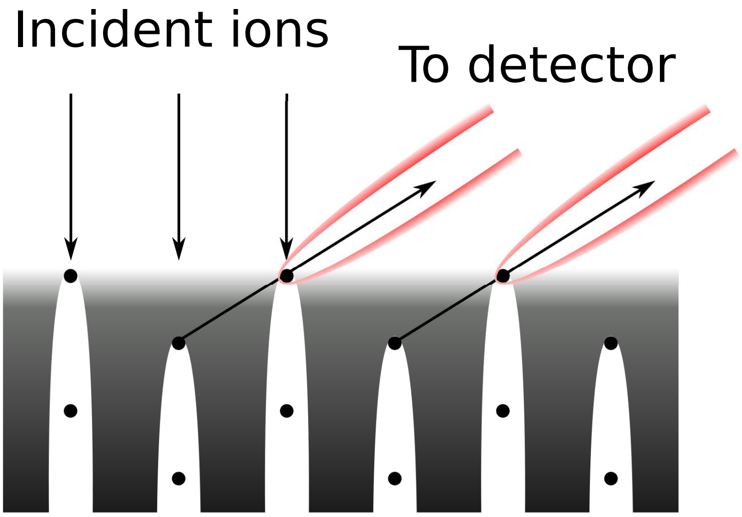

Figure 2.6: Figure shows the shadowing and blocking effects for a beam of parallel ions incident on a single crystal surface. Shaded areas within the crystal represent regions of ion flux, highlighting the unshaded regions below the scattering atoms which receive zero flux. Shown in red are the shadow cones cast as surface atoms block the backscattered ions exiting the crystal.

In addition to the phenomenon of shadowing, which ensures surface specificity, a similar effect occurs for ions backscattered from the subsurface layers, in which these ions are blocked in the outgoing trajectories which intersect with surface atoms (See figure 2.6). This gives rise to characteristic dips in the intensity of scattering signal centred around scattering angles which correspond to major crystallographic directions, with the resulting plots of scattering intensity versus scattering angle referred to as 'blocking curves'. The exact angular position of the dips relates to the positions of these surface blocking atoms, and so in principle the phenomenon of blocking allows one to determine the surface structure. However, many surface reconstructions are of a complex nature, possibly involving many nonequivalent movements of surface atoms both within the plane of the surface and perpendicular to the surface. Therefore, in practice, gaining insights into the exact nature of the structures adopted by surfaces involves the comparison of the experimental blocking curves with theoretical blocking curves which have been simulated for a given structural model.

2.3 Simulating MEIS blocking curves

The experimental blocking curves presented in this thesis, in which the measured scattering intensity is plotted as a function of the scattering angle, are in general compared to the results of one or more computer simulations of particular surface structural models. These computations have been performed using the VEGAS code, a program developed specifically for use in MEIS by Frenken et al. of the FOM-AMOLF institute [2, 22–24]. This program uses a Monte-Carlo based algorithm and principles such as time-reversal to efficiently calculate the scattering probability for each atom of a structural model in a given incidence/exit geometry. In this section a brief insight into the details of this computation is given, but the interested reader is referred to reference [22], wherein a more detailed description of the principles behind the VEGAS code can be found.

The most obvious method to simulate the ion scattering for a given structure would involve a full simulation of the experimental conditions, with many incident ions generated and subsequently tracked as they interact with the target material, and in some cases finally reach the detector. This method is impractical, however, if we consider the fact that very few ions will undergo a backscattering event due to the low associated cross-section, and even fewer still will then have an exit trajectory in the scattering plane of the detector, or even be backscattered through a solid angle within the plane which is of interest. A much less computationally expensive method for predicting the scattered ion yield in a particular exit direction is to firstly determine the probability for a particular atom to be hit by the incident beam, and then determine the probability

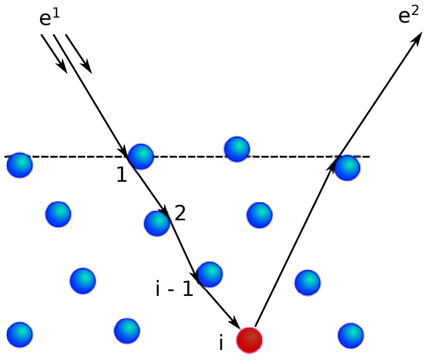

Figure 2.7: The incidence and exit directions e^1 and e^2 for an ion backscattering from atom i, shown in red. This ion will suffer a series of small angle deviations in its incidence and exit trajectories due to interactions with other atoms, taken into account by a Monte-Carlo algorithm in the VEGAS code used for simulating MEIS blocking curves [22].

associated with an ion scattered from this atom reaching the detector in the direction of interest. It is then easy to determine the scattering probability for this atom, and in turn the other atoms in the model surface unit cell. In this manner the overall scattering yield in particular incidence and exit directions can be calculated.

Let us consider backscattering from a particular atom i at the position x_i in the incidence and exit directions e^1 and e^2, respectively, as shown in figure 2.7. We can call the scattering probability $Y_i(e^1, e^2)$, and this can be expressed as

$$Y_i\left(e^1, e^2\right) = \int d^3x_i \, F^1\left(e^1, x_i\right) G_i\left(x_i\right) F^2\left(e^2, x_i\right). \tag{2.19}$$

Here G_i represents the probability that atom i is located at the position x_i; this is a Gaussian distribution about the atom's equilibrium position, and represents the effects of thermal vibrations. F^1 represents the incident ion flux at position x_i, in other words the probability of an incident ion reaching position x_i. This term is normalised so that the probability of an unshadowed atom receiving an ion is unity. Similarly F^2 is the probability that the backscattered ion will reach the detector in the direction e^2, normalised to unity in the absence of any blocking effects. Of course, this scattering probability must strictly be integrated over all possible positions x_i. Whilst the function G_i is well known, accurate determination of F^1 and F^2 is difficult as these quantities depend not only on the collision parameters but also G_k for the atoms $k \neq i$ along the incoming and outgoing paths. Equation 2.19 can be simplified with the revelation that in the absence of any blocking ($F^{2} = 1$), Y_i is in fact the hitting probability H_i of atom i:

$$H_i = \int d^3x_i \, F^1 \left(e^1, x_i\right) G_i \left(x_i\right). \tag{2.20}$$

Similarly the detection probability D_i can be determined if the incidence is assumed to be in a random direction, thus fully illuminating atom i ($F^{1} = 1$):

$$D_i = \int d^3x_i \, F^2 \left(e^2, x_i\right) G_i \left(x_i\right). \tag{2.21}$$

Having calculated these probabilities the following approximation is then made (which is shown to be a good one in the vast majority of cases [23]),

$$Y_i \approx H_i D_i. \tag{2.22}$$

As the energy losses suffered by ions in the surface region are normally only a small fraction of the incident energy, the principle of time-reversibility can be used, in which $F^{2}(e^{2}, x)$ can be expressed as $F^{1}(-e^{2}, x)$, in other words the probability of an ion being detected in a particular exit direction is identical to the probability of such an ion incident in that direction hitting the scattering atom in question. Thus, only the hitting probabilities for each atom need be calculated, albeit separately for each exit angle considered, in addition to the incidence direction.

In order to speed up the calculation of the atom hitting probabilities, in which the string of atoms between the atom of interest and the ion incidence position must be considered, a standard Monte-Carlo integration is employed. In this Monte-Carlo approach a special sampling function is used, as opposed to random sampling, which matches the function G_i; this has the effect of greatly simplifying the calculations.

Scattering probabilities calculated in this manner are normalised to be unity in the case of an unshadowed (or blocked) surface atom. A final normalisation is then made of the total scattering probability for a whole atomic layer of the crystal in question, such that in the final simulated blocking curves a yield of unity corresponds to the signal from the surface layer. This leads to the consideration of total scattering yields in terms of the number of *visible* atomic layers, with subsurface layers contributing smaller and smaller fractions of a full layer visibility, due to the increased degree of shadowing from the layers of atoms above.

It is perhaps worth mentioning that in some circumstances particular atoms can report a normalised scattering probability of greater than unity, thus leading to a larger than expected visibility of the particular atomic layer in question. This is due to a 'focusing effect', most evident for a subsurface atom which possesses an equilibrium position just beyond the shadow cone radius of an atom in the layer above, for which the normalised incident flux F^1 is greater than 1 due to the focusing of the trajectories of ions suffering small angle collisions with the shadowing atom.

2.4 Instrumentation

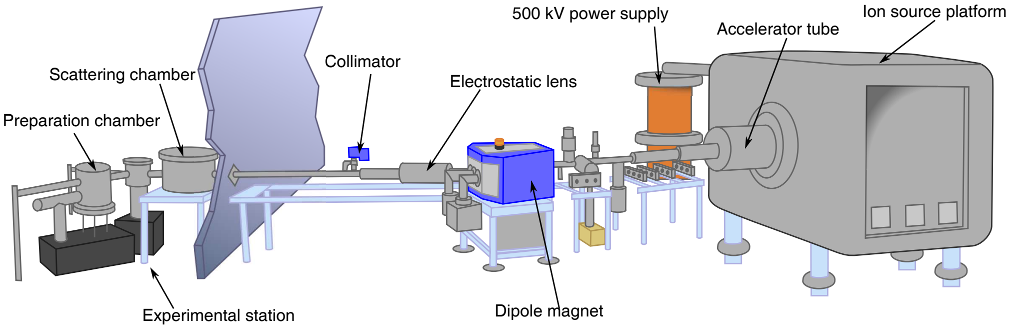

Figure 2.8: The layout of the accelerator, beamline and ultra-high-vacuum (UHV) scattering and preparation chambers, which all together constitute the UK National MEIS facility at Daresbury Laboratory.

The data presented in this thesis were gathered at the UK national MEIS facility at Daresbury Laboratory. This facility (see figure 2.8) comprises an accelerator system for the production of the ions and several chambers under ultra-high-vacuum (UHV), these chambers being situated within an experimental end-station. The main scattering chamber in which the MEIS data are gathered, a preparation vessel and a fast-entry load lock are connected via interlocks to a storage chamber. In this way several samples may be loaded, prepared, characterised and stored in situ.

The ions (usually H^+ or He^+) are generated in a duoplasmatron source as an ionised gas which is then extracted into a linear accelerator, capable of delivering ions of energy between $50 - 400$ keV. The beam is focused by passage through a quadrupole lens, whereupon the beam enters a bending magnet which selects only ions of the required type (the duoplasmatron source will typically generate a small fraction of undesirable ions such as H_2^+). The beam is then focused again with a quadrupole lens, after which the beam is aligned by electromagnetic steerers so as to pass through two successive sets of defining slits. This results in a beam which enters the main scattering chamber characterised by a width of 1.0 mm, a height of 0.5 mm and a divergence of less than 0.1°. Before the beam encounters the sample material it passes through a fine tungsten mesh situated at the entrance of the scattering chamber. This mesh detects a known fraction of the beam current, thus the current incident on the sample can be determined; it is found to be typically in the range $15 - 100\,\text{nA}$.

The beam finally encounters the sample which is mounted on a sample holder capable of interfacing with the multi-chamber sample transfer system, itself mounted whilst in the main chamber in a high-precision goniometer. This enables the sample to be rotated in three distinct axes to an accuracy of $\sim 0.1^\circ$. In this manner the sample can be precisely aligned with respect to the incident ion beam along a particular crystallographic direction of interest.

Housed within the main chamber is a toroidal electrostatic analyser (TEA), manufactured by High Voltage Engineering Europa [25]. This TEA is mounted on a rotation table, and is thus capable of rotating within the scattering plane. The TEA has a wide entrance slit which can accept ions scattered over an range of $\sim 27^\circ$. This slit is, however, narrow in height (0.5 mm), and in fact this slit defines the scattering plane; the sample is oriented so that the desired atomic scattering planes lie in the plane of the beam and the TEA entrance slit. Backscattered ions which enter the TEA are deflected via a pair of concentric toroidal electrostatic deflection plates through an angle of 90°, with the symmetry of the analyser around the scattering centre ensuring that the true scattering angles of the detected ions are maintained. The combination of electrostatic deflection and conservation of scattering angle allow a position sensitive detector to simultaneously record both the scattering angle and final energy of the detected ions. The energy window of the detector is 1.5% of the pass energy E_{pass}, with the pass energy being the central energy within the energy window. This pass energy is controlled by the voltages applied to the electrostatic plates. Data spanning a wide energy range can be collected by accumulating several identical doses of incident ion flux, with the pass energy being reduced by the required amount in a stepwise fashion. The individual 2 dimensional datasets can then be combined together using the data acquisition software MIDAS (Multi-Instance Data Acquisition System). In addition, the blocking curves shown in this thesis cover a wide range in scattering angle, this is because after data have been successfully collected at one position the analyser is typically moved so as to cover a neighbouring range of scattering angles, such that most experimental blocking curves comprise between $2 - 4$ such angular ranges.

The 2D spectra obtained from a crystal which has been aligned to a major crystallographic direction in order to gain surface specificity possess a characteristic energy peak (see figure 2.9) which corresponds to the large backscattered ion flux from the surface region, with this energy of this peak determined by the kinematic factor (equation 2.1) By contrast, ions which scatter from the deeper layers and suffer inelastic energy losses due to electronic stopping are detected in far fewer numbers, as seen by the low

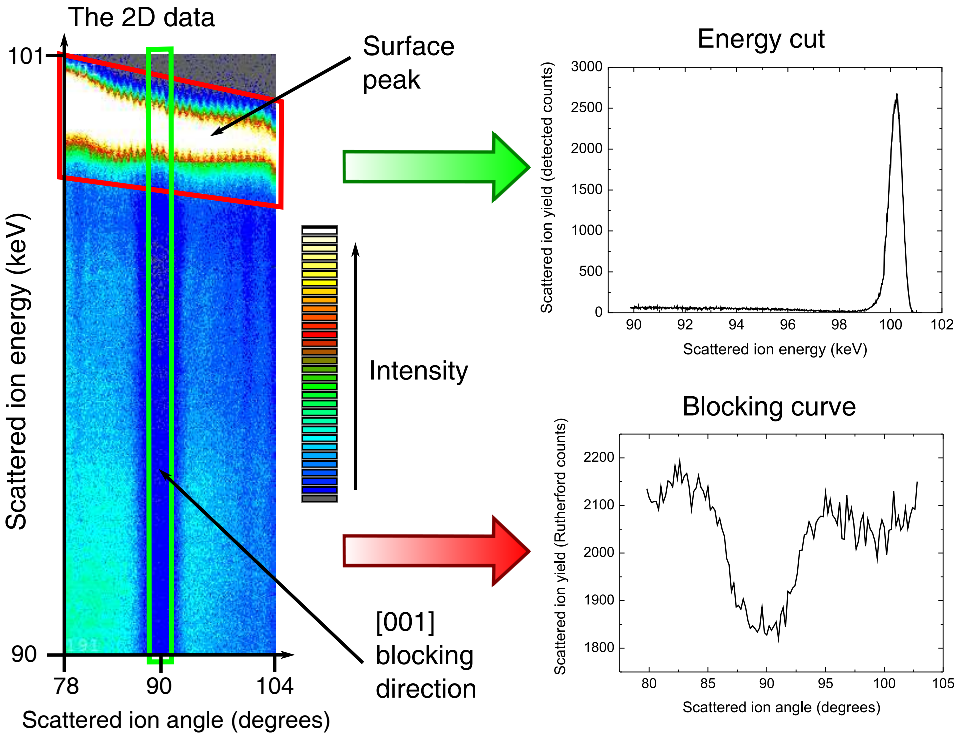

Figure 2.9: A 2D spectrum representative of those collected in MEIS, with a characteristic high intensity surface peak. These data were obtained via the scattering of 100 keV H^+ ions from a clean Au(111) surface. Integrating the signal over a narrow angle range (shown in green), or over energy for merely the surface peak (shown in red) results in the production of an energy cut or blocking curve, respectively.

counts for all energies below the surface peak. In order to extract a blocking curve, the surface peak is integrated over the energy range, producing a plot of integrated ion intensity versus ion scattering angle. This integration is commonly performed using a surface peak-tracking/fitting routine developed within the group at Warwick University. This routine utilises the ROOT C++ libraries for data analysis [26] initially developed at CERN, Switzerland (these libraries have been made freely available under the GNU Lesser General Public Licence). In this routine an asymmetric Gaussian is fitted to the surface peak for each individual channel in scattering angle, with the experimental counts integrated over a range specified by the fitted peak. As a final step, the resulting blocking curve is corrected so as to remove the 'Rutherford' dependence of the intensity upon the scattering angle; this has the effect of producing blocking curves without an overall gradient in the scattering signal (i.e. a flat background). This step not only makes for an easier visual inspection of the characteristic blocking curve dips, but crucially allows the experiment to be directly compared to the VEGAS simulated blocking curves with the use of a suitable scaling factor λ, a subject expanded upon in the next section.

2.5 Surface structure determination

2.5.1 Experiment-theory comparisons using reliability factors

Direct comparisons can be made between the blocking curves of experiment and theory via the use of a scaling factor λ. This term relates experimental yields in (Rutherford corrected) ion counts to the number of visible atomic layers, this being the way the yield is expressed in the VEGAS simulated blocking curves. Of course, even in the absence of any theoretical simulations it is still in general more informative to consider experimental yields in terms of visible layers. As such, the accurate determination of λ is of key importance. This factor can be derived from the experimental yield obtained from a surface with a *well-known* structure, i.e. one for which layer visibility can be predicted with good accuracy. For the work presented in this thesis, a scaling factor has most commonly been derived from the signal obtained from ions scattered from Cu atoms shallowly implanted to a known concentration within a Si(100) wafer. A detailed account of the methodology of this calibration process is included in the following chapter.

Although a suitable scaling factor provides a way to visually inspect the agreement between experiment and theory, a visual inspection alone, or a visual comparison of the merits of several theoretical fits to the same experiment is often inaccurate and always subjective. For this reason, reliability-factors have often been used in MEIS to objectively quantify the 'goodness of fit' between experiment and simulation. Woodruff et al. [27, 28] have previously assessed the suitability of a range of these 'R-factors' for use in MEIS, with the preferred one being a reduced chi-squared R-factor R_χ, defined by the following equation,

$$R_\chi = \left(\frac{1}{N}\right) \sum_i^N \left[\frac{(I_{exp} - \lambda I_{theo})^2}{I_{exp}}\right], \tag{2.23}$$

where N is the total number of data points compared, and I_{exp} and I_{sim} are the experimental and theoretical ion intensities. The experimental intensity is expressed in terms of raw counts, and there are a number of points worth mentioning regarding this fact. Firstly, the use of the raw counts renders equation 2.23 a true chi-square function used in statistics [29]; this means that a value of unity is expected in the case of a perfect fit, as the I_{exp} denominator is subject to Poisson statistics and so is, on average, equal to the square of the error on this quantity. Secondly, note how the value for R_χ increases, all else being equal (excepting the scaling factor λ), if the value of I_{exp} is doubled (with

λ doubled accordingly). For this reason one cannot prescribe a general 'goodness of fit' criterion based on the absolute value of R_χ, and must instead rely on its usefulness as a relative measure of the goodness of fit for the simulations of several structural models describing a particular set of experimental data. A final point relating to the use of raw ion counts concerns the 'Rutherford correction' of the experimental yields described in the previous section, where a factor of $\sim \sin^4(\theta/2)$ is applied to the data to remove the cross-sectional dependence on the scattering angle θ. The R-factor operates on the raw uncorrected counts, so seemingly small disagreements at low scattering angle between experiment and theory blocking curves have a large influence on the final R-factor. Thus the fits are generally biased towards minimising the low scattering angle yield discrepancies.

In MEIS experiments more than one incidence geometry is often exploited to increase the available structural information, this leads to multiple blocking curves, each with a corresponding R-factor when compared to theory. An overall combined R-factor can be obtained thus

$$R_{Overall} = \frac{N_1 R_1 + N_2 R_2 + \cdots N_n R_n}{N_1 + N_2 + \cdots N_n}, \tag{2.24}$$

with each individual R-factor weighted by the size of its respective dataset.

The choice of a chi-squared R-factor also makes the estimation of the uncertainty associated with a particular structural parameter rather straightforward, with the error being given as [29]

$$\sigma = \sqrt{\frac{2}{\left(\frac{d^2 R_\chi}{dZ^2}\right)_{R=R_{\mathsf{min}}}}}. \tag{2.25}$$

Thus if one calculates the R-factor as a function of the parameter of interest around the best-fit value for that parameter, one can use the curvature of the R-factor to estimate the uncertainty.

2.5.2 Optimising the structural model

When a model is found, often by a trial-and-error process, which provides a good description of the experimental data, a next step involves the optimisation of parameters of this structural model. The goal is to find the global minimum of the R-factor in the parameter-space considered, enabling the resulting set of parameters and the structure they define to be considered the 'best-fit' to the experimental data. Whilst the global minimum search can be undertaken in a manual fashion using a grid-based method, this method is time-consuming; another approach involves the use of an automated search routine. A number of these routines, such as Genetic Algorithms and Simulated Annealing attempt a global search of parameter-space, in order to avoid the problems associated with becoming trapped in a local (rather than global) minimum. Unfortunately, these methods often involve full simulations of many hundreds of structural models and are deemed unfeasible for application to MEIS. This being said, previous success has been had [30, 31] in MEIS with the use of line search methods which sample the R-factor gradient within a well defined region of parameter-space and attempt to converge on the R-factor minimum. The current version of this routine used by the group at Warwick University will now be described in brief; a fuller description of this method can be found elsewhere [32].

The routine is base on a Quasi-Newton (BFGS) algorithm [33, 34]. In such methods a function, in this case the chi-square R-factor, is approximated with a quadratic model which is then used to determine the position of the function's minimum. This quadratic model depends on both the gradient $\nabla_h f(x)$ at the sample point x and the estimated Hessian B (a matrix of second derivatives). These quantities are used to determine the search direction, and an iterative line search process is undertaken, with the gradients calculated at each step used to update the estimated Hessian. The newest version of the routine uses an improvement on this standard method which involves varying the line search step size h as the optimisation proceeds [35]. The step size is initially given a large value to ensure that low amplitude noise in $f(x)$ does not have the effect of mis-directing the search, with successive iterations adopting smaller values for h as the search closes in on the minimum. This approach, called *Implicit Filtering*, is found to be more robust in dealing with statistical variations in the R-factor function associated with the use of Monte-Carlo methods in the VEGAS simulations. Hereafter this automated optimisation routine is referred to by the acronym IFFCO (Implicit Filtering for Constrained Optimisation).

2.6 Supplementary experimental techniques

2.6.1 Low Energy Electron Diffraction (LEED)

Low energy electron diffraction, more commonly referred to by its acronym LEED, is one of the oldest surface science techniques, dating back to the early experiments of Davisson and Germer [36], which provided the first proof of the wave-like nature of the electron. LEED has since become one of the most commonly used techniques in Surface Science [37], providing both qualitative and quantitative information. This technique has been used, whenever possible, to qualitatively characterise the systems studied in this thesis, therefore a brief description of the technique will follow; far fuller descriptions are found in many texts, with the reader referred to the treatment given by Van Hove [38].

In LEED a collimated beam of electrons of energy in the range $20 - 300\,\mathrm{eV}$ is generated by an electron gun, and this beam is incident upon a surface of interest, possessing a 2-dimensional periodicity defined by the primitive lattice vectors $\mathbf{a}$ and $\mathbf{b}$. Electrons of these energies have characteristic wavelengths in the order of $\sim 1\,\text{Å}$, this value being the same order of magnitude as the interatomic distances in the solid target. Thus the conditions for diffraction of the incident electrons by the surface atoms are met. The surface specificity implied in the previous sentence arises due to the high cross-section for both elastic and inelastic scattering of the incident electron, resulting in a strong attenuation of the electron beam within the few atomic layers closest to the solid/vacuum interface. If the wave-vector of an incident electron is $\mathbf{k}$ and that of the diffracted electron $\mathbf{k}'$, then considering the conservation of energy we have

$$|\mathbf{k}'|^2 = |\mathbf{k}|^2, \tag{2.26}$$

and considering the conservation of momentum we arrive at

$$\mathbf{k}'_{\|} = \mathbf{k}_{\|} + \mathbf{g}_{\mathbf{hk}}, \tag{2.27}$$

where $\mathbf{g}_{\mathbf{hk}}$ represents the reciprocal net vector. Notice how only the wave-vector components parallel to the surface are conserved. This is because the surface net only possesses a periodicity parallel to the surface plane. The reciprocal lattice vector is given below as

$$\mathbf{g}_{\mathbf{hk}} = h\mathbf{a}^* + k\mathbf{b}^*, \tag{2.28}$$

where $\mathbf{a}^*$ and $\mathbf{b}^*$ are the translation vectors of the reciprocal lattice, found by

$$\mathbf{a}^* = 2\pi\frac{\mathbf{b}\times\mathbf{n}}{A} \qquad \mathbf{b}^* = 2\pi\frac{\mathbf{n}\times\mathbf{a}}{A} \qquad A = \mathbf{a}\cdot\mathbf{b}\times\mathbf{n}. \tag{2.29}$$

Here $\mathbf{n}$ is a unit vector normal to the surface. Thus constructive interference and the associated diffraction beam occur when the change in the parallel component of the electron wave-vector is equal to a reciprocal lattice vector characterised by the integers h and k, with the resulting beam spot identified by this pair of integer values.

In a typical LEED apparatus, as shown in figure 2.10, the diffracted beams produced by the diffraction of the incident beam propagate through a field-free region, produced by grounding the first of a series of hemispherical retarding grids, the subsequent grids being negatively biased, such that electrons not having undergone a purely elastic collision are suppressed. The electrons finally encounter a fluorescent screen held at a voltage of $5\,\mathrm{kV}$, which serves to accelerate the electrons to a degree sufficient to

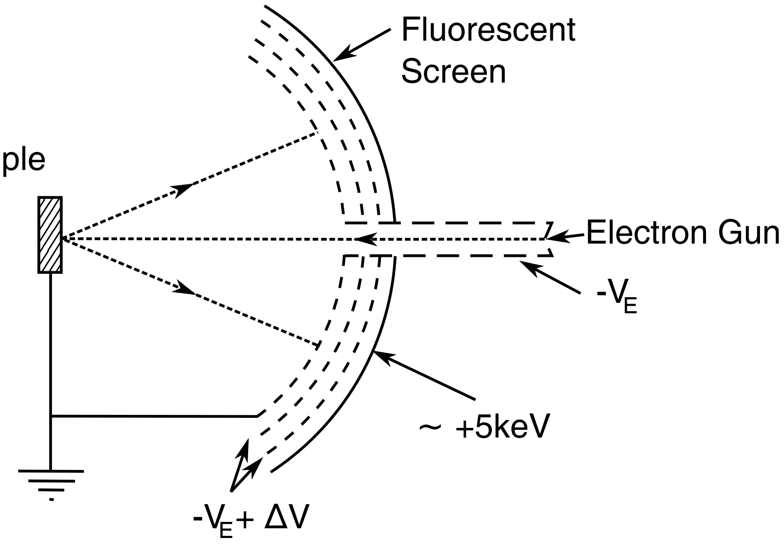

Figure 2.10: A schematic diagram of a standard LEED apparatus where the dotted arrows show the path of the electrons and V_E is electron source filament potential.

produce a visible beam spot. Thus the diffraction pattern produced can be considered a scaled representation of the reciprocal surface net, and a quick visual inspection is often enough to deduce the real-space surface net via an inversion of equations 2.29. LEED has been extensively used in this thesis as a way to judge the degree of order on clean transition metal single crystal surfaces, most often characterised by a set of diffracted beams consistent with a (1×1) periodicity of an unreconstructed surface. The sharpness of the diffracted beam spots gives an indication of the degree of order in the surface region. This technique has also served as a way to check the phase of adsorbate overlayer structures.

2.6.2 Auger Electron Spectroscopy (AES)

Auger electron spectroscopy is a technique which takes advantage of the characteristic 'Auger' electrons emitted from surface atoms previously ionised by an incident electron beam. Captured by a suitable energy analyser, these Auger electrons carry information about the surface chemical composition; for this reason the technique has been used as a judge of the cleanliness of the clean metal surfaces studied in this thesis. The interested reader is directed to [39] for a detailed description of this technique but a brief description is given below.

Auger electron spectroscopy typically involves a beam of electrons of energy $1 - 10\,\text{keV}$ incident on a sample, achieving penetration depths of $\sim 1\,\mu\text{m}$. This will result in some ionisation of the target atoms via the production of a core hole, a hole eventually filled by a more weakly bound electron, with the energy associated with this transition lost in the form of an emitted photon, or as kinetic energy given to another weakly bound electron. This latter process, referred to as the Auger effect after its discoverer, Pierre Auger, is much more common for core holes with a binding energy less than $\sim 10\,\mathrm{keV}$, and so the Auger electrons emitted from the sample can be detected using a standard hemispherical electron analyser. Surface specificity arises from the fact that the Auger electrons have a relatively low mean-free path, suffering a high level of inelastic scattering. The energies of the detected Auger electrons depend primarily on the binding energy of core level in which the hole was produced, an energy characteristic of the particular atom involved. In each atom transitions involving a number of possible energy levels will occur with varying probabilities; this gives rise to a unique 'finger print' of energy peaks for each atomic species in the collected spectrum. A typical Auger spectrum collected will contain peaks characteristic of transitions from several types of atom, a handbook containing example spectra is then consulted enabling the identification of the atomic species present on the surface.

Chapter 3

The structure of the Cu(410)-O surface

3.1 Introduction

Vicinal single crystal surfaces (surfaces made up of low-index crystal planes separated by atomic steps and kinks) have long been of interest due to the enhanced catalytic activity [40] and the adsorption and desorption behaviour [41] evident on these surfaces in contrast to simpler low-index single crystal surfaces. It is widely accepted that the steps themselves play a dominant role in the behaviour of these surfaces, and as such there have been many attempts to understand the atomic structure in these step regions. These step regions tend to be characterised by increased structural relaxation relative to the ideal bulk-like termination, due to the reduced coordination of the atoms at the step sites.

The Cu(410)-O stepped surface is a particularly suitable surface for study with medium energy ion scattering (MEIS) for a two main reasons:

1. A number of Cu surfaces vicinal to the (100) plane facet to form (410) regions as a consequence of oxygen adsorption [42–48]; clear evidence that the Cu(410)-O surface has a particularly low associated energy and is particularly stable.

2. Pronounced atomic roughening of the step edges [49, 50] in clean Cu(410) at room temperature, a general problem with clean metallic vicinal surfaces, is found to be alleviated by the adsorption of oxygen [49].

Thus, both the structural stability and the presence of well ordered steps make the Cu(410)-O surface ideally suited for study by MEIS, as both factors lead to consistency over the large surface area probed by the ions, a prerequisite for elucidating quantitative structural information.

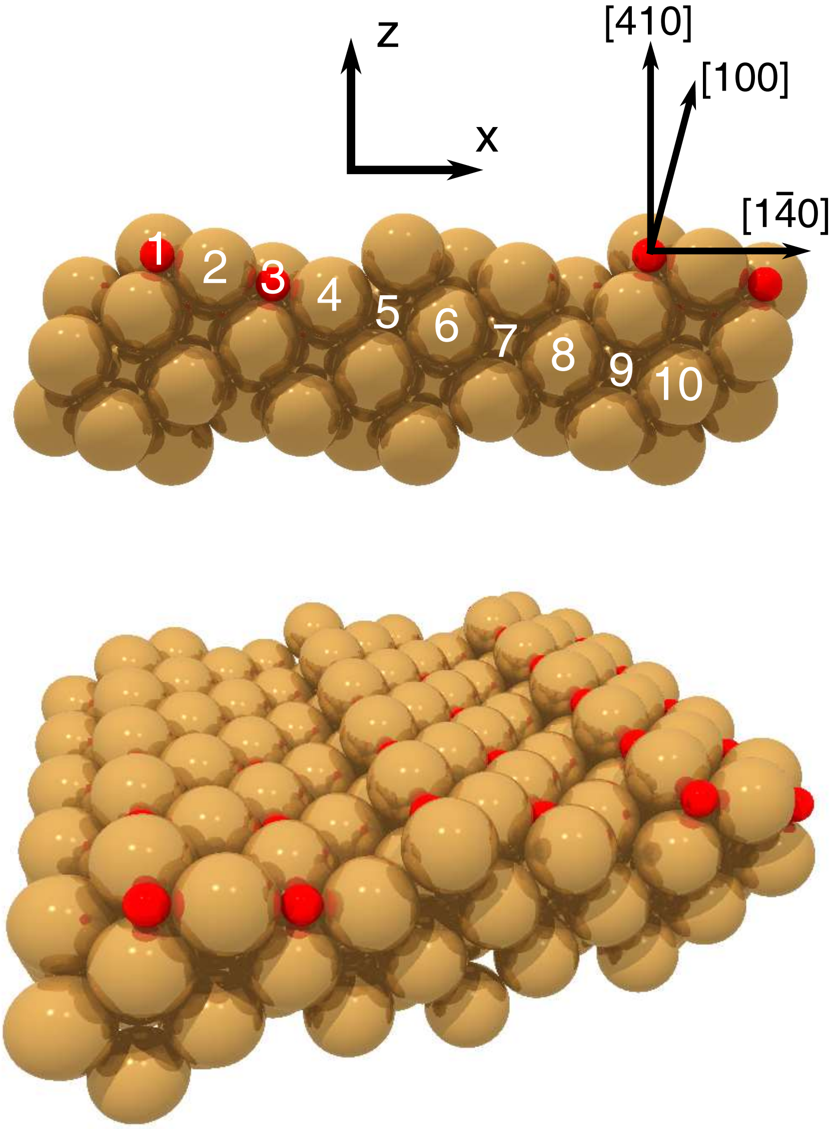

Figure 3.1: Model of the Cu(410) surface shown in a perspective and a side-sectional view. The side-sectional view is annotated with the directions of the principal axes, major crystallographic directions and the atom row numbers as described in the text. The smaller red spheres represent O atoms, and the larger spheres the Cu atoms.

The Cu(410)-O surface consists of (100) terraces separated by (001) steps, with oxygen atoms located in nominally 4-fold coordinated hollow sites on the (100) terraces (fig. 3.1).Half of these oxygen atoms occupy the 4-fold coordinated mid-terrace hollow sites, whereas the remaining oxygen atoms occupy reduced coordination hollow sites at the terrace edge. A number of previous investigations have been based on STM (scanning-tunneling microscopy) [43, 45, 51, 52], but several more quantitative studies exist. These include an early scanned-angle mode photoelectron diffraction investigation [53], and more recently investigations utilising ion scattering [54] and surface x-ray diffraction (SXRD) [55–57], with the results of some recent density functional theory (DFT) calculations also reported [55]. The previous studies have focused on a number of aspects of the structure, namely the adsorption site and layer spacing of the oxygen atoms, the relaxation of the Cu atoms relative to their ideal bulk positions and whether there is a missing Cu row on the (100) terraces. All of these questions are linked to the Cu(100)($\sqrt{2} \times 2\sqrt{2}$)R45°-O structure which forms on the singular Cu(100) surface (fig. 3.2). It is now accepted that on this surface every fourth [001] row of Cu atoms in the outermost layer is removed, leading to local geometries identical to those of the step sites on the (410) surface [46, 58–61]. One key difference between these models shown in figs. 3.1 & 3.2 is the fact that in the Cu(410)-O surface half of the O atoms occupy unreconstructed 4-fold coordinated hollow sites in the mid step as opposed to the less constrained O atoms at the step edge, whilst in the Cu(100)($\sqrt{2} \times 2\sqrt{2}$)R45°-O model all O atoms occupy the step edge site. The fact that the Cu(100)($\sqrt{2} \times 2\sqrt{2}$)R45°-O surface exhibits a missing Cu row at such O coverage had lead to the suggestion that such a fourth row would also be missing from the Cu(410)-O surface, but this has been shown to be inconsistent with the SXRD data [55]. Instead, it seems that the O atoms lie in almost coplanar sites at the step edge on the Cu(410)-O, as is the case with the Cu(100)($\sqrt{2} \times 2\sqrt{2}$)R45°-O, but at the mid step sites on the Cu(410)-O the O atoms sit above the surrounding Cu neighbour atoms, as has been found to be the case for low coverages of O on Cu(100) [59].

The remaining question is that concerning the relaxations of the outermost Cu atoms. The SXRD investigation has been the most detailed approach to this problem so far, involving many distinct structural parameters. These parameters are defined as follows: Cu and O atoms are referred to by their row (atomic layer) number, where each atomic layer is defined with respect to the (410) surface plane (row 1 atoms are those which are sited at the edge of the terrace). The ten outermost Cu atoms are labelled in such a manner in figure 3.1, and clearly all of these atoms lie along a single [001] atomic row parallel to the steps. Whilst one would expect atom movement parallel to the steps to be constrained, movement both perpendicular and parallel (along the z or [410] direction and along the x or [$1\bar{4}0$] direction) to the (410) surface is likely to occur. These movements would be largest concerning atoms in rows 1-4 which lie at the surface. Working under the reasonable assumption that the atoms in rows below

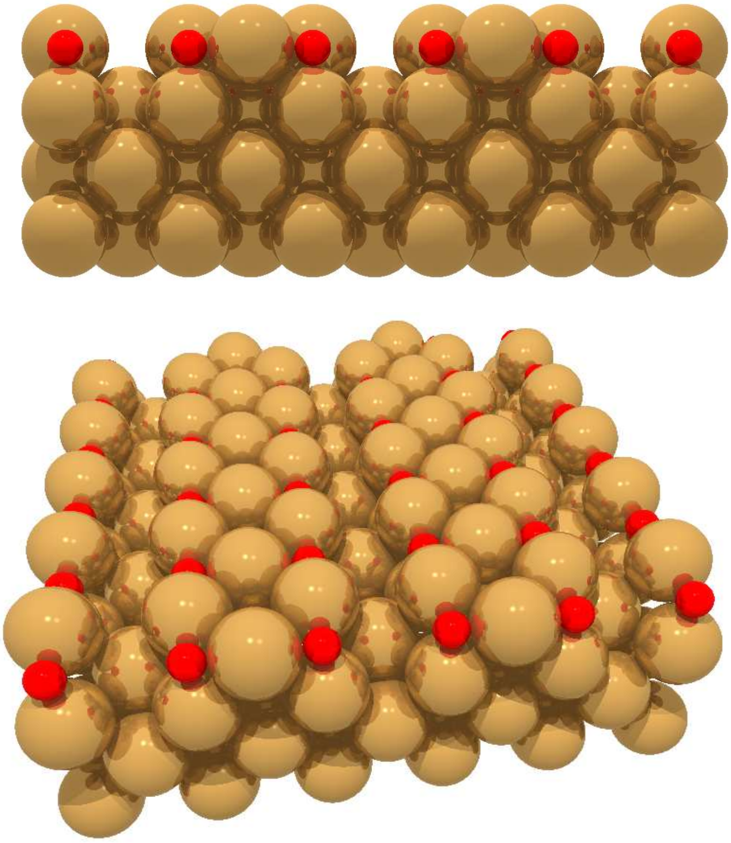

Figure 3.2: Side-sectional and perspective views of a Cu(100)($\sqrt{2} \times 2\sqrt{2}$)R45°-O model, with the smaller red spheres representing O atoms and the larger spheres the Cu atoms.

row 10 are constrained in their bulk sites, this leads to 20 distinct structural parameters which describe the outermost Cu atom configuration and 4 parameters which describe the O atom positions. These 24 parameters can be reduced to only 16 if the smaller parallel (x-axis) displacements of the atoms in rows 5-10 are assumed to be zero. It is these 16 parameters which the previous SXRD study attempted to identify. This study resulted in three distinct structural solutions being proposed, one based on the results of the DFT calculations, and two based on optimised fittings of the SXRD data using applied constraints based on Lennard-Jones potentials (hereafter referred to as LJ1 and LJ2). The structural parameter values corresponding to these three solutions are listed in table 3.1.

In order that more light be shed on this structural problem, an investigation using medium energy ion scattering (MEIS) on the Cu(410)-O surface has been undertaken, the description of which is the subject of the remainder of this chapter.

3.2 Experimental details

The experimental data were gathered at the national MEIS facility at the Daresbury laboratory, UK. The Cu(410) sample was formed via spark-machining from a single crystal Cu bar, followed by mechanical polishing using successively finer grades of diamond paste. This crystal was loaded into the ultra-high vacuum chamber system and within a base pressure of $\sim 3.0 \times 10^{-10}$ mbar cleaned in situ via repeated sputtering with Ar^+ ions and annealing to $\sim 500°C$. The sample was judged to be clean with reference to Auger electron spectroscopy (AES) and the 'split beam' low energy electron diffraction (LEED) pattern characteristic of clean Cu(410) [44]. The Cu(410) crystal was exposed to molecular oxygen (O_2) at a partial pressure of 2×10^{-7} mbar for 12 minutes with the sample held at a temperature of 300°C. The resulting (410)(1 × 1) LEED pattern was as expected, with some brighter and sharper beams (missing or weaker in the clean Cu(410) pattern) indicative of improved ordering of the step structure in the presence of chemisorbed oxygen.

Upon transfer to the main scattering chamber (possessing a routine pressure of 2.0×10^{-10} mbar), MEIS data were gathered using 100 keV H^+ ions over a range of solid scattering angles in six distinct incidence geometries (see figure 3.3) .The asymmetry of the Cu(410)-O surface was utilised to gather data in both 'up-step' and 'down-step' directions, with the scattering plane in all cases perpendicular to the [001] direction along the steps. In both of the up-step and down-step directions the ion beam was aligned along three different major crystallographic directions, the $\langle 110 \rangle$, $\langle 100 \rangle$ and $\langle 310 \rangle$, which in an ideal bulk-like solid and without considering atom vibrations, illuminate 1, 2 and 3 (100)-type surface layers respectively.

The gathered MEIS data were reduced as described in chapter 2 to form blocking curves which relate the scattered ion yield to solid scattering angle. As described previously (chapter 2), comparison of the MEIS blocking curves with simulated blocking curves was achieved via the use of a reduced chi-squared R-factor. In the calculation of such a R-factor, a key parameter is the scaling (or calibration) factor λ, used to normalise the experimental backscattered ion yield to that of the simulated backscattered ion yield (equation 2.23, page 21). An absolute determination of this calibration value was achieved via the use of a reference sample, a Si(100) crystal shallowly implanted with Cu atoms to a known concentration (3.12×10^{15} atoms cm^{-2} with a precision of $\pm 3\%$), established independently by conventional Rutherford backscattering.

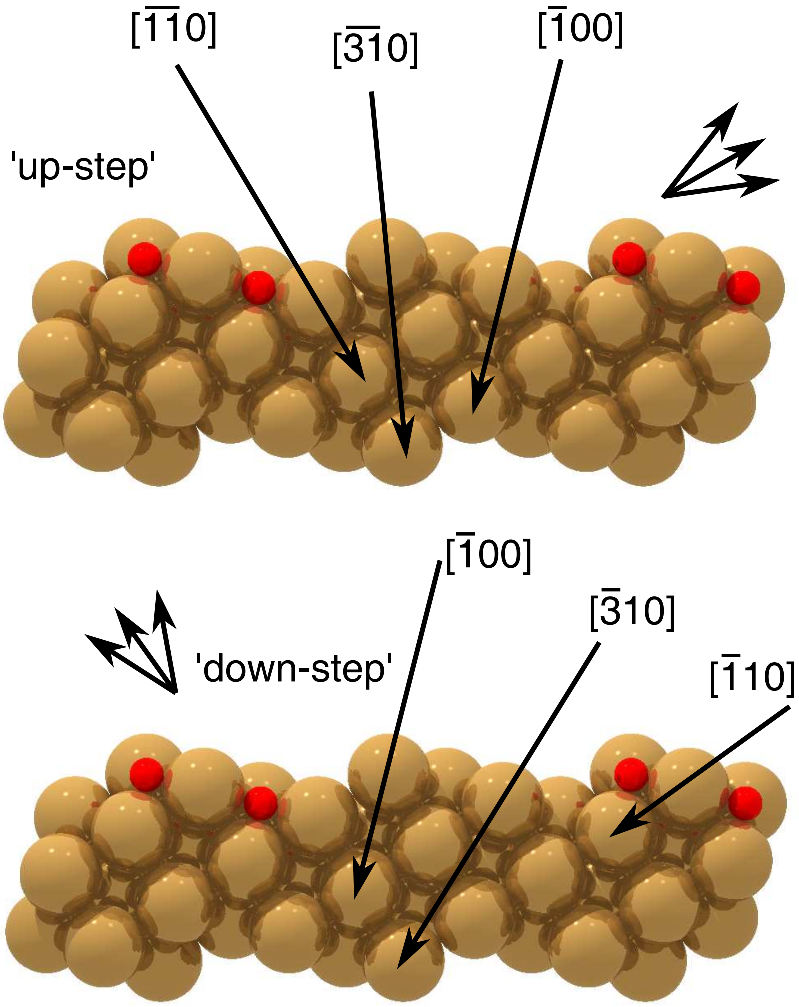

Figure 3.3: The six ion scattering geometries used in the MEIS experiment. The $\langle 110\rangle$, $\langle 110\rangle$ and $\langle 310\rangle$ incidence directions illuminate 1, 2 and 3 (100)-type surface layers respectively in a bulk continuation surface.

A brief description of the methodology involved in obtaining a scaling factor from this reference sample is given below. In order to minimise any shadowing, and therefore maximise the backscattered ion signal from the implanted Cu atoms, the reference sample is first aligned along the $[\overline{211}]$ direction (using the Si signal) and then moved $+7^\circ$ in rotation, resulting in an incidence geometry devoid of any major channelling directions (a so called ‘pseudo-random’ incidence geometry). Once the scattering signal from the Cu atoms has been corrected for the angular dependence of the Rutherford cross-section, the resulting bocking curve should be uniform with respect to scattering angle, and from this a calibration value can be derived. This calibration value must be corrected for the differing layer density of the Cu(410) surface and the different incidence angles used, as with each incidence angle a differing area of the sample is illuminated by the ion beam.

In establishing the error value associated with the scaling factor λ a number of other imprecisions must be added to the aforementioned error attached to the implanted Cu concentration. One of these arises from the fact that the Cu blocking curves from the reference sample exhibit a systematic decrease in the yield at more grazing scattering angles, a fact which can be attributed to unwanted blocking effects, even in the pseudo-random incidence geometry. In addition, from previous experience of experimental results from a range of crystalline solids, it is the case that errors can be introduced when the scaling factor is transferred to different geometries. This is perhaps due to slight misalignments of the beam, sample and detector.

In consequence of these additional errors, in this work the scaling factors associated with each of the geometries have been allowed to vary by up to $\pm 10\%$. The implications of this relaxed constraint on λ are discussed further in the next section.

3.3 Results and discussion

The experimental blocking curves obtained from the 6 different incidence geometries, the nominal 1-layer, 2-layer and 3-layer illuminations, both up-step and down-step, are shown in figure 3.4. The backscattered ion yield is expressed in terms of visible (100)-type layers. The λ calibration values used in displaying the data are fixed and are a best-estimate derived from the Cu implanted Si(100) reference sample. The major crystallographic $\langle 110 \rangle$ direction is the one along which the Cu atoms are packed the closest, as such the deepest blocking dips arise from atoms which exit the surface along this direction. Scattering of this kind occurs at 90°, 135° and 116.7° in the nominal 1, 2 and 3-layer illumination geometries respectively. In all cases the observed yield in these dips is significantly greater than that expected from 1 surface (100)-type layer. Much of the additional layer visibility can be attributed to the thermal vibrations of the atoms (of magnitude consistent with the sample being at room temperature), which leads to imperfect shadowing of the lower layers and an increase in the backscattered ion signal. In addition, small relaxations of the surface Cu atoms away from bulk-like positions will similarly illuminate some lower layer Cu atoms. Further evidence for relaxation in the Cu surface is provided by the fact that in all major experimental blocking dips, the dip minima are displaced in angle from those expected from blocking along the bulk directions (such as the angles quoted above).

Figure 3.4 also shows the results of a VEGAS simulation of the ideal bulk-terminated structure, where the sub-surface atoms (those in rows 5-10 and the underly-

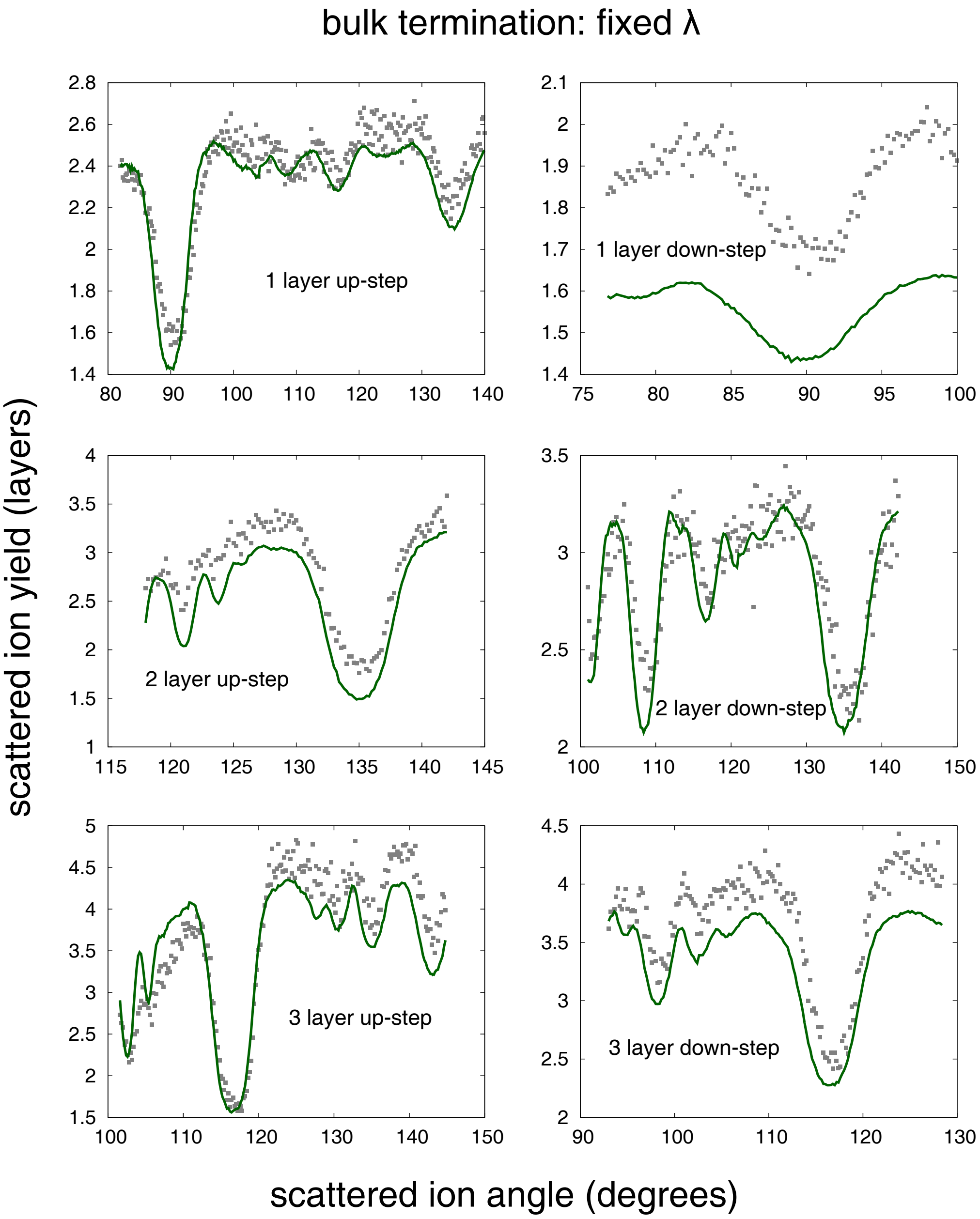

Figure 3.4: Experimental 100 keV H^+ fixed-calibration blocking curves (grey squares) obtained from the Cu(410)-O surface in the six different incidence geometries shown in figure 3.3 with the results of a VEGAS simulation in which all Cu atoms are assumed to occupy ideal bulk-like sites. The O atoms are situated in 4-fold symmetric hollow sites at heights of 0.06 Å and 0.65 Å at the step and terrace sites respectively (see 'Bulk' column in table 3.1).

ing bulk) have been assigned vibrational amplitudes derived from the Debye temperature. The atoms in rows 1-4 have been given isotropic vibrational amplitudes with a $\sqrt{2}$ enhancement. The adsorbed O atoms are assumed to occupy 4-fold symmetric hollow sites relative to the underlying substrate, at heights of 0.06 Å and 0.65 Å for the step and mid-terrace sites respectively. These heights reflect those used in the combined SXRD/DFT study [55]. It should be noted, however, that due to the fact that the O atoms are the much weaker scatterers, their contributions to the Cu blocking curves are small and as such their exact positions are not crucial in the interpretation of the simulated blocking curves.

An examination of the differences between the experimental blocking curves and those of the simulated bulk-like structure highlight the angular displacements of the experimental blocking dips away from the bulk like position, and also the general increase of experimental scattering yield in all geometries, both effects evidence of some level of surface relaxation. The proportional difference in yield is the largest in the 1 layer down-step geometry. This is because the 1 layer illumination geometries, in particular the one in the down-step direction, are the most sensitive to surface relaxations, meaning that the predicted absolute scattering yields show a strong dependence on the smallest of surface structure changes. It is however also true that these geometries show the largest fractional yield change in response to changes in the surface vibrational amplitudes.

The increased sensitivity of the 1 layer illumination geometries to surface atom vibrations and relaxations can be explained by the fact that in these geometries the closest subsurface atoms shadowed by those in the surface layer lie only one inter-atomic distance (in the case of Cu 2.56 Å) away in the shadowing direction. At this distance the shadow cone cast by the surface Cu atom is quite narrow (calculated to be 0.17 Å for the conditions in this experiment). This means that even small displacements from the expected bulk position of the shadowed atom, both static and dynamic, will result in these atoms contributing to the backscattered ion signal. In contrast in both the 2 and 3 layer illuminations the nearest shadowed atoms lie further from those atoms fully illuminated by the incident beam, and so the shadow cone radius at these positions is larger, and small displacements no longer increase the scattered ion signal. The effect of surface atomic vibrations on the expected yield is particularly evident in the case of the 1 layer incidence geometries, where in theory the expected yield in the double-alignment geometry (ions exiting along the $\langle 110 \rangle$ type direction at a scattering angle of 90°) is only 0.75 (100)-type layers, due to shadowing and blocking of the surface atoms in row 4, in the down-step and up-step directions respectively. In fact, in both of these geometries, the yield as predicted by the bulk-like VEGAS simulation is roughly double this expected value, as shown in the major 1 layer blocking dips in figure 3.4. This two-fold increase is entirely attributable to the thermal vibrations of the atoms in the surface, indeed, if the vibrational amplitude of the vibrations is greatly decreased, the resulting simulations exhibit the yields predicted by the theory.

Although it is true that the scattered ion yield changes provide useful information on the structural relaxations in the Cu(410)-O surface, it is generally the case with MEIS that the shape of the blocking curves (including the dip positions) can provide more reliable structural information. This is chiefly due to the uncertainty associated with the scaling factor λ, as discussed previously, which itself is so crucial to any yield based approach to elucidating structural information. The aforementioned $\pm10\%$ uncertainty which has been attached to λ in this experiment is by no means uncommon. For this reason the absolute yields have been given secondary importance to the shape of the blocking curves in the evaluation of different structural models in this investigation. This decision is reflected in the way in which the MEIS chi-square R-factors comparing simulation and experiment have been calculated, as explained below.

The fixed scaling factor λ for each geometry, derived from the reference sample, has been allowed to independently vary for each geometry by up to $\pm10\%$, in such a way as to minimise the overall yield discrepancy between the simulation and experimental blocking curves. In addition a 'skew' has been applied to the experimental blocking yield across the scattering angle range, likewise chosen so as to enable a better match between the experiment and theory, in this case in terms of the overall gradient on the blocking curves. This skew is justified due to the fact that systematic variations in the gradient of individual blocking curves, believed to be caused by sensitivity variations in the MEIS detector, have been observed in the experimental blocking curves obtained in many previous studies. The application of these corrections to the experimental blocking curves ensures that the remaining discrepancies between the experiment and theory (those which are reflected in the R-factor) are those which arise from the differing shapes and magnitudes of the blocking features (our primary information). It should be obvious, however, that since it is the experimental blocking curves which are modified by both of these corrections, it would not be practical or particularly informative to directly compare the simulated blocking curves of multiple model structures with the corrected experimental data on the same set of axes, as this data would be composed of several slightly different overlapping experimental blocking curves. For this reason, the experimental blocking curves shown in the figures are the un-corrected version, lacking any skew and retaining the fixed λ scaling factor derived from the reference sample unless specifically stated otherwise. With reference to the above method of R-factor calculation the combined chi-square R-factor for the bulk-terminated structure shown in figure 3.4 for all six geometries is 5.20; the value for the more sensitive 1 layer geometries alone is actually higher, and is 6.75.

As a next step, a number of models from the combined SXRD/DFT study [55], namely the previously mentioned LJ1, LJ2 and DFT models, were constructed and VEGAS simulated blocking curves produced. The structural parameter values associated with these models are given in table 3.1, and the resulting blocking curves are shown in figure 3.5. Experimental comparisons involving these three models resulted in a general reduction in the R-factors for each individual geometry, and the combined R-factors for all six geometries and for just the 1 layer illuminations all underwent a significant reduction. Those models with the lowest R-factors were the LJ2 and DFT structures, for which the total combined R-factors were 3.00 and 2.59 respectively, while the 1 layer R-factors were 2.61 and 2.87 respectively. It is also noteworthy that in terms of the absolute yield, VEGAS simulations for all of the models result in generally better agreement with the fixed calibration experimental data, although as discussed previously the quoted R-factors fail to account for this. It is clear however, that no one of the three models considered fully describes the experimental structure, and it is not immediately evident as to which of the models even best describes the data. Therefore a series of structural optimisations have been undertaken, in an attempt to find a structure which provides a better description of the MEIS data.

The structural optimisations were undertaken using the IFFCO optimisation routine, as described in chapter 2. As explained in the introduction section, it is possible to describe the surface structure of the Cu(410)-O surface using 16 distinct structural parameters, namely the displacements from bulk-like positions along the x and z axis for atoms in the first 6 (410)-type atomic rows, and a further set of z displacements for the atoms in rows 7-10. Using the IFFCO routine to optimise 16 distinct structural parameters is a daunting task, particularly if one reasonably adds a further set of parameters to describe the (potentially anisotropic) thermal vibrations of the different surface and near-surface atoms. In this case such an approach was soon found to be unrealistic, the problems being both fundamental and computational. The fundamental problem is that there may not be sufficient information contained within the six different blocking curves to uniquely define as many as 16 or more parameters, both structural and potentially vibrational. The computational problem is due to the intractability of attempting to search a box in 16 dimensional hyperspace for a single global minimum, which may not even exist (due to the fundamental problem). Instead we have decided to focus on the structural parameters which define the displacements along the z and x axis (perpendicular and parallel to the Cu(410) surface) for the outermost Cu atoms in rows 1 to 4, namely those which form the step surface. In doing so we have also fixed the vibrational amplitudes of the surface atoms to a $\sqrt{2}$ enhancement of those of the sub-surface

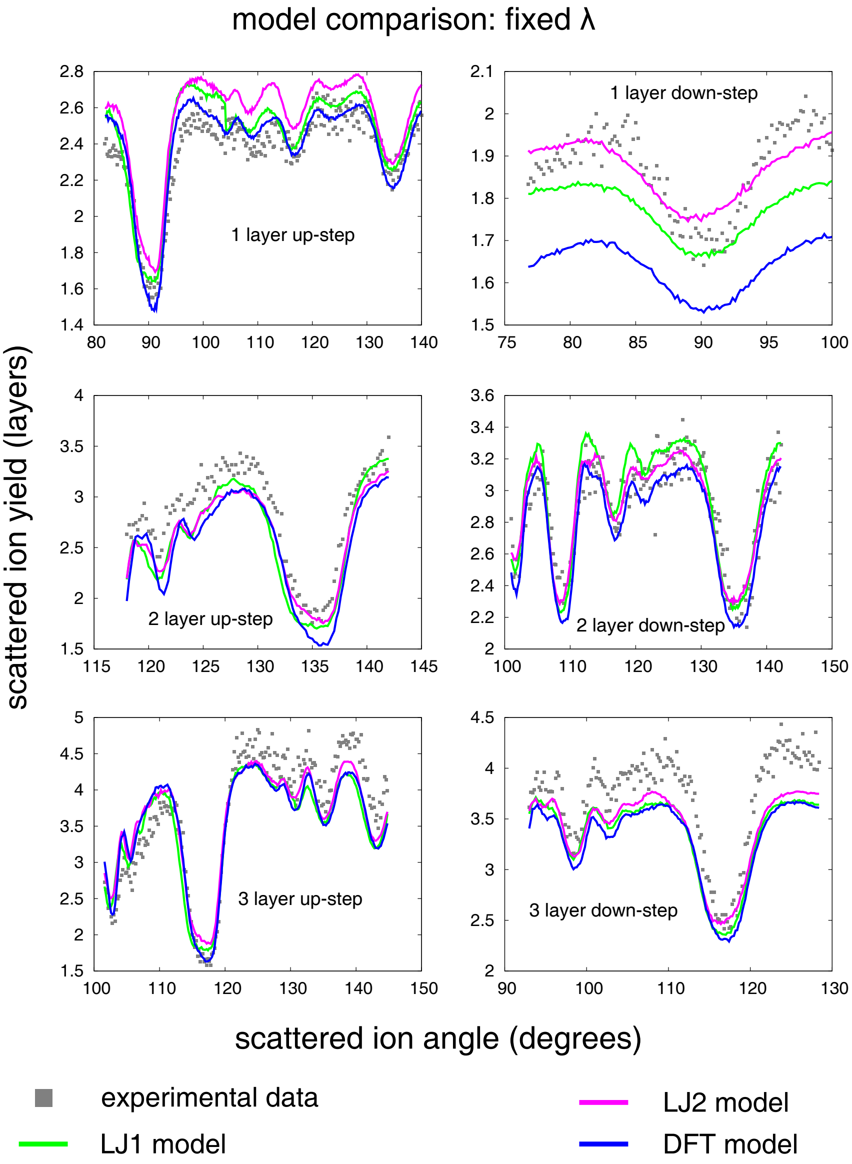

Figure 3.5: Experimental 100 keV H^+ fixed-calibration blocking curves (grey squares) obtained from the Cu(410)-O surface in the six different incidence geometries shown in figure 3.3 with the results of a series of VEGAS simulations based on the LJ1, LJ2 and DFT models proposed in the recent combined SXRD/DFT study [55] (see table 3.1 for the structural parameters associated with these models).

Row	Atom	Bulk	LJ1	LJ2	DFT	MEIS (best-fit)	MEIS (best-estimate)
Perpendicular (z) displacements (along [410] – see Fig. 3.1)							
1	Cu	0	0.16	0.15	0.11	0.21	0.27 ± 0.10
1	O	0.06	0.08	0.04	0.39	(0.04)	
2	Cu	0	0.24	0.27	0.27	0.10	0.08 ± 0.03
3	Cu	0	0.03	0.07	0.08	0.09	0.10 ± 0.02
3	O	0.65	0.72	0.59	0.83	(0.59)	
4	Cu	0	−0.12	−0.08	−0.06	0.17	0.16 ± 0.03
5	Cu	0	−0.10	−0.13	0.02	(−0.13)	
6	Cu	0	0.03	0.10	0.05	(0.10)	
7	Cu	0	−0.08	−0.10	−0.03	(−0.10)	
8	Cu	0	−0.01	0.01	−0.01	(0.01)	
9	Cu	0	−0.03	−0.05	0.03	(−0.05)	
10	Cu	0	0.05	0.06	0.01	(0.06)	
Lateral (x) displacements (along $[1\bar{4}0]$ – see Fig. 3.1)							
1	Cu	0	−0.14	−0.10	−0.07	0.00	-0.11 ± 0.11
1	O	0	−0.56	0.06	0.09	(0.06)	
2	Cu	0	0.16	0.17	0.14	−0.08	-0.05 ± 0.03
3	Cu	0	0.13	0.14	0.10	0.05	0.04 ± 0.03
3	O	0	0.11	0.20	0.27	(0.20)	
4	Cu	0	0.05	0.02	0.03	−0.01	0.02 ± 0.03
5	Cu	0	0.06	0.01	0.01	(0.01)	
6	Cu	0	0.05	0.06	0.04	(0.06)	

Table 3.1: The atomic displacements (in Å), relative to an ideal bulk termination, with O atoms occupying 4-fold symmetric adsorption sites, for the models from the recent combined SXRD and DFT study [55], alongside the results of the MEIS optimisations. The bracketed values are ones that have not been optimised and have remained unadjusted.

atoms, neglecting both anisotropy and different values for those atoms at the step edge. Although the inclusion of such parameters might well result in a better match between the simulation and experiment, it is unlikely that the optimised vibrational amplitudes would couple strongly to the structural relaxation parameters which are the main focus of this investigation. Even in the simplified situation involving the optimisation of only 8 distinct relaxation parameters, the computations still proved to be completely unfeasible, and due to their increased sensitivity to the surface relaxations, the decision was made to undertake the optimisation using only the two 1 layer illumination geometries. This being said, earlier calculations involving incremental changes from the bulk-like structure to those of the various models considered had made it clear that even in the 1 layer geometries the combined effect of the many small subsurface relaxations was substantial, both in terms of an increase in the absolute yield and angular shifts in some of the blocking dips. In order to include the effects of deeper layer relaxations in the optimisation process, four separate optimisations were conducted based on different initial structures, namely the simple bulk-like termination and the LJ1, LJ2 and DFT structural models, with the Cu atoms in rows 1 to 4 free to vary in both the z and x directions, but with all other parameters remaining fixed. In all cases these optimisations resulted in a significant lowering of not only the combined 1 layer R-factors, but reassuringly the combined total R-factors for all six geometries as well. Of the four different optimisations, that which had the initial LJ2 structure produced the both the lowest combined 1 layer R-factor at 1.23 and also the lowest total combined R-factor at 2.15. The structural parameters associated with this model, both fixed and optimised, are shown in table 3.1, where a value within brackets is one which has not been optimised but has remained fixed. The comparison between this best fit structure and the experimental blocking curves is shown in figures 3.6 and 3.7, where the normal method of showing the un-skewed experimental data with a fixed λ scaling factor is employed in figure 3.6, whereas in figure 3.7 the experimental data has been skewed and λ has been optimised. As such figure 3.7 best shows the discrepancies and similarities upon which the R-factors, and hence the optimisation itself in the case of the 1 layer geometries is based, but it is figure 3.6 which must be used when comparing the optimised model with the other models in figures 3.4 and 3.5. As might be expected, figure 3.7 shows quite good agreement between experiment and theory, but in addition figure 3.6 shows a significant improvement in the overall yield agreement in comparison to the combined SXRD/DFT models in figure 3.5 and an even greater improvement in the case of the bulk-like terminated model in figure 3.4. This yield change is particularly evident in the sensitive 1 layer down-step geometry.

As a test of the optimisation methodology adopted in this investigation, the structure was re-optimised with the tolerance on the scaling factor λ reduced to $\pm 3\%$, and

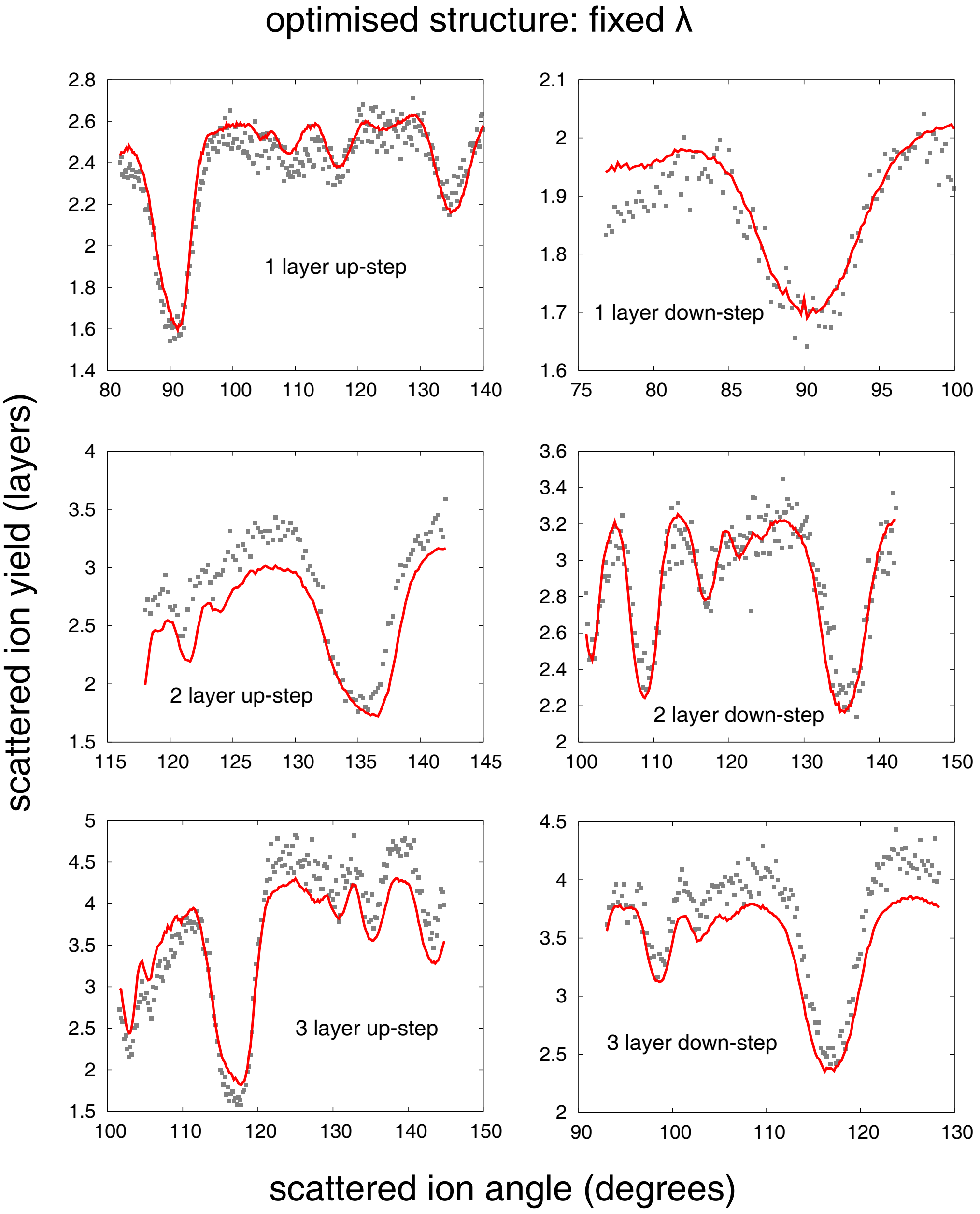

Figure 3.6: Experimental 100 keV H^+ fixed-calibration blocking curves (grey squares) obtained from the Cu(410)-O surface in the six different incidence geometries shown in figure 3.3 with the results of a VEGAS simulation of the best-fit structure (see table 3.1 for the associated structural parameter values).

likewise again but in the next instance with fixed scaling factors. While the significant 1 layer geometry yield changes could be reproduced, the shape and location of the blocking dips were in poor agreement with the experimental data, and yield discrepancies between simulation and experiment in the 2 and 3 layer geometries also failed to improve. In the light of these re-optimisations it is clear that the initial approach involving less weight being given to absolute yield agreement was the correct one.

Before any discussion concerning the results of the MEIS structural optimisation can be made, it is first necessary to assign some measure of precision and confidence to each optimised structural parameter. The standard procedure for calculating the uncertainties on a set of optimised parameters, involving R-factor curves for each parameter, is explained in more detail in chapter 2. However, in the case of the present investigation, which involves a large number of optimised parameters, some of which may be coupled, it is by no means certain that the standard method is the best way of defining the confidence limits. In this investigation, therefore, an alternative approach has been used, that is to ask how stable the optimised structural values are with respect to those parameters which have remained fixed (i.e. the sub-surface atom displacements for the four different initial structures). Table 3.1 shows the MEIS best-estimate optimised structural parameter values, alongside those for the best-fit structure, where the best-estimate value represents an estimated mean value based on all four optimisations, and the accompanying error is the scatter of these optimised parameter values.

It was found to be the case that the optimised parameter values for the four optimisations were on the whole in good agreement, this is reflected in the generally modest scatter values found in the MEIS best-estimate column in table 3.1. The same table highlights, however, that there are some significant differences between this study's optimised values and those which were found in the combined SXRD/DFT study. Most notable of these is the displacement perpendicular to the surface of the Cu atoms in the 4th row, these atoms occupying the surface sites closest to the bottom of the steps. All three models from the previous study favour an inward (negative) displacement for these atoms, whereas in the current study an outward relaxation is the preferred result. As these atoms can be considered second layer atoms with respect to the (100) terrace above, an outward displacement of significant magnitude might necessitate a similarly large outward displacement of the row 1 Cu atoms, as it is these atoms which partially cover the row 4 atoms below. This study does find that the Cu row 1 atoms prefer to sit further outwards from their bulk positions than the same Cu atoms in the previous studies, by an amount similar in magnitude to that of the row 4 atom displacement. In this respect, then, the MEIS results are shown to be self-consistent. Another dissimilarity between the results of this study and those of the previous investigations is in the relaxation of the row 2

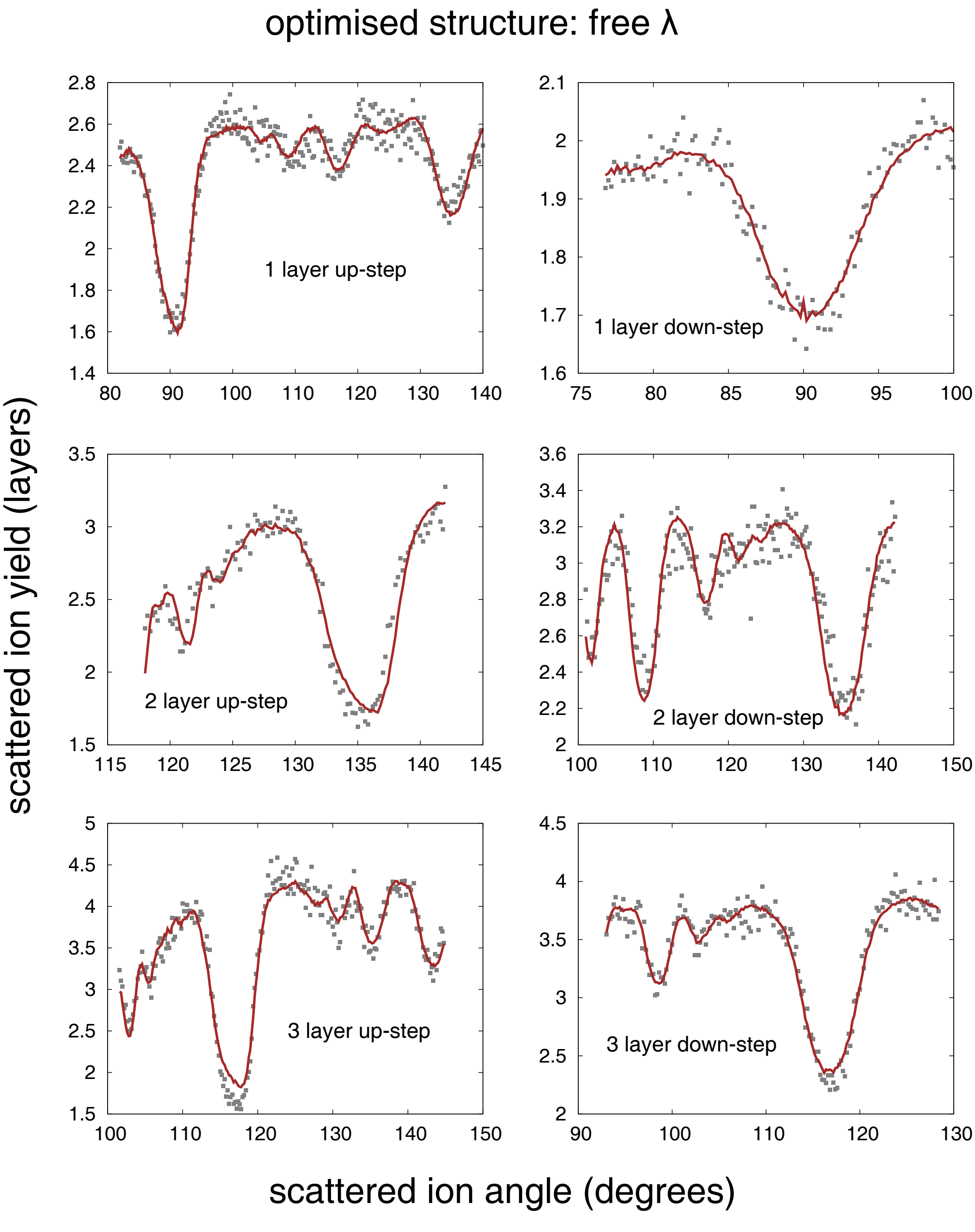

Figure 3.7: Experimental 100 keV H^+ blocking curves (grey squares) calibrated with freely optimised λ scaling factors and an overall 'skew' so as to better fit the results of a VEGAS simulation of the best-fit structure (compare with figure 3.6).

Cu atoms, which with the MEIS results are shown to undergo small shifts both outwards from the surface and laterally towards the step edge. In contrast, these same atoms are shifted laterally away from the step edge in the previous favoured models, and are displaced outwards perpendicularly from the surface to a greater extent.

One of the largest discrepancies between the experiment and theory blocking curves evident in figure 3.7 is that of the major blocking dip position in the 2 layer illumination up-step geometry, at nominally 135°, which corresponds to blocking along the major $\langle 110 \rangle$ outgoing direction. One possible explanation for this is the fact that in this geometry, in contrast to the optimised 1 layer down-step geometry the row 4 Cu atoms are fully illuminated by the 2 layer incidence beam. These atoms' positions, which as noted previously are in disagreement with the previous SXRD/DFT study, have perhaps less effect on the 1 layer down-step blocking curves, and as such the optimisation may be less sensitive to these row 4 Cu atom displacements. On the other hand, VEGAS simulations have shown that even in the 1 layer down-step geometry these row 4 Cu atoms still receive a significant amount of illumination, due to both relaxation and thermal vibrations. As such the true picture is certainly more complex, and some blocking curve discrepancies might only be resolved if all six geometries were simultaneously optimised.

The results found in this study should be compared with those of an earlier ion scattering investigation by Coen et al. [54] of the Cu(410)-O surface. This MEIS study was rather different, using heavier 200 keV He^+ ions incident in the $[\bar{1}00]$ direction only (normal incidence with respect to the (100) terraces, illuminating 2 (100) type layers). Blocking curves, each consisting of one major blocking dip, were collected in two geometries centred around the down-step [110] direction and the [011] direction within the (100) terraces. This greatly reduced quantity of information, although treated with very precise fitting, had the effect of constraining the type of structural models which could be evaluated. Only perpendicular displacements (with respect to the (100) terraces) of the outermost 4 Cu atom rows (rows 1 to 4 in figure 3.1) were considered, excepting the step edge Cu atoms in row 1, which were allowed a fixed lateral relaxation (in the (100) plane) away from the step edge. The three models are outlined below:

1. Row 1 Cu atoms were displaced outwards from the surface by 0.25 Å and laterally away from the step edges by 0.185 Å. Cu atoms in rows 2 to 4 remained in bulk-like positions.
2. Cu atoms in rows 1 to 4 were displaced outwards from the surface by 0.12 Å and row 1 Cu atoms were displaced laterally away from the step edges by 0.185 Å.
3. Row 1 Cu atoms were displaced outwards from the surface by 0.15 Å and laterally away from the step edges by 0.185 Å. Cu atoms in rows 2 to 4 were relaxed

outwards from the surface by 0.07 Å.

The general trend of these results is indeed consistent with all of the results shown in table 3.1, however the fact that the models tested by Coen et al. had such heavy constraints make a more detailed comparison of the two experiments unrealistic. It should also be noted that in the previous MEIS study it was concluded that there was enhanced surface atomic disorder, this being simulated by significantly increasing the vibrational amplitudes of the surface atoms. In this way they were able to increase the theoretically predicted yields to better match those of the experiment. In this work this enhancement of the theoretical yield is achieved via the inclusion of sub-surface atom relaxations as implied by the SXRD/DFT studies, without any need to assume increased surface disorder, be it static or dynamic. This is consistent with the STM studies [49] which show that the Cu(410)-O surface is in fact very well-ordered.

A comparison can be made between the relaxation parameters associated with the Cu atoms in rows 1 and 2 in this investigation and the equivalent 'edge' and 'centre' row Cu atom parameters in the Cu(100)($\sqrt{2} \times 2\sqrt{2}$)R45°-O surface. In this structure the Cu atoms adjacent to the missing rows, whose local environment matches the row 1 step edge atoms in Cu(410)-O, have been found to be outwardly relaxed in a number of previous studies. In two different quantitative LEED studies these relaxations were 0.28 Å [61] and 0.50 Å [62], while a photoelectron diffraction investigation found a value of 0.21 Å [59] (although the latter involved a large associated error). These same studies found lateral displacements of these atoms towards the missing Cu row (equivalent to away from the step edge in the case of the Cu(410)-O) of 0.30, 0.10 and 0.29 Å respectively. In another study [46], this time using surface X-Ray diffraction (SXRD), where only the lateral displacements were investigated, two alternative displacements of 0.25 and 0.31 Å were suggested. On the whole these displacements are rather larger than the equivalent ones on the Cu(410)-O surface, as even though the perpendicular relaxations are of similar size to those given in this MEIS study, the lateral relaxations are significantly larger. In terms of the 'centre' row on the Cu(100)($\sqrt{2} \times 2\sqrt{2}$)R45°-O surface and its row 2 equivalent in Cu(410)-O, a direct comparison is less meaningful, due to the fact that in the (410) surface there are no lateral constraints on the Cu atoms, whereas symmetry arguments in the case of the (100) surface imply lateral movements would be unfavourable.

3.4 Conclusions

The Cu(410)-O stepped surface has been investigated using medium energy ion scattering (MEIS), using 100 keV H^+ ions, in several geometries giving rise to six distinct blocking curves. The asymmetry of the surface was exploited to enable data to be taken in both the ‘up-step’ and ‘down-step’ directions, which are equivalent directions with respect to the (100) terraces, but possess a uniqueness on the (410) surface. A range of different structural models were tested by simulating the blocking curves via use of the VEGAS computer code. These models involved sixteen distinct structural parameters which together define the structure of the near surface region, furthermore eight structural parameters corresponding to those atoms which lie directly at the surface were optimised using the IFFCO optimisation routine. The results found in this study are in broad agreement with those of a previous combined SXRD/DFT investigation, nevertheless, some significant quantitative differences remain. These results also show somewhat smaller surface relaxations than those attributed by a number of previous studies to the Cu(100)($\sqrt{2} \times 2\sqrt{2}$)R45°-O ‘missing row’ structure, a structure related to that of the Cu(410)-O surface by the similarities of the local atomic environments.

Chapter 4

Methylthiolate induced lateral distortion on the Cu(100) surface

4.1 Introduction

Self-assembled monolayers (SAMs), which can be formed by the interaction of n-alkanethiols ($CH_3(CH_2)_{n-1}SH$) with coinage metal (Cu, Ag and Au) surfaces have been intensively studied for $\sim$ 20 years [63–67]. The formation of a SAM in ultra-high vacuum (UHV) is most often achieved by introducing the n-alkanethiol in the gas phase to the metal surface, whereupon, following deprotonation, the resulting thiolate ($CH_3(CH_2)_{n-1}S$) bonds to the metal surface via the S head-group, with the adsorbed molecules spontaneously ordering into regular periodic structures. Such structures have a wide range of realised and potential applications, such as electronic materials and chemical and biochemical sensors (e.g. [68–70]), often involving the functionalisation of the end-group. The majority of the research conducted to date has been focused on the Au(111) surface, in part due to the fact that such surfaces can be readily produced by physical vapour deposition or sputtering, but also because the Au surface is particularly insensitive to other species. There has, however, been a significant amount of research directed at thiolate SAMs formed on the Ag and Cu surfaces, although until recently there have been very few quantitative structural studies. Nonetheless, there is now substantial evidence that the adsorbed thiolates induce major reconstructions on the (111) surfaces of all three coinage metals [71]. Of particular interest is the thiolate-induced modification of the Cu(111) surface, the first surface to provide strong evidence for the aforementioned major reconstructions [72]. In this case the adsorption of the thiolate molecule triggers a reconstruction of the outermost Cu atomic layer, which adopts a near-square pseudo-(100) structure, with the S head-group bonding to the surface in four-fold coordinated hollow sites. This reconstruction has been characterised in great detail, not only for methylthiolate ($n = 1$) [73, 74], but also for octanethiolate ($n = 8$) [75, 76]. The adsorbate-induced pseudo-(100) surface reconstruction has additionally been observed for a number of atomic adsorbates on Cu and Ni surfaces [77]. The most plausible explanation for the occurrence of this reconstruction is that adsorption in the (100)-type four-fold coodinated hollow site is much more energetically favourable than adsorption in (111)-type 3-fold coordinated hollow site, to the extent that the energy barrier associated with the creation of a pseudo-(100) reconstructed layer over a mismatched (111)-type substrate layer can be overcome. Indeed, the results of a density functional theory study [78] do find that for methylthiolate adsorbed on Cu(111) and Cu(100), it is the four-fold coordinated hollow site of the Cu(100) surface which has the greatest stability. However it is only more recently that direct quantitative support for the energetic advantage of a pseudo-(100) reconstruction has been found, in the case of nitrogen adsorbed on Cu(111) [79].

One implication of the argument stated above is that if an adsorbate occupies a 4-fold coordinated hollow site in a pseudo-(100) reconstructed surface, it should adsorb onto the pure (100) face of that material in the same hollow site. This has been shown to be true in the case of a number of n-alkanethiols [80–83], and additionally for two aromatic thiols, namely benzenethiol [84] and 2-mercaptobenzoazole (MBO) [85]. There is, however, an unusual aspect of the alkanethiolate induced pseudo-(100) reconstruction on Cu(111), namely that the Cu-Cu neighbour spacing in the reconstructed layer is significantly ($\sim 15\%$) greater than that in the Cu(100) surface, an aspect not evident in other pseudo-(100) reconstructions, for which the inter-atomic spacings in the reconstruction and the (100) face tend to be much more similar. In most cases the pseudo-(100) reconstructed layer in a particular system is incommensurate with the substrate, or the two posses a large commensurate mesh; as such the reconstructed layer might be expected to adopt a periodicity which is not particularly constrained by that of the underlying substrate. This is not the case with the unreconstructed Cu(100) surface, and so, considering the large inter-atomic spacing adopted in the pseudo-(100) reconstruction on Cu(111), one might expect that the adsorption of alkanethiolate on the Cu(100) surface would lead to considerable lateral compressive stress in the outermost surface layer. This stress could lead to local surface strain, given an adsorbate structure periodicity which would permit such movement. This local surface strain effect on the Cu(100) surface will be explored in the remainder of this chapter.

In all of the cases mentioned above in which a thiolate is adsorbed on the Cu(100) surface, there exists a (2×2) phase at a coverage of 0.25 ML (see figure 4.1). In addition, at higher coverages most of these systems show a $c(2 \times 6)$ phase which can be thought

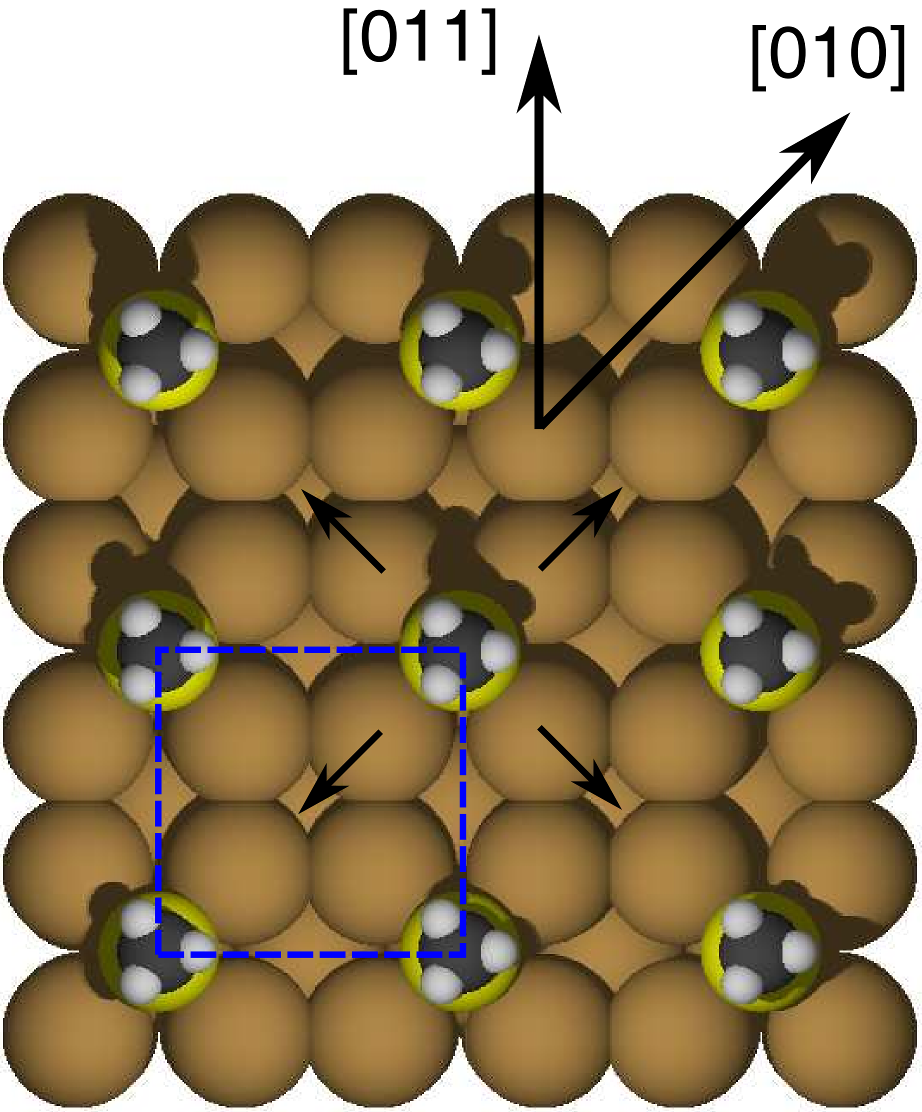

Figure 4.1: Plan view of the Cu(100)(2 × 2)-CH_3S surface, showing both the two pertinent azimuths and a superimposed square representing the (2 × 2) unit mesh. The short arrows highlight the proposed lateral outward radial displacements (shown here with a value $\Delta_{xy} = 0.15$ Å) of the Cu surface atoms surrounding the adsorbed methylthiolate species.

of as a faulted c(2 × 2) phase, with the extended periodicity being attributed to either a periodic rumpling of the surface [86], or a periodic adsorbate vacancy array [82]. In fact the c(2 × 2) phase with the adsorbates situated in the 4-fold hollow sites is a common one on face centred cubic (fcc) metal (100) surfaces. In this structure, which has a coverage of 0.5 ML, each metal surface atom lies midway between two adsorbate species, and therefore a radial outward lateral shift of each metal atom in order to relieve the local compressive stress is not possible, as a movement in this manner from one adsorbate species is a movement towards another. By contrast, in the lower coverage 0.25 ML (2×2) phase, outward lateral relaxations as described above are permissible in terms of the surface structure.

It is this (2×2) phase in the Cu(100)-CH_3S system which is the subject of the current investigation, and the aim is to establish if such lateral relaxations occur. The medium energy ion scattering (MEIS) technique is particularly suited to identifying adsorbate induced surface structural relaxations of the kind expected in the Cu(100)(2×2)-CH_3S phase. Not only do small displacements of surface Cu atoms give rise to shifts in the positions of the dips in the MEIS blocking curves, but small atomic shifts away from the bulk like positions in selective incidence geometries give rise to an enhanced scattering yield due to increased illumination of the lower substrate layers. It is this latter aspect of MEIS which is exploited most in the work presented in this chapter.

4.2 Experimental details

The MEIS experiments upon which this chapter is based were taken at the national MEIS facility at the Daresbury laboratory, UK. The Cu(100) single crystal sample used in this study was formed via spark-machining from a single crystal Cu bar, followed by mechanical polishing using successively finer grades of diamond paste. Upon loading into the ultra-high vacuum (UHV) chamber system at the facility, the sample was prepared and cleaned *in situ* in the usual manner, involving repeated cycles of 1.5 keV Ar^+ ion bombardment at grazing incidence trajectories followed by annealing to $\sim 500°C$ within a routine chamber base pressure of $\sim 2.0 \times 10^{-10}$ mbar. The sample was judged to be well-ordered and free from contaminants when a (1×1) LEED pattern with sharp spots was observed, and Auger electron spectra obtained from the sample showed only the peaks expected from a clean Cu surface. The Cu(100)(2×2)-CH_3S system was prepared by exposing the clean Cu(100) surface to dimethyldisulphide (DMDS - (CH_3S-SCH_3)), which breaks up in the presence of metal surfaces to form two methylthiolate species, via the scission of the S-S bond, which then bond to the surface through the S head-group. The DMDS liquid, placed within a glass ampoule, was mounted onto an externally pumped line attached to the MEIS preparation chamber, and was purified by means of several freeze/thaw pumping cycles. This allowed the DMDS to be introduced in vapour form to the sample in the preparation chamber via a leak valve. The sample, being held at room temperature, was then exposed to a DMDS partial pressure of 1.0-2.0 $\times 10^{-6}$ mbar. This resulted in total exposures in the range 3.6-7.2 $\times 10^{-3}$ mbar $\cdot$ s. As thiolate SAMs are known to be susceptible to electron-beam radiation damage, LEED was only used on the surface *after* the MEIS measurements, at which time a clear (2×2) pattern was observed. Despite the high exposures used, no LEED spots indicative of the high-coverage c(2×6) phase were seen. In the 100 keV H^+ ion MEIS spectra taken on the dosed surface, relative intensities of the S and Cu energy peaks taken in the surface-specific 'double alignment' geometry ($[\bar{1}10]$ incidence, [110] exit) indicated a S coverage of between 0.31 ML and 0.36 ML. Although these values are somewhat higher than the expected 0.25 ML coverage for the (2×2) phase, they are significantly lower than the 0.5 ML expected for the c(2×6) high-coverage phase.

MEIS blocking curves using 100 keV H^+ ions were obtained for both the clean Cu(100) surface and the Cu(100)(2×2)-CH_3S system in such a manner as to limit the total flux on a particular region of the sample to $4\,\mu$C (expressed in terms of the 'drain current - see chapter 2 for a more detailed description). In taking such a precaution, no evidence was seen in either the MEIS data or the subsequent LEED pattern of ion beam induced damage to the surface region. As is usual, the blocking curves for both the clean and methylthiolate-(2×2) surface represent the scattered ion yield from the surface Cu atoms. Despite the fact that the signal from the S scattering was sufficient to extract some surface stochiometry information, the low number of detected ion counts precluded the possibility of producing S blocking curves. These low scattering fluxes are typical of a target atom such as S with a relatively low scattering cross-section (which scales with the square of the target atomic number, Z). For the same reason, it is not possible to measure blocking curves with meaningful statistics using the scattered ion signal from both the H and C atoms in the methylthiolate species, for which the cross-sectional dependence problem is even more severe.

The experimental blocking curves were obtained in three distinct ion incidence geometries, namely along the $[\bar{1}10]$ direction and the $[\bar{1}00]$ direction in the [010] azimuth, and along the $[\bar{2}11]$ direction in the [011] azimuth. These geometries are shown in figure 4.2, with the two azimuths also defined in figure 4.1. With reference to figure 4.2, it is clear that in the $[\bar{1}10]$ incidence direction the ion beam would illuminate only the outermost Cu layer in the absence of any Cu atom displacements or thermal vibrations, as the atoms in the deeper layers are shadowed by those in the surface layer. As such this incidence geometry is referred to as a one layer illumination. Similarly, the two other incidence geometries are both 2 layer illuminations. Note that in both azimuths shown in figure 4.2, half of the atoms shown are in a different scattering plane than those shown in front. In the case of the [010] azimuth, those atoms in the plane behind are in equivalent positions (with respect to the incident ions) to those in the plane in front, and as such one need only consider the front-most plane when considering ion beam illumination.

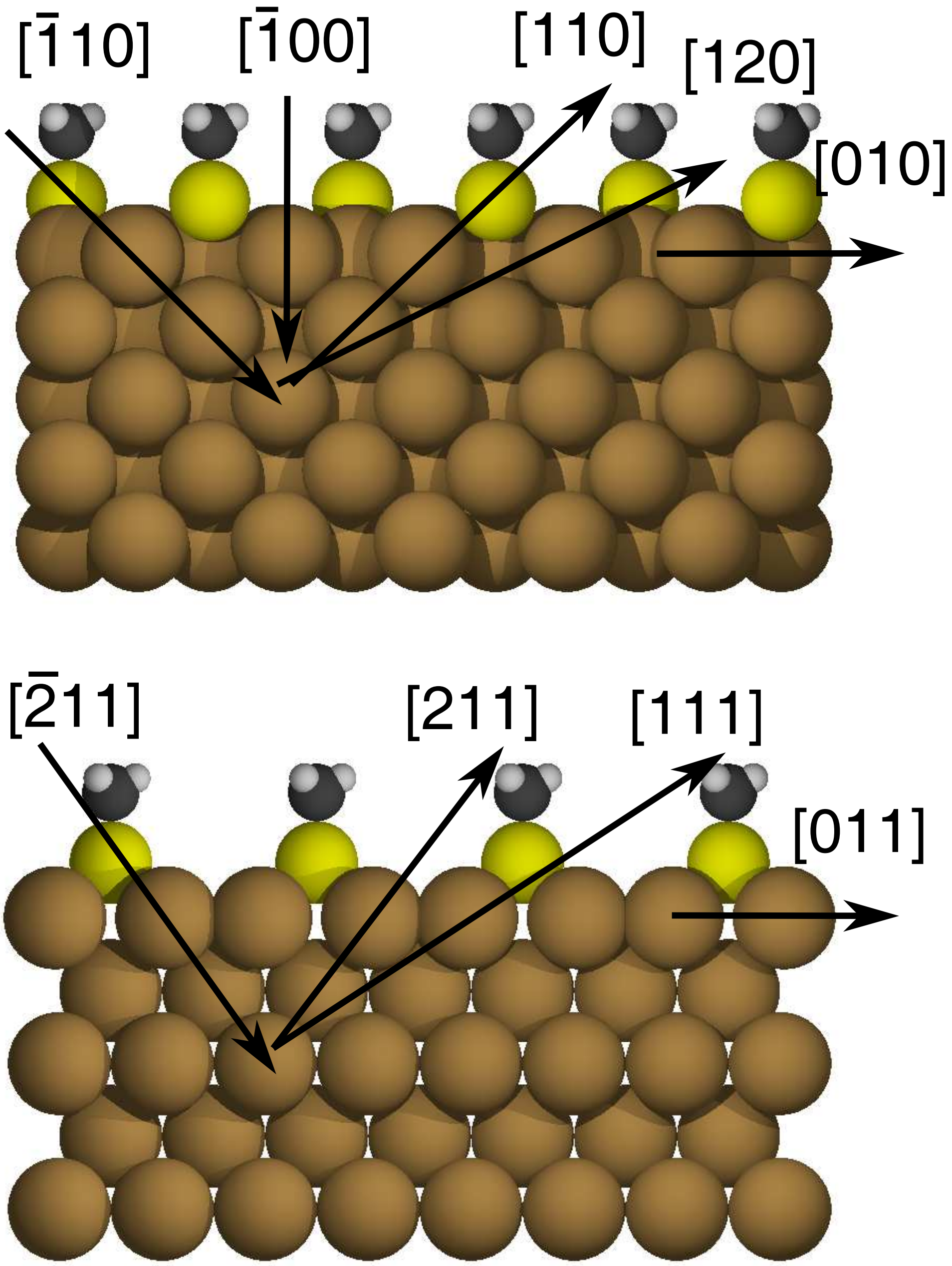

Figure 4.2: Side views of the [010] and [011] azimuthal scattering planes of the Cu(100)(2 × 2)-CH$_3$S surface showing the ion incidence and major bulk blocking exit directions utilised in this medium energy ion scattering study.

By contrast, for the [011] azimuth, the atoms in the rearmost plane are those in the even numbered layers (2nd, 4th, etc.), whilst those in front are atoms in odd numbered layers. Thus in the [$\bar{2}$11] incidence geometry 2 layers are fully illuminated by the ion beam, even though in each scattering plane any subsurface layer is shadowed by the layer above. Choosing geometries which fully illuminate very few layers ensures that any lateral displacements of the surface atoms leads to a loss of shadowing of the deeper layers and consequentially an experimentally observable increase in the scattered ion yield. In practice, the thermal vibrations of the Cu atoms ensure that some atoms in lower layers are illuminated even with structural models in which all atoms occupy bulk-like positions. Nevertheless, the incidence geometries in this experiment, in particular that of the $[\bar{1}10]$ 1 layer illumination, show a high degree of sensitivity to surface relaxations.

As with all MEIS experiments, determination of the scaling factor λ, which enables the experimental scattered ion yield to be expressed in terms of the number of visible atomic layers, is of key importance. As is usual, a reference sample of Si(100) shallowly implanted with Cu atoms to a known concentration was used to calibrate the backscattered ion yield (find a value for λ) for the blocking curves obtained from the clean and dosed Cu(100). A more detailed description of the methodology involved in the use of this reference sample to calculate λ scaling factor values is given in chapter 3. An important concern when obtaining a λ value in this manner is that of the error attached to λ, which is normally estimated to have a value of $\pm 10\%$. However, since it is the relative *differences* in the scattered ion yield of the clean and thiolate covered surfaces that are of interest in the current study, the λ values extracted from the reference sample were refined via the matching of the clean surface experimental yield to that of a VEGAS simulation of the clean surface.

4.3 Results and discussion

Figures 4.3, 4.4 and 4.5 show the experiment blocking curves for both the clean Cu(100) surface and the Cu(100)(2×2)-CH_3S, along with the results of VEGAS simulations for a number of different structural models. In both the $[\bar{2}11]$ (figure 4.3) and $[\bar{1}10]$ (figure 4.5) geometries there is a clear increase in the scattered ion yield when comparing the clean and dosed surface blocking curves. Both effects can be attributed to adsorbate induced surface Cu atom displacements, which must be greater than any small Cu atom displacements expected on the clean surface. By contrast, in the $[\bar{1}00]$ incidence geometry the scattering yield remains almost unchanged upon the adsorption of the methylthiolate species. With reference to figure 4.2 we are reminded that in this nominal 2 layer illumination the ions are incident along the surface normal, and as such one would expect any overall scattering yield change in this geometry to reflect only lateral atom movements, because any perpendicular movement of the atoms would not result in any increase in the illumination of the subsurface layers. This is in contrast to the other

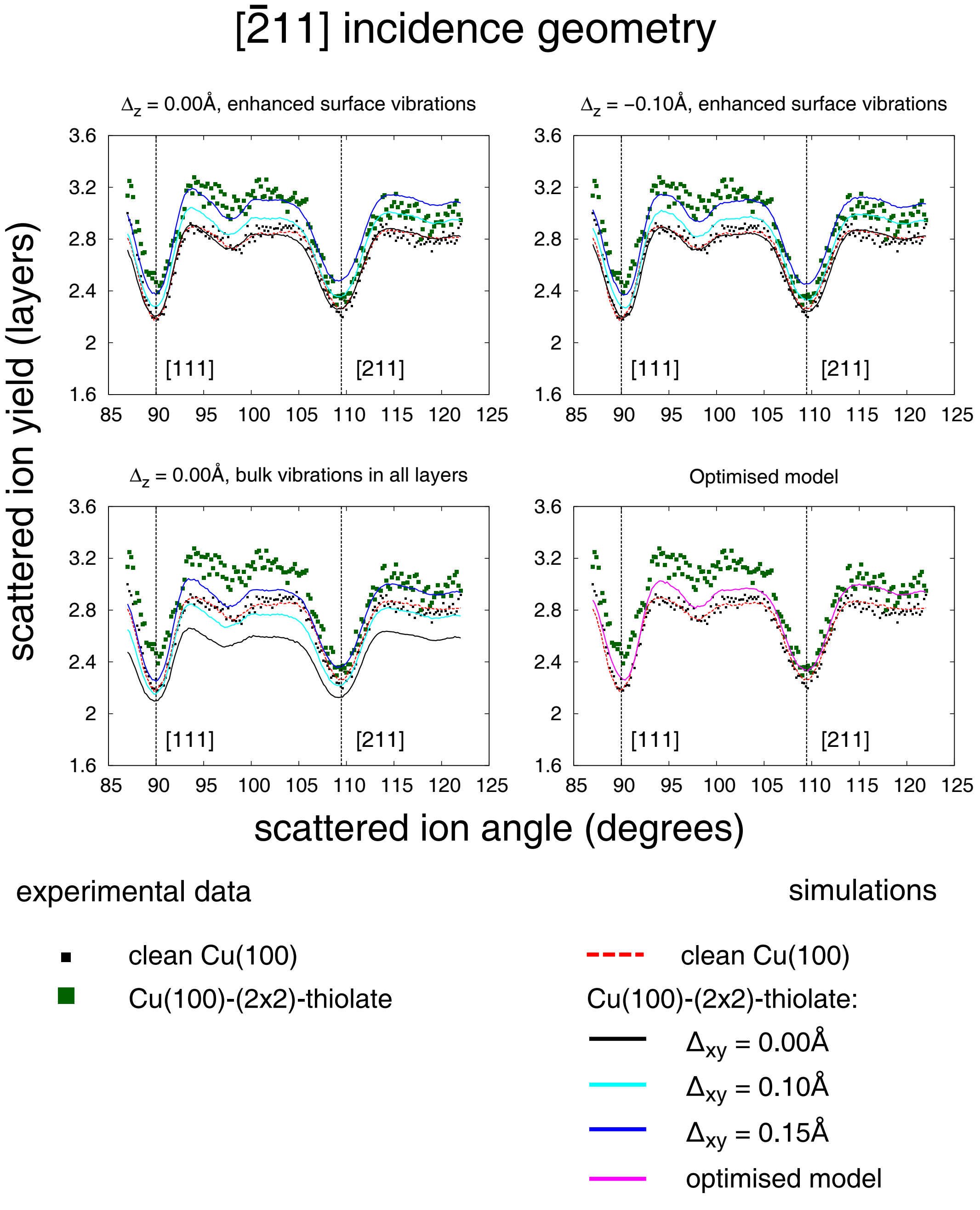

Figure 4.3: Comparison of the experimental blocking curves for both the clean Cu(100) and Cu(100)(2 × 2)-CH_3S surfaces in the [$\bar{2}$11] incidence geometry, with the results of various simulated models exploring the effects of surface relaxation, including both radial lateral movement (Δ_{xy}) and perpendicular movement (Δ_z) of the surface Cu atoms.

two geometries, in which we are in principle sensitive to Cu surface atom movements both parallel and perpendicular to the surface plane. Indeed this $[\bar{1}00]$ normal incidence geometry was selected as a potential way to distinguish between the two different types of surface Cu atom movement. Given the lack of a significant change in the Cu scattering yield in this geometry, this might be taken at first glance to be evidence of a lack of lateral Cu atom relaxation. However, the VEGAS simulations show that upon the adsorption of the thiolate adlayer, the expected yield change from that of the clean surface actually *decreases* in the absence of any Cu atom displacements, simply due to the effects of some shadowing by the S head-group atoms. In the light of this fact, the lack of any yield change in the $[\bar{1}00]$ geometry upon the addition of the adsorbate can in fact be regarded as evidence of some Cu atom movement parallel to the surface due to the increased subsurface illumination. Therefore we take this result as evidence of lateral surface distortion on the Cu(100)(2×2)-CH_3S surface.

In each panel in the figures 4.3, 4.4 and 4.5, the results of a VEGAS simulation of the clean Cu(100) surface are presented. As mentioned previously, it is these simulated blocking curves which have been used to fine-tune the absolute yield calibration. The final λ scaling factor value derived in this manner is therefore influenced by both the amplitude of the thermal vibrations and the surface relaxation values used in the clean VEGAS model. The root-mean-square (rms) vibrational amplitudes in the subsurface layers were set to 0.079 Å (consistent with the bulk Debye temperature), with the vibrations in the surface layer enhanced (isotropically) by a factor of $\sqrt{2}$. The outermost inter-layer spacing was contracted by 2.4%, whilst the spacing between the 2nd and 3rd atomic layers was expanded by 1%. These surface relaxations are those found in an earlier study of the clean Cu(100) surface using MEIS [87], values similar to those obtained in a number of LEED studies (e.g. [88, 89]). The isotropic surface layer rms vibrations used are representative of the typical values found in a range of surface studies. The aforementioned MEIS study [87] found larger surface vibrational enhancements ($\sim 80\%$), but the effect of this enhancement on the scattering yield was somewhat offset by the inclusion of correlated vibration effects. In this same study evidence was found for an unusual anisotropy within the surface vibrations, the vibrational amplitude parallel to the surface plane being found to exceed that in the perpendicular direction. Due to the fact that the focus of this study is the *relative* yield change upon adsorption of the methylthiolate species, the exact parameter values used in the modelling of the surface vibration effects are not crucial, although some consideration of possible adsorbate-induced changes to the surface vibrational amplitudes is necessary.

The first set of simulated models exploring possible thiolate-covered surface reconstructions have their blocking curves presented in the upper-left panel in each of

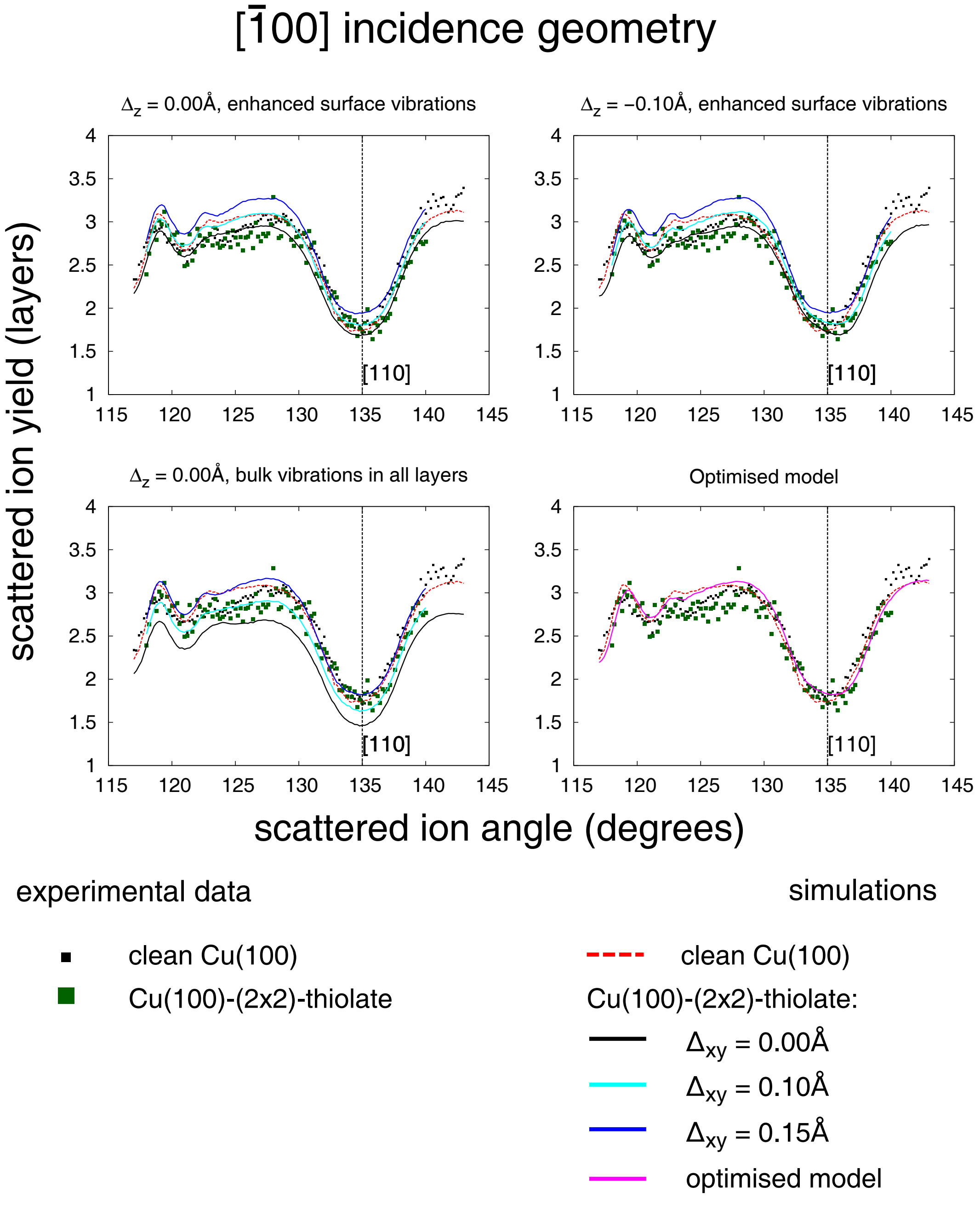

Figure 4.4: Comparison of the experimental blocking curves for both the clean Cu(100) and Cu(100)(2 × 2)-CH_3S surfaces in the [$\bar{1}$00] incidence geometry, with the results of various simulated models exploring the effects of surface relaxation, including both radial lateral movement (Δ_{xy}) and perpendicular movement (Δ_z) of the surface Cu atoms.

the three incidence geometry figures (figures 4.3, 4.4 and 4.5). In these simulations all layer-spacing values were set to those of the bulk, and the thermal vibrational amplitudes were those used in the simulation of the clean surface, with the characteristic $\sqrt{2}$ enhancement in the surface layer. Three different values for the (outward) radial lateral relaxation of the surface Cu atoms around the S head-group (Δ_{xy}) are explored, namely no such relaxation at all ($\Delta_{xy} = 0.00\,\text{Å}$) and values of $\Delta_{xy} = 0.10\,\text{Å}$ and $\Delta_{xy} = 0.15\,\text{Å}$. These simulations include the shadowing and blocking effects of the S head-group atoms located within the 4-fold hollow sites, giving rise to the (2×2) surface periodicity and its adsorbate coverage of 0.25 ML. The S atoms are situated at heights of 1.37 Å above the surface plane, these values reflecting those found in one of the previous studies [81]. The calculations do not consider the scattering of the C and H atoms of the methylthiolate due to the weak nature of this scattering and the fact that they are not located in the high-symmetry sites in which they would need to sit in order to shadow or block ions scattering from nearby Cu atoms. In such a system it should be noted that the simulated blocking curves corresponding to the case of $\Delta_{xy} = 0.00\,\text{Å}$ in this first panel are those which show the scattering yield expected in a bulk-terminated structure with no increased illumination due to any Cu atom structural movements, although including the influence of shadowing by the S head-group atoms lowers this yield. In all cases these simulations therefore show a decrease in the expected Cu scattering signal from that of the clean surface, the largest of which is in the $[\bar{1}00]$ geometry (figure 4.4). The much smaller scattering yield decrease in the other two geometries can be mainly attributed to the reduced S shadowing in these geometries due to the fact that the S atoms do not occupy bulk-like sites in terms of their heights above the surface. As the $[\bar{1}00]$ geometry is insensitive to this height mismatch, the S atoms will fully shadow one quarter of all the 'chains' of Cu atoms perpendicular to the surface. Because the experimental data do not show this predicted decrease in yield in the 2 layer $[\bar{1}00]$ illumination, we can infer that some lateral movement of the Cu atoms has occurred, in a manner consistent with the large observed experimental yield increase in the other two geometries. The changes in the experimental scattered ion yield upon methylthiolate adsorption appear to be consistent in all three geometries with a value for Δ_{xy} in the range 0.10-0.15 Å. A point worth stressing is that the differing yield changes in each of the incidence geometries' simulated blocking curves are the result of the same change in the surface relaxation parameters. This effect can be attributed to the differing widths of the shadow cones cast in equivalent subsurface layers in each of the three geometries. These differing widths are due to the different inter-atomic distances along the ion incidence trajectories in each of these geometries. As the shadow cone broadens as a function of distance, so the subsurface atoms which lie closest to the surface shadower atom in the direction of the ion beam receive a greater illumination as a consequence of both a small surface atom displacement and the rms thermal vibrations of the two atoms in question. Furthermore it is noteworthy that the scales on the ordinate axes differ in the three geometries, giving rise to an additional apparent differences in yield. This effect is most evident in the case of the $[\bar{1}00]$ incidence, a nominally 2 layer illumination with a particularly large blocking dip, for which seemingly small yield changes are in fact somewhat larger when one considers the yield scale on the ordinate axis.

In order to further explore the Cu surface relaxation, the second set of panels on the upper right in figures 4.3, 4.4 and 4.5 shows the dosed surface simulations which result from an outward 0.1 Å perpendicular relaxation, in addition to the various lateral relaxations. The effect of this added perpendicular relaxation on the adsorbate-induced yield change is relatively small, however it does result in some angular shifts in the blocking dips, resulting in a significantly better fit between experiment and theory. This is most evident in the case of the [120] blocking dip within the $[\bar{1}10]$ incidence geometry, but also in that of the [111] exit direction with $[\bar{2}11]$ incident ions, with a further improvement in fit also observed in the $[\bar{1}00]$ incidence geometry at a scattering angle of 120°. From these results one can infer therefore that the lateral radial shifts of the Cu surface atoms are accompanied by a perpendicular outward displacement of a similar magnitude. This outward relaxation which accompanies the lateral movement of the Cu atoms is consistent with a 'hard-sphere' atom model, in which the surface atoms 'ride up' on the underlying layer upon moving away from their hollow site bulk-like position. This simple model is, however, clearly inconsistent with the radial nature of the shifts, which forces the Cu surface atoms to lie closer than the hard-sphere separation to each other within the plane of the surface.

As a final exploration of the possible adsorbate-induced modification of the $Cu(100)(2 \times 2)$-CH_3S surface, the effect of changing the surface vibrations of the dosed surface is presented in the lower left panel in figures 4.3, 4.4 and 4.5. A possible consequence of strong chemisorption is a stiffening of the Cu surface atom bonds (these atoms no longer exist at the vacuum interface), and as such one might expect a reduction in the usual vibrational amplitude enhancement of these Cu atoms. In order to test the consequences of this possibility the simulations presented in the first panel, i.e. those without the perpendicular relaxation, were repeated with the usual $\sqrt{2}$ surface vibrational enhancement removed, so that the Cu surface atoms possessed the same vibrations as those in the underlying substrate. In all cases the adoption of bulk-like surface vibrations leads to a reduction in the simulated scattering yield, particularly so in the case of the unrelaxed model. This is understandable if one considers the fact that the shadow cone radius is only 0.17 Å at the Cu-Cu nearest neighbour distance behind the shadowing atom.

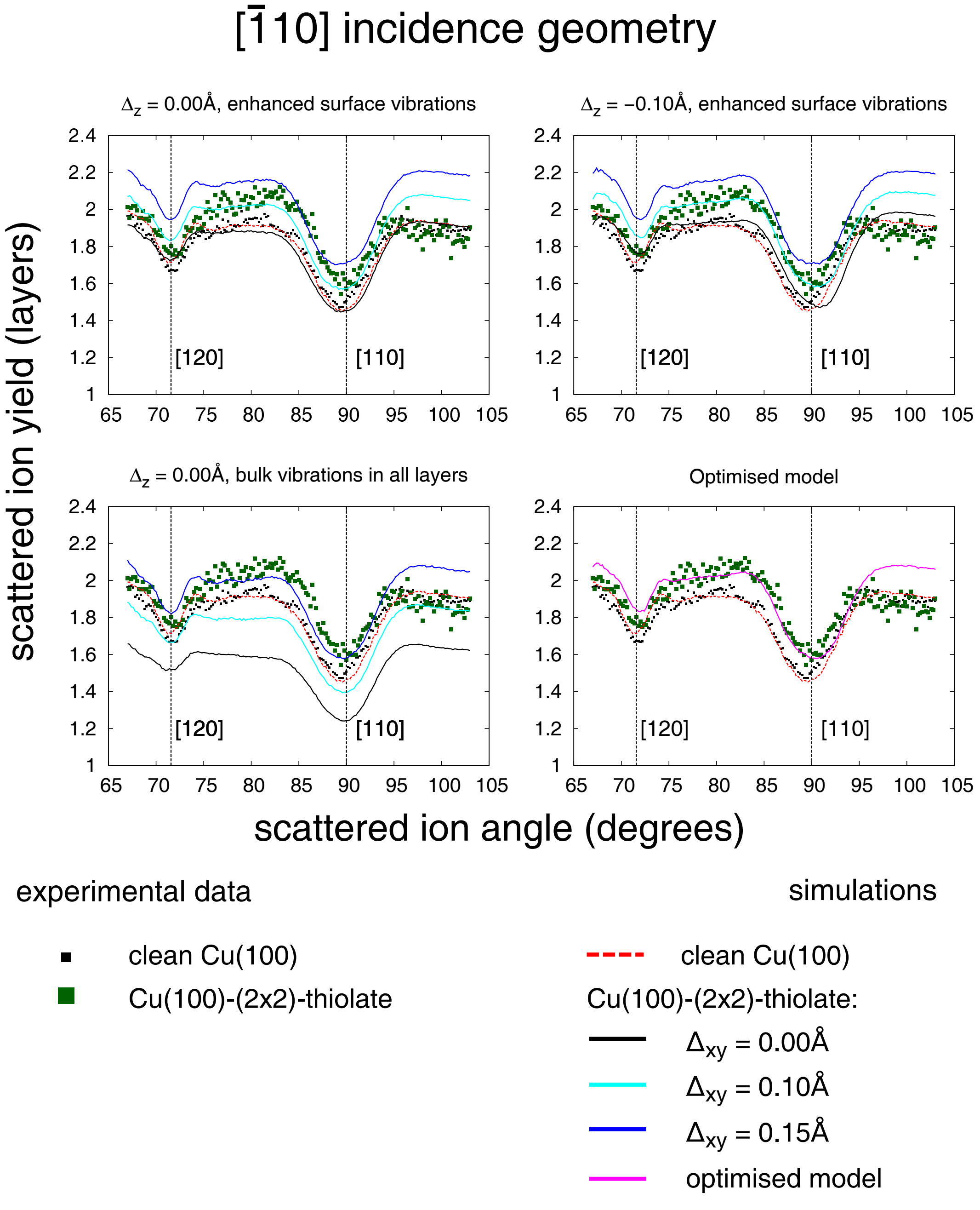

Figure 4.5: Comparison of the experimental blocking curves for both the clean Cu(100) and Cu(100)(2 × 2)-CH_3S surfaces in the $[\bar{1}10]$ incidence geometry, with the results of various simulated models exploring the effects of surface relaxation, including both radial lateral movement (Δ_{xy}) and perpendicular movement (Δ_z) of the surface Cu atoms.

Surface vibrations that are enhanced from 0.079 Å by a factor of $\sqrt{2}$ to 0.112 Å leads to a significant loss of shadowing in the case of the unrelaxed surface, and correspondingly a larger yield. When this surface vibrational enhancement is removed the 0.079 Å rms vibrational amplitudes are much smaller than the shadow cone radius, dramatically reducing the visibility of the Cu atoms directly behind those in the surface. However, if the surface Cu atoms are relaxed laterally by up to 0.15 Å, a value comparable with the shadow cone radius, the subsurface visibility is increased to a large extent, irrespective of the size of the surface vibrational amplitudes, and so the same reduction in the $\sqrt{2}$ enhancement has less effect on the scattering yield. In the light of the results shown in this final panel we deduce that if adsorbate-induced reductions in the surface vibrational amplitudes do occur, the implied lateral relaxation needed to reproduce the observed yield change is somewhat larger, but perhaps no more than 0.05 Å.

Having established the likelihood of both a small radial lateral relaxation and a similar perpendicular outward movement, and having shown that a small reduction in the usual surface vibration enhancement is quite reasonable, an optimisation of the Cu(100)(2×2)-CH_3S surface structure was undertaken using the automated IFFCO fitting routine. This optimisation was implemented in order to quantify the various structural parameters and so as to attach some confidence limits to the resulting best-fit structural values. The basic description of this routine and the methodology of its general use have been outlined previously (chapter 2). It is usual when using this routine to allow the λ scaling factors used in the calibration of the experimental yield to independently vary by up to $\pm 10\%$ in each scattering geometry, a number reflective of the confidence normally attached to these experimentally derived λ values, as discussed in the previous section. However, given the use of the clean surface simulations as a fine-tuning of these values, and the importance of the *relative* adsorbate-induced yield change to this argument, in the present case of this optimisation, λ was fixed. This ensured an optimised model with a yield change consistent with all models previously considered in this study. The optimum values found using this approach were $\Delta_{xy} = 0.12$ Å, $\Delta_z = -0.08$ Å and an rms surface vibrational amplitude of 0.103 Å, a value only slightly less than the standard $\sqrt{2}$ enhancement used throughout this investigation. These values are quite similar to those estimated in a more approximate manner using the original set of simulated models.

A formal method for estimating the precision on a parameter optimised in this way involves the calculation of a MEIS R-factor, used to quantify the 'goodness of fit' between experiment and theory in the optimisation routine, for various values of each parameter, moved away from the optimised value in a step-wise fashion with all other parameters remaining fixed at their optimised values. From a polynomial fit of the resulting 'R-factor plots' the error attached to each parameter can be estimated, in the manner described in chapter 2. These R-factor curves are shown in figure 4.6. Using this approach the error on the lateral shift parameter, Δ_{xy}, has a value of ±0.02 Å,with the error on the surface vibrational amplitude similarly found to be ±0.01 Å. With reference to figure 4.6 these best-fit values occupy a well defined minimum within their respective dimensions of the 'parameter space' considered. However, the Δ_{xy} dip possesses a clear asymmetry, implying an asymmetry in the confidence limits of this optimised parameter. Using an asymmetric fit based around the optimal minimum R-factor value merely results in the parameter confidence limit in the outward radial lateral direction being increased slightly, and that in the inward direction being similarly reduced, however the error values calculated using this approach do not differ, when quoted to one significant figure, from the initial error estimate of ±0.02 Å. The situation is more complicated in the case of the perpendicular shift Δ_z, with the minimum R-factor optimised value of $\Delta_z = -0.08$ Å accompanied by a second minimum at a value of -0.01 Å. The R-factor associated with this small outward shift is only slightly larger than that associated with the optimised value. Under the formal error approach this results in a value for Δ_z of 0.04 ± 0.08 Å. The more subjective assessment based on the simulated models in the previous figures, however, favoured a significant outward relaxation as its inclusion resulted in shifts in the simulated dips such as to better match those of the experiment. It is therefore clear that using the automated fitting approach, along with the fixing of the experiment/theory yield calibration, results in an insensitivity to these perpendicular movements. One downside of the R-factor plot based method of error calculation is that there is no allowance for the possibility of parameter coupling, e.g. a change in the value of Δ_z affecting the optimal value of Δ_{xy}. Given this shortcoming, and the ambiguity surrounding the optimised value for Δ_z, the R-factor curves were reproduced with Δ_z set to -0.01 Å, but under these circumstances the new R-factor curves showed little change, with the optimal value and precision estimate for Δ_{xy} remaining unchanged. This result implies very little parameter coupling between the Δ_z perpendicular surface displacements and the Δ_{xy} lateral radial surface movements, and increases the confidence in the verity of the 0.12 ± 0.02 Å value attached to Δ_{xy}.

Based on the results of both the initial analysis of the range of simulations in figures 4.3 to 4.5, and the IFFCO structural optimisation, it is clear that the MEIS data provide firm evidence for a lateral radial displacement of the surface Cu atoms around the S head-group atoms of the adsorbed methylthiolate species, estimated to be 0.12 ± 0.04 Å, and that this lateral movement is accompanied by an outward surface layer relaxation of 0.08 ± 0.04 Å. The precision estimate is a more conservative one in the case of the Δ_{xy} parameter than that provided by the R-factor plot method, but is more generous for Δ_z, acknowledging the clearly improved fitting of the blocking dips observed

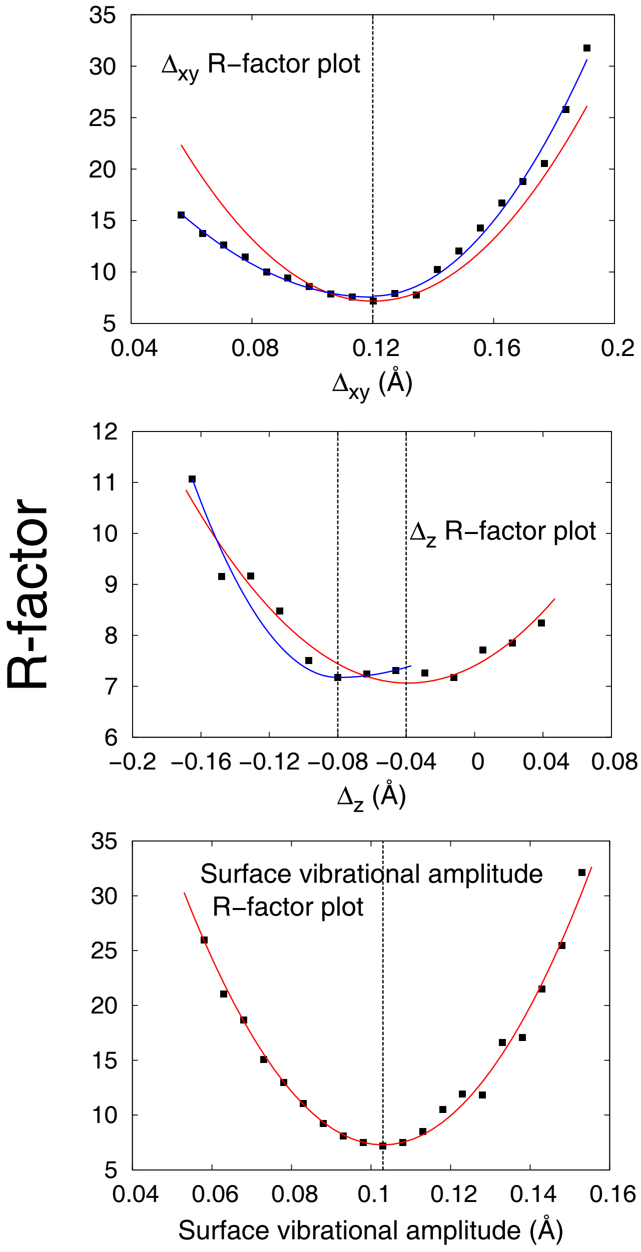

Figure 4.6: R-factor plots for the Δ_{xy} lateral shift, Δ_z perpendicular relaxation and surface vibrational amplitude set of parameters which were optimised using the IFFCO routine. The black squares represent the calculated R-factors as a function of different parameter values, and the red lines a 2nd order polynomial fit to these data, from which the error attached to each parameter can be estimated. The blue lines represent an asymmetric fit about the optimised parameter value.

upon the addition of a significant outward surface relaxation. The only theoretical study of the Cu(100)(2 × 2)-CH_3S surface [78] found values for these displacements which are only slightly smaller, namely a value in the range 0.04 − 0.09 Å for the lateral shift and a magnitude of between 0.05 − 0.08 Å for the outward relaxation of the surface Cu atoms. It is a point worth mentioning that in the case of MEIS the ion beam averages over an equal number of displacements of the opposite sign within the scattering plane, and as such it is impossible to distinguish between an outward lateral movement away from the S head-group or an inward one of the same magnitude. It is clear, however, that the changes seen upon adsorption are consistent with an outward radial displacement. Moreover, as the MEIS technique averages over the whole surface, including any disordered regions, an independent determination of this effect by a conventional diffraction technique which is sensitive to only the surface structures which exhibit long-range order would be ideal as a complimentary method to provide independent confirmation of the surface modification.

In order to place the results of this MEIS study in a slightly wider context, it is worth comparing the Cu(100)(2 × 2)-CH_3S surface with its accompanying lateral surface distortion with the structure adopted in the Cu(100)(2 × 2) phase formed by the adsorption of 0.25 ML of atomic sulphur. Whilst the Cu(100)S system includes the common low coverage (2 × 2) phase, at higher coverages no simple 0.5 ML c(2 × 2) phase forms, in contrast to the case of S adsorbed on Ni(100), for which both 0.25 ML (2 × 2) and 0.5 ML c(2 × 2) phases exist with the S atoms occupying the 4-fold coordinated hollow sites [77]. In this respect the Cu(100)(2 × 2)-S system is similar to the Cu(100)/methylthiolate case, with the lack of a simple c(2 × 2) phase perhaps indicative of S-induced surface compressive stress. This would suggest that a similar outward lateral radial movement around the hollow site S adatom might occur, and although an initial study using energy-scan photoelectron diffraction concluded in favour of *inward* radial movements of 0.05 Å [90], subsequent more detailed experiments based on quantitative LEED [91, 92], surface X-ray diffraction [93] and MEIS [94] challenged this, finding outward relaxations in the range 0.02 − 0.04 Å. The original energy-scan photoelectron diffraction data was eventually re-analysed, leading to a revised conclusion which favoured an outward movement of 0.04 Å. It seems clear then, that an outward lateral displacement occurs in the Cu(100)(2 × 2)-S system, mirroring our result on the Cu(100)(2 × 2)-CH_3S surface, but that this movement is very much smaller.

4.4 Conclusions

A medium energy ion scattering (MEIS) experiment using 100 keV H^+ ions has been carried out on the Cu(100)(2 × 2)-CH_3S surface, in order to explore any distortions of the Cu surface induced by the adsorbed methylthiolate species. The existence of the methylthiolate induced pseudo-(100) reconstruction on the Cu(111) surface, with a Cu-Cu spacing 15% larger than that of Cu(100), has led to the prediction of considerable adsorbate-induced stress in the 0.25 ML methythiolate (2×2) phase. It is suggested that this stress may result in a local strain characterised by radial lateral expansions of the Cu atoms surrounding the 4-fold hollow site occupied by the thiolate. MEIS blocking curves were obtained for both the clean and thiolate dosed (2×2) phase in three distinct incidence geometries along the $[\bar{1}10]$,$[\bar{1}10]$ and $[\bar{1}10]$ crystallographic directions respectively. Changes in the scattered ion yield in these three geometries have been shown to be consistent with a lateral radial Cu atom expansion of 0.12 ± 0.04 Å, whilst the angular positions of the blocking dips indicate that an additional perpendicular outward surface movement of 0.08 ± 0.04 Å occurs.

Chapter 5

Methylthiolate induced modification of the Au(111) surface

5.1 Introduction

Self-assembled monolayers (SAMs) of alkylthiolate ($CH_3(CH_2)_{n-1}S$) molecular chains adsorbed on the Au(111) surface have long been a subject of great scientific interest, primarily due to the use of such SAM systems in range of technological applications, (e.g. [68–70]), but also due to the ease with which the Au(111)/SAM surface can be prepared, both under ultra-high vacuum (UHV) conditions and in the liquid phase. However, despite the extensive range of studies conducted on these systems [63–67], the structure of the thiolate/Au interface remains in doubt [71]. It is well established that the thiolates bond to the surface through the S head-group, and that two different structural phases exist at the saturation coverage of 0.33 ML, having periodicities of $(\sqrt{3} \times \sqrt{3})R30^\circ$ and $(3 \times 2\sqrt{3})$rect., with the latter phase being often referred to in the literature as a $c(4 \times 2)$ superlattice of the $(\sqrt{3} \times \sqrt{3})R30^\circ$ surface mesh. It would seem that the shortest alkyl chains, in particular methylthiolate ($n = 1$), will only adopt surface structures with the $(\sqrt{3} \times \sqrt{3})R30^\circ$ periodicity, whereas for longer alkyl chains the two phases appear to coexist.

The majority of the earliest structural studies of the Au(111)/alkylthiolate systems have been based on theoretical total-energy calculations, with a particular focus on the methylthiolate species, due to the small size of the molecule and the associated reduction in the difficulty of the calculations. These studies, which assumed the thiolate covered surface to be unreconstructed, consistently found in favour of a thiolate S head-group adsorption in either the 3-fold coordinated hollow sites [95–98], the 2-fold coordinated bridge sites [99–101], or a site approximately halfway between the two [102, 103]. These studies were subsequently challenged by two independent experimental determinations of the Au(111)($\sqrt{3} \times \sqrt{3}$)R30°-CH_3S structure, using energy-scanned photoelectron diffraction (PhD) [104] and normal incidence X-ray standing waves (NIXSW) [105], both of which indicated that the the S head-group adsorbed in an atop site. This apparent inconsistency can be reconciled if the adsorbed thiolate induces a surface reconstruction on Au(111), but the exact nature of the surface structure formed remains controversial. Two rather different models for the reconstructed Au(111)/thiolate surface have been proposed, namely the Au-adatom-dithiolate model (AAD), and the Au-adatom-monothiolate model (AAM), shown in figure 5.4 in section 5.3.2 on page 75. In the AAD model, proposed on the basis of scanning-tunnelling microscopy (STM) results [106], two thiolate species bond atop Au(111) surface atoms, on either side of an Au adatom which occupies a bridge site. Based on further NIXSW experiments of the high coverage phases of a range of alkythiolates of varying chain lengths (n = 1 to n = 8), the AAM model was proposed [107]. This involves a single thiolate bonded atop an Au adatom which itself occupies a 3-fold coordinated hollow site. In the case of the ($\sqrt{3} \times \sqrt{3}$)R30° phase these adatoms are situated in 'fcc' hollow sites (hollows directly above Au atoms in the third atomic layer of the substrate), whereas in the ($3 \times 2\sqrt{3}$)rect. phase the adatoms reside in both the fcc hollows and the 'hcp' hollows (directly above Au atoms in the second layer).

Although there are a few theoretical studies which support the AAM model (e.g. [108]), most more recent studies favour the AAD model due to the higher energy cost associated with creating an AAM structure, as this involves the creation of twice as many Au adatoms as the AAD structure (e.g. [109]). More recent experimental investigations using photoelectron diffraction [110, 111] and near-edge X-ray absorption fine structure (NEXAFS) [110, 112] fail to distinguish between the two models, as both involve S adsorption in a local atop site geometry. Another recent study, based on Au 4f photoemission core level shifts [113, 114] appears to favour the AAM model, but a new theoretical investigation [115] suggests that the photoemission results may be better described by the AAD model. New STM results provide conflicting evidence for the both the AAD [116] and the AAM [117] models.

A key difference between these two models regarding the thiolate saturation coverage ($\sqrt{3} \times \sqrt{3}$)R30° phase is that of the local adsorption site and coverage of the Au adatoms. In the AAD model we expect to see a 1/6 ML (0.17 ML) coverage of Au adatoms in bridge sites, whereas in the AAM model there are 1/3 ML (0.33 ML) of Au adatoms, all of which occupy hollow sites. In two recent STM studies the authors

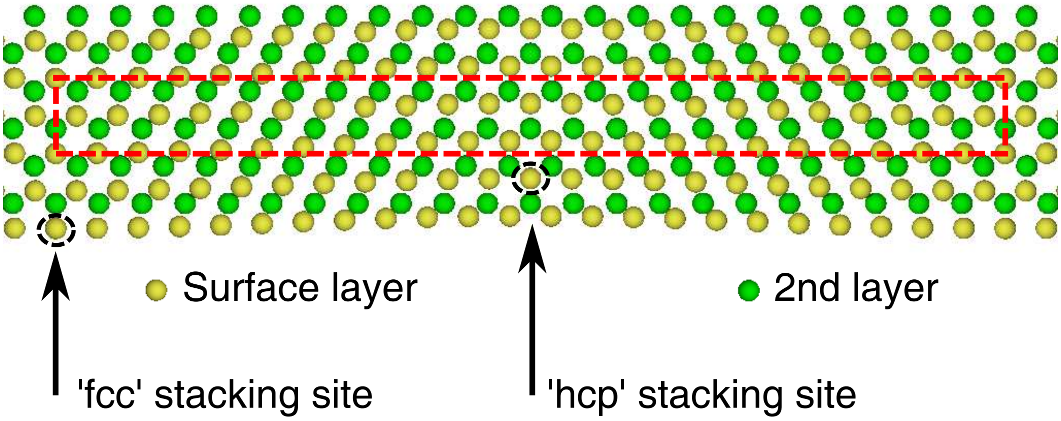

Figure 5.1: Plan view of the surface and 2nd atomic layers of the $(22 \times \sqrt{3})$rect. surface reconstruction of the clean Au(111) surface, showing the smooth transition between 'fcc' and 'hcp' stacking along the long axis of the surface mesh.

tried to determine this Au adatom coverage by reacting off the surface thiolate and then measuring the area of the resulting Au monolayer island coverage, formed by the two-dimensional condensation of the adatoms. In one of the two experiments [118], the octylthiolate SAM was removed by interaction with an atomic hydrogen flux, with a coverage of 0.14 ML found for the resulting Au adatom islands, a value which supports the AAD model. In the second study, also involving octylthiolate [119], the molecules were removed by localised electrolysis with water under the STM tip, with a value for the resulting Au adatom island coverage found to be 0.15 ML. However, this coverage estimate was subsequently revised to 0.22 ML, a value considerably higher than that expected for an AAD surface structure. This revision was the result of a number of corrections not considered in the first study. One of these corrections stems from the fact that upon removal of the thiolate species and the subsequent Au adatom island formation, the clean Au(111) surface adopts the well characterised [120–122] $(22 \times \sqrt{3})$rect. 'herring-bone' structure. In this reconstruction of (1×1) surface, the long-axis periodicity results from the addition of an extra Au atom in every 22 within the surface layer. This extra Au atom occupies an hcp site (stacking above Au atoms in the second layer), forcing the remaining surface atoms to occupy a range of sites between the hcp site occupied by the additional atom and the normal 'fcc', leading to a smooth transition between hcp and fcc stacking (see figure 5.1). It is the resulting increase of 0.045 ML in the clean surface Au coverage which necessitates a revision to the initial estimate of the Au adatom coverage for the dosed surface. In addition, another correction must be applied, in this case due to the existence of monolayer 'etch pits', characteristic of such thiolated surfaces, which become partially filled upon the removal of the octylthiolate species. The consideration of these two surface processes, coupled with the possibility of the loss of Au adatoms to the steps on the underlying Au(111) surface, has lead the authors to conclude that the 0.22 ML value should be regarded as a lower limit estimate of the Au adatom coverage on the Au(111)($\sqrt{3} \times \sqrt{3}$)R30°-CH_3S surface. Therefore the authors of this study, Li et al., concluded in favour of the AAM model [119].

Given the problems associated with the movement of Au adatoms upon the removal of the thiolate species, an ideal solution would involve the use of surface technique which could probe the adatom coverage at the *buried interface*, with the thiolate species in place. Medium energy ion scattering (MEIS) is one such technique, which has proven effective in evaluating similar thiolate-induced modification of the surface for both Cu(111) [74] and Ag(111) [123]. In the remainder of this chapter the results of just such an investigation are presented, namely the use of MEIS to probe the buried interface in the Au(111)($\sqrt{3} \times \sqrt{3}$)R30°-CH_3S system.

5.2 Experimental details

The experiments were performed at the Daresbury Laboratory national MEIS facility, over a period spanning a number of experimental data collection runs. The single crystal Au(111) sample was purchased from the Surface Preparation Laboratory (SPL, Netherlands), where it was both oriented and polished. The crystal was cleaned under ultra-high vacuum (UHV) *in situ*, with the normal cycles of 1.5 keV Ar^+ ion sputtering at grazing incidence followed by annealing to $\sim$ 550°C. The surface was judged to be contaminant free and well-ordered by the use Auger electron spectroscopy (AES) and low-energy electron diffraction (LEED), respectively, with the clean surface LEED pattern showing the 'split-spots' characteristic of the clean herringbone-reconstructed ($22 \times \sqrt{3}$)rect. phase. The methylthiolate ($\sqrt{3} \times \sqrt{3}$)R30° phase was formed by exposing the clean Au(111) surface, at room temperature, to a vapour of dimethyldisulphide (DMDS - CH_3S-SCH_3). This molecule breaks up in the presence of the surface via the scission of the S-S bond to form two methylthiolate species, which then bond to the surface through the S headgroup. DMDS is used in preference to methylthiol due to its lower toxicity and greater ease of handling. The DMDS vapour was introduced to the sample through a leak valve connected to a glass ampoule containing the DMDS in liquid form, with the external section containing the ampoule having been previously purified by several freeze/thaw pumping cycles. Typical exposures of DMDS vapour lasted 10-30 minutes at a partial pressure of 1×10^{-8}–5×10^{-7} mbar. No use of LEED was made to characterise the ($\sqrt{3} \times \sqrt{3}$)R30° thiolate phase before the MEIS data were taken because of the known high cross-section for electron irradiation damage. Despite this, LEED was used both during the initial dosing procedures and after some of the MEIS studies, and in both cases a pattern consistent with the $(\sqrt{3} \times \sqrt{3})$R30° phase was observed.

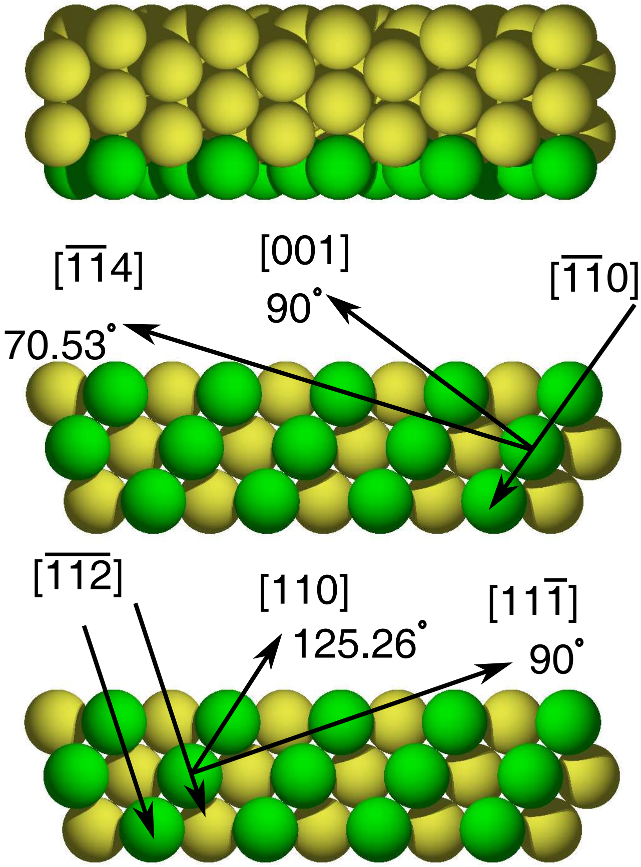

Figure 5.2: Plan and side-section views of the ideal bulk-terminated Au(111) surface. Shaded in green is one of the sheets of atoms that lie in a scattering plane used in this experiment. The figure shows the $[\bar{1}\bar{1}0]$ and $[\bar{1}\bar{1}\bar{2}]$ ion incidence directions used in this experiment, which correspond to nominal illuminations of only the 1st and both the 1st and 2nd outermost atomic layers respectively. Also shown are the ion exit directions along which major blocking occurs.

The Au(111) crystal was transferred under UHV to the main scattering chamber, in both the clean and thiolate dosed condition, where MEIS data were collected using 100 keV H^+ ions. Caution was exercised when considering the total ion flux incident on any particular region of the sample, so as to avoid ion beam induced surface damage affecting the MEIS data. Test spectra were collected using total incident ion fluxes on a single sample area of 2.5 μC, 5.0 μC and 10 μC, however in all of these cases no evidence of beam induced damage effects was observed. Therefore, the MEIS data presented in this chapter were taken with total incident fluxes between 0.5-4.0 μC for any particular region of the sample illuminated by the ion beam.

MEIS blocking curves from both the clean and dosed Au(111) surface were collected in two distinct ion incidence geometries, as shown in figure 5.2. This figure makes clear that ions incident in the $[\overline{1}\overline{1}0]$ and $[\overline{1}\overline{1}2]$ direction will nominally illuminate only the first one and two atomic layers, respectively, in the case of the ideal bulk-terminated surface. Of course, the (room temperature) thermal vibrations of the atoms ensure that some fraction of the otherwise shadowed deeper atomic layers become visible. However, it is worth noting that for a shadowed subsurface atom which sits at the nearest neighbour distance of 2.88 Å behind the shadowing Au atom, the resulting shadow cone has a radius of 0.25 Å. This value can be compared to the considerably smaller root-mean-square (rms) vibrational amplitude of a bulk Au atom, calculated from the bulk Debye temperature to be 0.093 Å. Thus the large scattering cross-section for the Au atoms (with the associated large shadow cone widths) has the effect of limiting the partial illumination of nominally shadowed subsurface layers. Nonetheless, VEGAS simulations of the unreconstructed Au(111) surface do show additional signal attributable to scattering from the deeper subsurface layers, although much of this extra signal can be attributed to the inclusion of a $\sqrt{2}$ enhancement of the surface layer rms vibrational amplitudes in the simulations. This value is representative of the typical enhancements found to be present on single crystal metal surfaces.

In order to express the experimental scattered ion flux in terms of the number of visible atomic layers, as is the case with the simulated ion yield of the VEGAS code, it is necessary to obtain an experiment dependent scaling factor λ. A value for this term was found in the normal manner; namely by use of a Si(100) reference sample shallowly implanted with Cu atoms to a known concentration. A more detailed description of this way in which a value for λ is extracted can be found in chapter 3. It is important to note that a λ scaling factor derived in this manner is typically reliable to within $\pm 10\%$, and that in some cases, including the present study, a more accurate calibration is required in order to interpret the data. A discussion regarding a refinement of the λ scaling factor forms part of the next section of this chapter.

5.3 Results and discussion

5.3.1 Initial evaluation and yield calibration

The experimental blocking curves obtained for both the clean Au(111) surface and the 0.33 ML methylthiolate $(\sqrt{3} \times \sqrt{3})$R30° phase are shown in figure 5.3 as individual data-

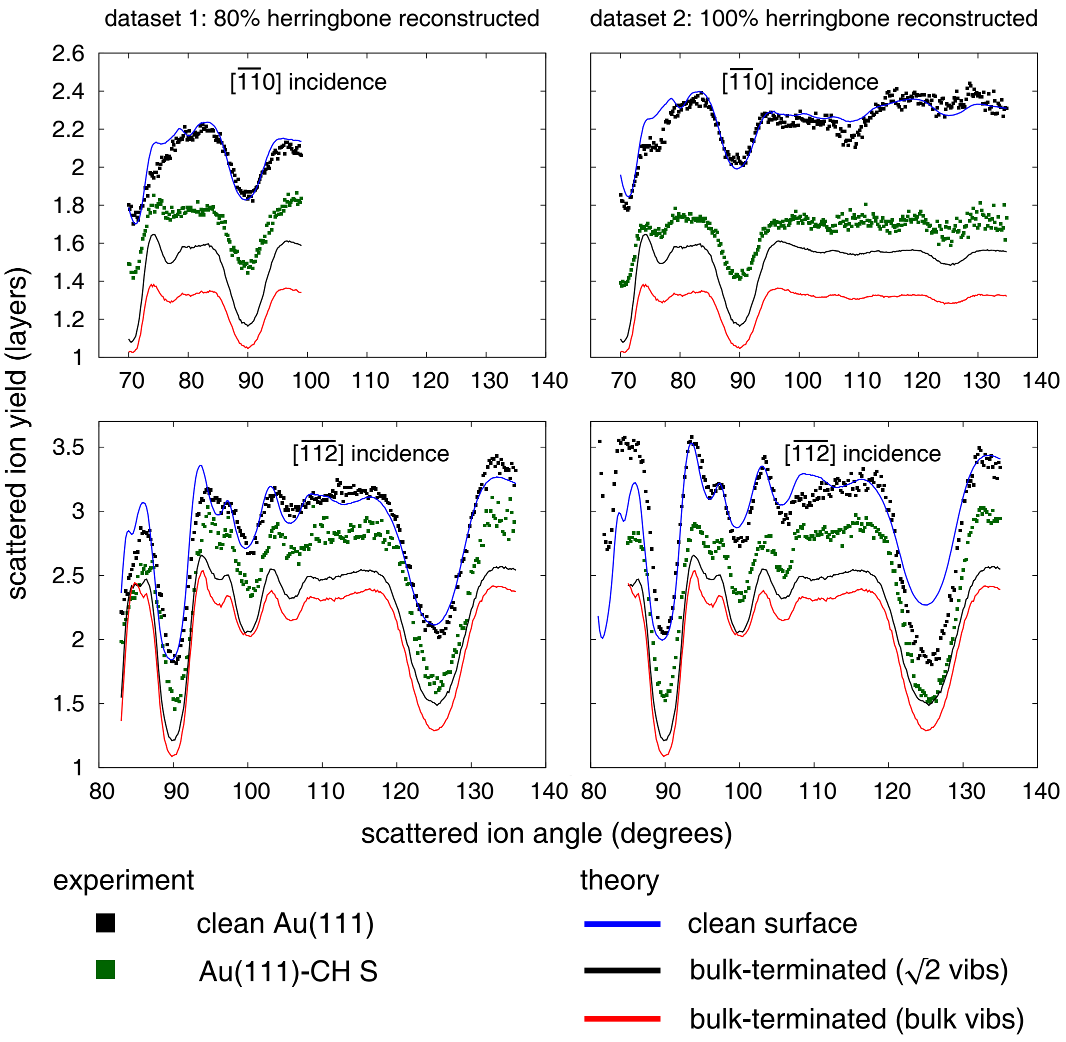

Figure 5.3: Experimental MEIS blocking curves from both the clean and $(\sqrt{3} \times \sqrt{3})\mathrm{R}30^\circ$ thiolated Au(111) surfaces recorded with ions incident in the $[\overline{1}10]$ and $[\overline{11}2]$ directions (see figure 5.2). Also shown are the VEGAS simulated blocking curves for the clean Au(111) surface, which include the $(22 \times \sqrt{3})$rect. herringbone reconstruction, with the simulated results from the bulk-terminated (1×1) Au(111) surface added as a useful reference.

points. This figure includes the results of two independent MEIS experiments which were separated by around two years, the first of which covered a smaller range of scattering angles in the $[\overline{1}\overline{1}0]$ incidence direction. These blocking curves show a broad similarity in the shape and position of the major blocking dips for both the clean and thiolate-covered surfaces, indicative of the fact that these dips are primarily a consequence of the blocking of ions exiting the crystal from the unreconstructed near-surface region along the bulk crystallographic directions. The main difference between the scattered ion signal from the clean and thiolated surfaces is in the absolute yields, a qualitative effect observed for thiolate adsorption on both Cu(111) and Ag(111) [74, 123]. However, in both of these previous cases the clean surface was unreconstructed, with the addition of the thiolates leading to a surface reconstruction and consequentially an *increase* in the yield of the scattered ion signal. However, on clean Au(111) there exists the aforementioned $(22 \times \sqrt{3})$rect. herringbone reconstruction. The smooth transition along the long axis of this phase from fcc to hcp stacking means that the vast majority of the atoms in the reconstructed surface layer no longer occupy bulk sites, and as such will not shadow the subsurface layers. This leads to an expected increase in yield corresponding to roughly one atomic layer. This is due to the fact that although there is slightly more than one monolayer of Au atoms in the reconstructed surface, as mentioned in the introduction, one can also expect a small amount of shadowing of the second layer. Given that even small concentrations of adsorbed thiolates are known to lift this herringbone reconstruction, and that the expected coverage of Au adatoms in both the AAM and AAD model for the thiolated surface is well less than one atomic layer, one can easily account for the resulting *decrease* in the scattered ion signal upon the adsorption of the thiolate species. The experimental blocking curves of the two different datasets are generally in very good agreement, aside from the absolute scattering yields obtained from the clean Au(111) surface. This discrepancy will subsequently be considered in detail.

Although the qualitative yield difference between the clean and thiolate dosed Au(111) surfaces can be easily understood, further insights require that the absolute yield of the experimental scattering signal be accurately calibrated. The standard method for obtaining the λ scaling factor, which, as discussed previously, involves typical errors of $\pm 10\%$ is thus unsuitable. This value is derived from a separate reference sample, but a considerably more accurate calibration value can often be obtained by reference to the scattered yield obtained from the clean surface upon which the thiolates have been deposited. This is the case for both Cu(111) and Ag(111), which possess unreconstructed clean surfaces with very little movement of the surface atoms away from the bulk-like positions. The well-established nature of both the structural and vibrational parameters associated with these surfaces enables the scattering yield (expressed in visible atomic layers) to be accurately predicted by simulation, and thus the absolute scattered ion yields in both experimental blocking curves can be stated with confidence. The existence of the herringbone reconstruction on the Au(111) surface makes such an approach difficult in the case of the current study. The structure $(22 \times \sqrt{3})$rect. phase is quite well known, although the exact coordinates of some of the Au atoms in the reconstructed layer are not known precisely. On the other hand, we show later that knowledge of these exact positions does not prove important in determining the scattered ion yield from the clean Au(111) surface. Of greater concern is the possible existence of regions of unreconstructed (1×1) phase on the clean surface associated primarily with the presence of local defects, as observed in STM studies. A considerable fraction of this (1×1) phase on the surface leads to a significant reduction in the scattered ion yield, therefore the percentage of the surface which is unreconstructed becomes the key variable in the determination of the scattered ion yield from the clean surface. So that the impact of this uncertainty might be minimised, many MEIS experiments on the Au(111)$(\sqrt{3} \times \sqrt{3})$R30°-$CH_3S$ surface were conducted over a period of three years, with each experiment including repeated measurement on both the clean and re-prepared thiolated surfaces. The datatsets shown in figure 5.3 are representative of the numerous blocking curves obtained in this manner.

In order to obtain an accurate and internally-consistent yield calibration VEGAS simulations of the $(22 \times \sqrt{3})$rect. herringbone reconstructed Au(111) surface were performed, along with simulations for the unreconstructed (1×1) phase. Although there is some uncertainty surrounding the exact positions of the surface atoms in the herringbone phase, it was found that the predicted scattering yield was insensitive to the particular atomic coordinates used. This is because the majority of these atoms are significantly removed from the bulk sites in which they would shadow the subsurface layers, and so the total scattered ion flux is insensitive to their exact locations. The results of these simulations were compared to the experimental data from clean Au(111), with a number of possible admixtures of the reconstructed and unreconstructed simulations to account for incomplete reconstruction on the clean surface. In figure 5.3 the resulting best-fit (as judged by visual inspection) clean surface simulations are shown, with 80% and 100% herringbone reconstructions found to be optimal for the first and second datasets respectively. As expected, the scattering yield from the 100% herringbone reconstructed surface is higher than that from the 80% reconstructed surface, but also noteworthy are the yields of the thiolated surfaces in the two datasets, which are almost identical. This is reassuring, as one would not expect the Au atom movement at the thiolate/gold interface (if any) to be dependent on the exact long-range order of the surface, order which nevertheless does affect the fraction of the clean surface which does not reconstruct.

Figure 5.3 also shows the results of the VEGAS simulations of the unreconstructed

(1×1) Au(111) surface. There are in fact two simulations; one in which the surface layer atoms are assumed to have the same vibrational amplitudes as those in the underlying bulk layers, and one in which the surface vibrations are enhanced by a factor of $\sqrt{2}$. This standard enhancement is often found to better describe the MEIS data from the unreconstructed clean surface for a number of other surfaces (such as Cu). The simulations for the (1×1) surface which do not posses this enhancement are included as a useful reference to the results of the herringbone reconstruction, as these blocking curves show the scattering which would be expected from the unreconstructed (and bulk vibrating) lower layers upon the removal of the herringbone reconstructed surface layer.

It is clear that the experimental scattered ion yield from the thiolated Au surface is significantly larger than that expected from the unreconstructed (1×1) phase of Au(111), even when including enhancement of the surface Au atom vibrations. There is ~ 0.2 additional (with respect to the (1×1) surface with enhanced vibrations) atomic layers worth of scattering yield in the $[\overline{1}\overline{1}0]$ incidence geometry, and ~ 0.3 atomic layers of extra signal in the $[\overline{1}\overline{1}2]$ geometry. These yield differences must arise from the scattering from additional Au atoms, i.e. the Au adatoms characteristic of the AAM and AAD models, providing direct evidence for existence of Au adatoms at the Au/thiolate interface. Therefore, the remaining questions are:

1. How many Au adatoms are present at the interface?
2. Where are these adatoms located?

5.3.2 Modelling the Au(111)$(\sqrt{3} \times \sqrt{3})$R30°-$CH_3S$ system

As discussed in the introduction of this chapter, there are two basic alternative models for the $(\sqrt{3} \times \sqrt{3})$R30°-methylthiolate surface structure. The first is the AAM model for which we expect 0.33 ML of Au adatoms sited in the 3-fold coordinated fcc hollows, although a small fraction of these adatoms may occupy hcp hollow sites. This last point is an important one, as MEIS is sensitive to the differences between these two hollow sites, as will be explained in detail shortly. The second model considered is the AAD model, in which each AAD species consists of one Au adatom, which occupies a bridging site, and two thiolate molecules bonded either side of the Au adatom in near-exact atop sites. This model cannot actually form a true $(\sqrt{3} \times \sqrt{3})$R30° phase on the surface unless one doubles the thiolate coverage to 0.67 ML as each AAD has two thiolate molecules associated with it. As this is clearly at odds with the known thiolate coverage of 0.33 ML, we instead accept that, as suggested in recent low-temperature STM studies [116], this high coverage phase actually consists of 0.17 ML of of AAD species with the Au adatoms lacking good long-range order. Thus the AAD structure can be modelled with 0.17 ML

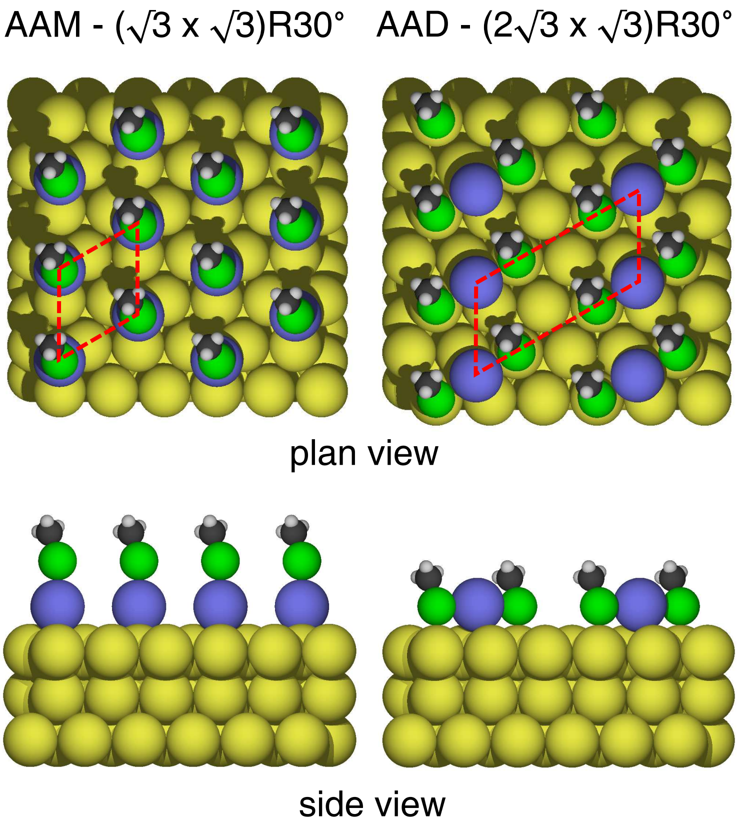

Figure 5.4: Plan and side views of the models used in this study to represent the AAM (Au-adatom-monothiolate) and AAD (Au-adatom-dithiolate) reconstructions suggested to occur in the Au(111)($\sqrt{3} \times \sqrt{3}$)R30°-CH_3S surface phase. For the sake of clarity the Au adatoms are shaded in blue, and the Sulphur head-group atoms in green. The S-C bond angles shown in these models are schematic only; the actual orientations are not well-established.

of Au adatoms in bridging sites, each with the two associated thiolate molecules, on a ($2\sqrt{3} \times \sqrt{3}$)R30° surface mesh. The two basic models for the AAM and AAD structures are shown in figure 5.4, where the orientations of the S-C bonds are in schematic form; neither the azimuthal or polar angles which describe these bond orientations are well established.

All of the possible Au adatom sites, namely the fcc and hcp hollow sites and 2-fold coordinated bridging sites, are in principle distinguishable in this MEIS experiment. The differences between these sites as seen by the incident ions are explained as follows, with figure 5.5 showing a model in which these differences are highlighted. AAM adatoms which occupy the fcc hollows are situated in bulk-continuation sites, therefore in theory they should not increase the scattered ion yield, as the Au adatoms shadow the otherwise fully illuminated subsurface atoms below. In effect the incident ions see the same 'chains' of atoms as they would have seen, had the surface been unreconstructed. If, however, the inter-layer spacing of the adatoms differs from the bulk inter-layer spacing, or there is an enhancement in the amplitude of the vibrations, there should be an associated increase in the scattering signal. For the AAM adatoms which may occupy hcp hollow sites the situation is somewhat different, as shown in figure 5.5, where it is clear that for both of the incidence geometries, but for the $[\overline{1}\overline{1}0]$ incidence direction in particular, these adatoms do not fully shadow any atoms in the lower atomic layers, thus the existence of adatoms in these sites should induce an increase in the overall scattering signal. In addition, Au adatoms in the hcp hollows also block the outgoing ions in directions not originally associated with strong blocking effects, leading to the expected presence of additional blocking dips. In the case of the bridge sites occupied by the Au adatoms of the AAD model, it is important to note that there are three different bridge sites, all of which are occupied (both due to the presence of multiple rotational domains, and the possibility of surface disorder), these sites being labelled **a**, **b** and **c** in figure 5.5. In this figure it is clear that adatoms which are located in the **b** and **c** bridge sites do not lie within any substrate scattering planes, therefore these atoms will neither shadow the Au substrate atoms nor block the backscattered ions from these same atoms, but they will be expected to increase the overall scattered ion yield. By contrast, Au adatoms in the **a** bridging sites do lie within the scattering plane, although in a non-bulk-like position. Thus they will not be expected to strongly shadow any substrate atoms, and as such they will contribute to the total scattered ion yield in a similar manner to those adatoms which lie in sites **b** and **c**. However, these site **a** bridging atoms will block the scattered ions in the appropriate outgoing trajectories.

The results of the VEGAS calculations for the AAM and AAD models are shown in figure 5.6. In these models the Au adatoms reside on an unreconstructed Au(111) surface, with a $\sqrt{2}$ enhancement of the vibrational amplitudes in the surface layer. The methylthiolate species are represented by the inclusion of the S head-group, with the C and H atoms not considered, in part due to the ambiguity surrounding their exact positions, but most significantly because these atoms are such weak scatterers in comparison to the Au atoms (as the scattering cross-section scales with the square of the atomic number, scattering from the C atom is ~ 7 times weaker than that from the S atom, and two orders of magnitude weaker than that from Au). It is also the case that the C and H atoms do not occupy sites in which they would be expected to contribute significant shadowing or blocking.

The VEGAS simulations are compared with the experimental data from the second dataset (the dataset with the increased scattering angle range in the $[\overline{1}\overline{1}0]$ incidence

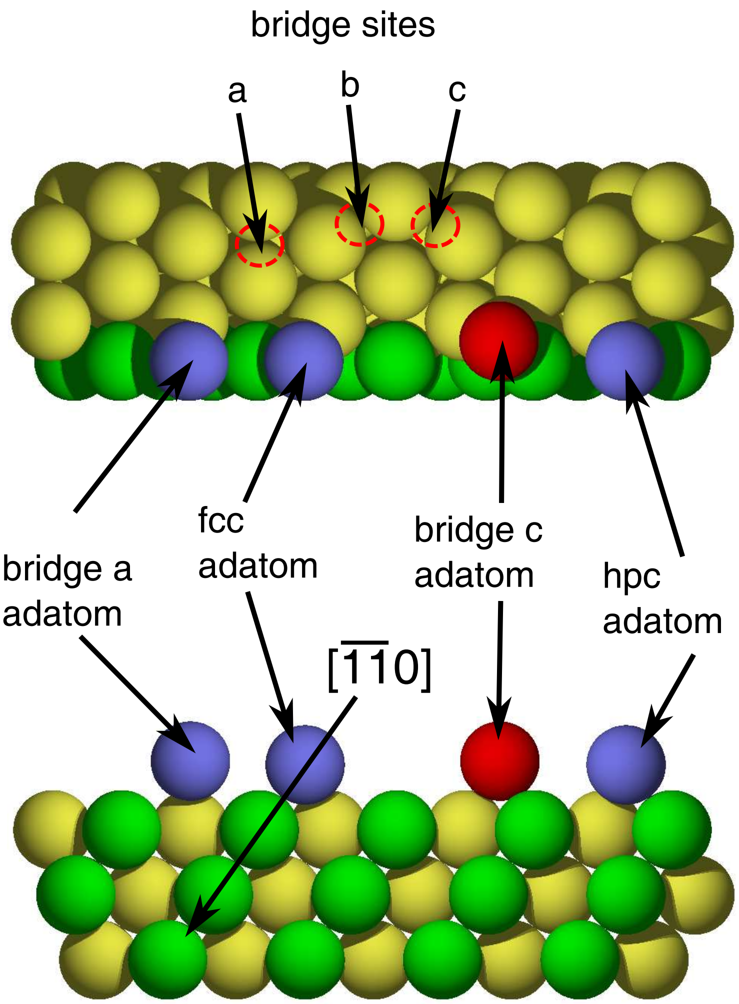

Figure 5.5: A plan and side view of the Au(111) surface exploring the adsites considered in this study. Au adatoms situated in the fcc hollow sites, hcp hollow sites and bridge sites are shown. The positions of the three inequivalent bridge sites are indicated, the **a** site being the only one that lies within the scattering planes of the substrate atoms (with adatoms in the scattering plane shaded in blue).

geometry), along with the simulations for the 100% herringbone reconstructed clean surface. In the panels on the left of figure 5.6 are shown the results of the AAM model simulations. In the AAM calculations, the S head-group atoms were positioned atop the 0.33 ML of Au adatoms which occupied either the fcc hollows or the hcp hollows, leading to the two different simulated blocking curves shown in these panels. Although it is only the fcc hollows which have been proposed to be occupied in the $(\sqrt{3} \times \sqrt{3})$R30° saturation coverage phase, the simulation for the fully hcp occupied AAM model provides

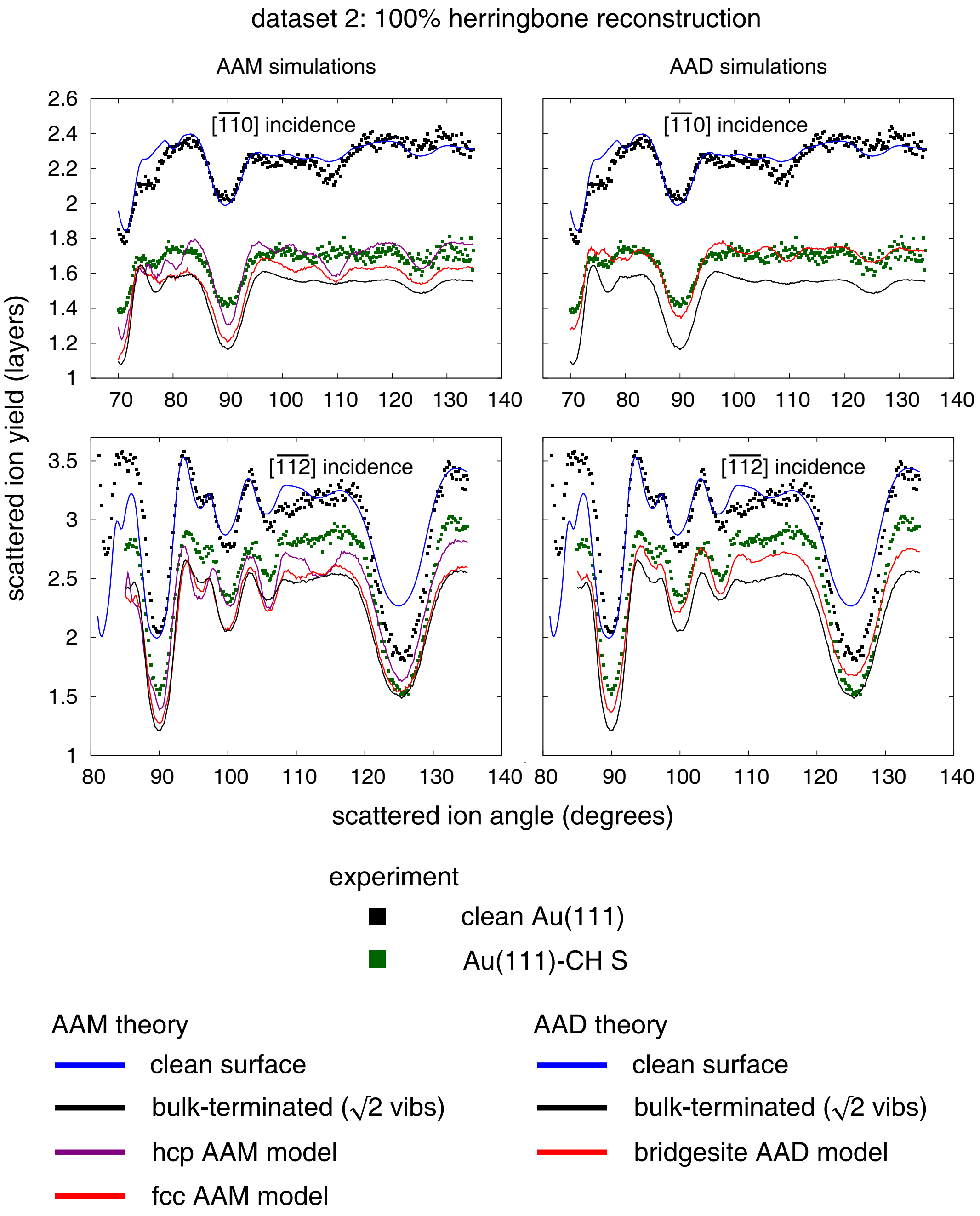

Figure 5.6: Experimental blocking curves for the clean and methylthiolate covered Au(111) surfaces, together with the results of VEGAS simulations of the (1×1) unreconstructed surface, the herringbone reconstructed clean surface and a number of simulations of the Au(111)$(\sqrt{3} \times \sqrt{3})$R30°-$CH_3S$ surface based on the AAM and AAD models shown in figure 5.4.

a clear indication of the effects expected for the partial occupation of this site. In these models the Au adatoms were situated centrally within the hollow sites at a bulk interlayer spacing above the surface, with adatom vibrational amplitudes enhanced to the same extent as those in the surface layer. As predicted in the earlier discussion, the occupation of only fcc hollows leads to only a small rise in the scattered ion signal, with this rise of < 0.1 atomic layers largely the result of the enhanced vibrations of both the adatoms and those atoms in the surface layer (in the unreconstructed surface only the first atom encountered by the ions possesses an enhanced vibrational amplitude). By contrast, the hcp AAM simulated blocking curves show a greater increase in the scattering yield of ~ 0.2 layers. Although this increased yield difference is expected, as mentioned previously (these adatoms do not strongly shadow any atoms below, in contrast to adatoms in fcc bulk-continuation sites), the yield change upon the inclusion of hcp adatoms might have been expected to be closer to ~ 0.33 layers, in line with the adatom coverage of 0.33 ML. A number of further simulations have shown that the yield increase due to the presence of these adatoms is greatly suppressed by a shadowing of the Au(111) surface by the S head-group atoms. It is clear that the overall yield predicted by the fcc AAM model simulations is significantly lower than the experimental yield from the thiolated surface; this is especially true in the $[\overline{1}\overline{1}2]$ incidence geometry. The hcp AAM model simulated blocking curves certainly better describe the average yield increase of thiolate dosed scattering signal, particularly in the $[\overline{1}\overline{1}0]$ incidence geometry, but the simulated blocking features do not provide a good match to experiment. Specifically the large simulated blocking dips situated at $\sim 110°$ and $\sim 113°$ in the $[\overline{1}\overline{1}0]$ and $[\overline{1}\overline{1}2]$ incidence directions respectively are not present in the experimental blocking curves. In addition, hcp AAM simulations show a particularly deep blocking dip with high shoulders in the [001] major blocking direction (scattering at 90°), whereas the same feature in the experiment is considerably shallower. Some partial occupation of hcp hollow sites in the AAM model would therefore improve the experiment/theory agreement. However, as stated previously NISXW experiments [105, 107] are consistent with 100% fcc site occupation and could only support a small partial occupation of hcp sites ($< 10\%$). The simulations from such an AAM model would therefore still poorly describe the overall scattered ion yield of the experimental data.

The panels on the right of figure 5.6 display the results of VEGAS simulations of the basic AAD structure shown in figure 5.4. These simulations take into account the possibility of rotational domains/disorder, such that the simulated blocking curves include in equal measure the scattering from Au adatoms which occupy the three different bridge sites shown in figure 5.5. The height of the bridge site Au adatoms above the surface plane is consistent with the simple hard-sphere model of touching Au atoms.

The AAD simulated blocking curve in the $[\bar{1}\bar{1}0]$ incidence geometry clearly describes the experiment rather well in terms of the overall absolute scattering yield, and although there are still some discrepancies between the theory and experiment blocking features, these are quite small. There is, however, still a fairly substantial yield discrepancy between the simulations and experiment in the $[\bar{1}\bar{1}2]$ geometry. The ~ 0.2 atomic layer yield increase evident in the AAD simulations is slightly larger than that implied by an additional 0.17 ML worth of Au atoms, but a detailed inspection of the simulated ion yield for each atomic layer indicates that this additional scattering signal may be attributable to incident ion 'focussing', an effect seen in previous MEIS investigations. In this study the suggestion is that the shadow cones cast by the out-of-plane bridge site Au adatoms have the effect of focussing the incident ion flux onto the atoms in the adjacent scattering planes, thus leading to a small increase in the scattered ion signal.

5.3.3 General discussion

In comparing the two competing models of the Au/thiolate interface, namely the fcc AAM model and the bridge site AAD model, it is clear that the AAD model is the one favoured by this MEIS study. Two important questions remain, however, and the first of these concerns the difference in yield between the simulated AAD model and the experimental data in the $[\bar{1}\bar{1}2]$ geometry, with the experimental yield lower by ~ 0.1 layers. Given the difficulties involved in the determination of an accurate λ scaling factor, is this theory/experiment discrepancy really significant? This discrepancy is only slightly less than 4% of the average total scattered ion yield in this geometry, and were the clean surface assumed to adopt a 90% herringbone reconstruction, the resulting change in the absolute yield calibration would redress the imbalance. This change in the calibration, however, would reduce the thiolated surface yield in the $[\bar{1}\bar{1}0]$ incidence geometry by $\sim 3\%$, or 0.05 layers, worsening the fit between theory and experiment in this geometry. Thus, we can conclude that the yield mismatch between experiment and theory in the $[\bar{1}\bar{1}2]$ lies at the margin of the experimental precision in this experiment, and that the overall fit for the AAD model seems reasonable.

The second question worth asking is one concerning the inter-layer spacing of the Au adatoms in the AAM model. We have assumed a spacing consistent with that of the bulk, with the Au adatoms therefore situated in bulk continuation sites, with the slight yield increases evident in the fcc AAM simulated blocking curves attributable to the use of enhanced surface vibrations. This scattering yield could be enhanced still further if the adatom vibrational amplitudes were increased to a greater extent, or if the adatom-surface inter-layer spacing were to be changed. Of these two, allowing some modification of the inter-layer spacing seems more reasonable, and as such simulations have been performed for AAM modes which incorporate either an inward or outward inter-layer spacing change of 0.2 Å, this value being perhaps the upper limit of what is reasonable. We find that it is the movement of the Au adatoms *inward* towards the surface layer that results in the largest enhancement of the scattering yield; an increase of ~ 0.1 layers. This results in an experiment/theory overall yield match which is only slightly worse than that for the AAD model, particularly in the $[\overline{1}\overline{1}0]$ incidence geometry, although the substantial blocking dip at a scattering angle of $\sim 110^\circ$ is clearly not present in the experimental blocking curve. The *outward* expansion of the adatom-surface inter-layer spacing results in a smaller ~ 0.05 layers increase in the scattered ion yield. The greater yield change seen with the inward displacement of the adatoms can most probably be attributed to the smaller shadow-cone radius at the underlying atom position. Unfortunately, the true adatom inter-layer spacing in this system is not well established; the theoretical studies of the AAM model, which have been referred to previously, fail to report an inter-layer spacing for the lowest energy structure.

5.4 Conclusions

MEIS has been used to investigate the structure of the thiolate/Au interface in the Au(111)$(\sqrt{3} \times \sqrt{3})$R30°-$CH_3S$ system. The overall scattered ion signal drops significantly upon the adsorption of the methylthiolate species due to the lifting of the clean Au(111) $(22 \times \sqrt{3})$rect. 'herringbone' reconstruction, but the resulting absolute scattering yield is still higher than that expected for a (1×1) unreconstructed Au(111) surface. We cite this as direct evidence of the presence of a significant quantity of Au adatoms at the buried thiolate/surface interface. Simulations of the two basic models proposed for this adatom structure, namely the Au-adatom-monothiolate (AAM) and Au-adatom-dithiolate (AAD) model, have been compared to experiment. The overall scattering yield of simulations for the AAM model appears to be highly sensitive to the exact (and not well-established) values for the adatom-surface inter-layer spacing and the vibrational amplitudes of the atoms, leading to some uncertainty surrounding the predicted yield of the thiolated surface. Nevertheless, this study finds in favour of the AAD model, characterised by 0.17 ML of Au adatoms which occupy bridging sites at the interface between the Au(111) surface and the methylthiolate overlayer.

Chapter 6

Evidence for adsorbate-induced reconstruction via backscattered ion yields

6.1 Introduction

In this chapter the results are presented of two additional medium energy ion scattering (MEIS) investigations of possible adsorbate-induced reconstructions of metal surfaces. In both cases a lack of detailed information in the literature regarding specific structural models has limited the ability to reach any firm quantitative structural conclusions, but some general features of the surface structures adopted upon adsorption could be identified.

6.2 Alanine on Cu(110)

6.2.1 Introduction

Many biological molecules posses an intrinsic chirality, or handedness, leading to two geometrically distinct forms of such molecules, called enantiomers, which are mirror images of each other. Despite the fact that these molecules are chemically identical, living organisms will often react physiologically in very different ways to opposite enantiomers; thus within the chemical and pharmaceutical industries there is a great need for enantioselective catalysis, in which chemicals can be produced in quantity with a high degree of enantiomeric purity. Whilst most success to date involves homogeneous catalysis [124], much effort is being directed towards developing heterogeneous enantioselective catalysts, with a common candidate system comprising an organic chiral 'modifier' molecule adsorbed on a non-chiral metal surface [125]. The necessity of understanding the behaviour of these systems at the molecular level has led to surface science investigations of a variety of chiral modifier molecules adsorbed on single crystal metal surfaces, probed by a range of experimental techniques. This large body of work is summarised in a number of reviews [125–128].

Perhaps the most studied of these systems is that in which the amino acid alanine ($NH_2CH_3C^*HCOOH$) deprotonates to form $NH_2CH_3C^*HCOO$- (alaninate) which then adsorbs upon Cu(110). Alanine is the most simple amino acid which exhibits chirality, this being manifest about the C atom labelled C*, with the two resulting enantiomers referred to as S-alanine and R-alanine. The Cu(110)-alaninate system is characterised by a number of distinct surface structural phases of differing molecular coverages, extensively investigated by Barlow et al. [129]. One high coverage phase involving exposure to a single enantiomer, in which the alaninate species bond to the Cu surface through both the amino N atoms and the carboxylate O atoms, possesses a long range order shown by the (3×2) low-energy electron diffraction (LEED) pattern obtained from this surface. STM studies of this surface phase indicate that the (3×2) unit cell contains two molecules, thus the molecular coverage associated with this phase is 0.33 ML. This structural phase differs from the other high coverage phases in that the arrangement of the molecules with respect to the surface is achiral. An unusual feature of this surface is that the LEED pattern shows missing spots which imply the presence of glide planes, comprising both a reflection through a plane perpendicular to the surface and a translation parallel to this plane. This interpretation cannot be strictly true, however, in a case such a this in which the adsorbed species is a single enantiomer of a chiral molecule, as such molecules are by definition distinct from their mirror forms. By way of contrast, let us briefly consider a similar (3×2) phase formed when Cu(110) is exposed to the simplest (non-chiral) amino acid glycine (NH_2CH_2COOH) [130]. This molecule also deprotonates, forming a glycinate, NH_2CH_2COO-, which then bonds to the surface through both the amino N atoms and the carboxylate O atoms. Whilst glycine molecules are not inherently chiral in their free from, the adsorbed gylcinate species do possess a chirality, and can therefore exist on the surface as two distinct enantiomers. Here again there exist two adsorbate molecules per unit cell, but each molecule adopts a different enantiomeric form. Therefore, in this phase a true glide symmetry exists, reflected in the characteristic missing spots seen in the LEED pattern obtained from this surface.

As stated previously, no such true glide symmetry is strictly possible within the Cu(110)(3×2)-alaninate surface phase formed from a single enantiomer, as the overlayers are by definition homochiral. In order to understand the apparent presence of glide

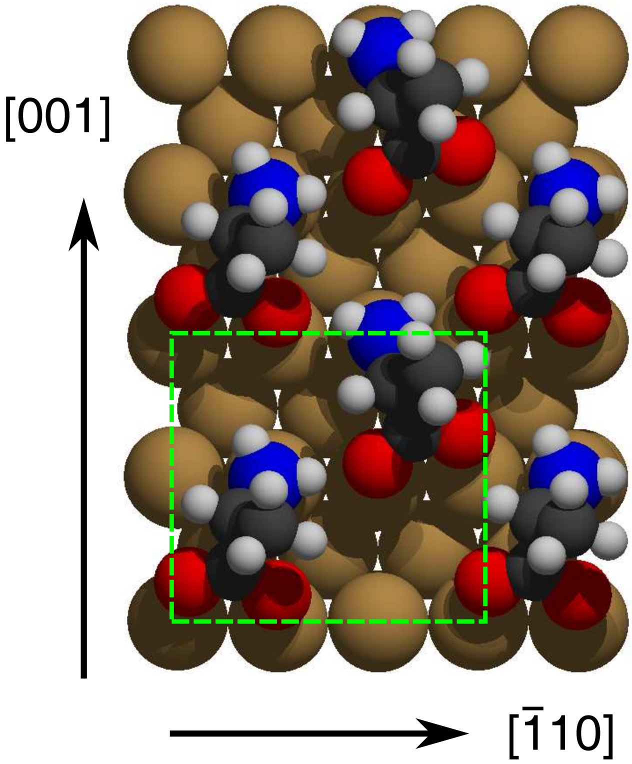

Figure 6.1: Schematic plan view of the Cu(110)(3×2)-alaninate surface structure found to give the lowest total energy in DFT calculations by Rankin and Sholl [131]. The black spheres represent C atoms, the red spheres O atoms and the blue spheres N atoms. Also shown in green is the outline of the (3×2) unit cell.

planes in this phase it has been found to be informative to consider separately the chirality of the molecule and that of its footprint on the surface. In this manner a homochiral Cu(110)(3×2)-alaninate overlayer could involve adsorbed molecules with different footprint motifs, or different local bonding geometries, and so be heterochiral in terms of footprint chirality, giving rise to pseudo-glide planes and a missing-spot (3×2) LEED pattern [129]. A density-functional theory (DFT) study of the Cu(110)(3×2)-alaninate phase has found such a configuration involving mirrored footprints to be energetically favourable [131]. This particular configuration, shown in figure 6.1, involves a triangular footprint formed by the bonding of the carboxylate O atoms to adjacent Cu atoms along the close-packed [$\bar{1}10$] rows and the amino N atom bonding to one of two possible Cu atoms in the neighbouring row, with two possible triangular footprints thus created which are (translated) mirror images of each other in the [001] glide plane. A subsequent experimental investigation using photo-electron diffraction (PhD) [132] found the DFT model (with minor modifications) to provide a good description of the experimental data. One advantage of this configuration is that no Cu surface atom is required to bond with multiple adsorbate molecule atoms, as is the case for a number of other suggested configurations.

Whilst it might seem that the structure of the Cu(110)(3 × 2)-alaninate phase is now relatively well understood, questions still remain, one of which being whether or not the adsorbed alaninate species triggers a significant lateral distortion of the underlying Cu(110) surface layer. This possibility had first been raised by Barlow et al. [129], as such a distortion would result in a heterochiral surface layer whose asymmetry might contribute to the pseudo glide symmetry seen in the LEED. In addition, a more recent study [133] utilising a number of techniques has found evidence of a lack of true long range periodicity in the Cu(110)(3 × 2)-alaninate phase as seen with STM (scanning-tunneling microscopy), with a large lateral surface layer distortion suggested as a possible reason for this loss of periodicity. The same study concluded that the high coverage (3 × 2) phase is generally more complex than had been initially assumed, this complexity prompting further experiments by the authors using quantitative analysis of LEED intensity-energy spectra so that further light might be shed on the organisational details of this phase [134].

In the remainder of the section an investigation of the Cu(110)(3 × 2)-alaninate surface using medium energy ion scattering (MEIS) is presented. The primary aim is to establish whether there exists a significant degree of lateral distortion of the Cu surface atomic layers for the alanine dosed surface, and, if evidence of such distortion is found, elucidate the details of this distortion. MEIS is ideally suited to answer such a question, as given a suitable ion incidence direction which exploits the characteristic shadow-cones to ensure the majority of the ions backscatter from only the surface region, any lateral distortion of the surface layers will result in a quantifiable increase in the scattering signal with respect to that obtained from a clean and undistorted Cu(110) surface.

6.2.2 Experimental details

The MEIS data were collected at the UK National MEIS facility at the Daresbury Laboratory, Cheshire, UK. The Cu(110) sample disc was spark-machined from a single crystal bar and subsequently mechanically polished using successively finer grades of diamond paste. This sample, upon being loaded into the Daresbury ultra-high-vacuum (UHV) chamber system, was prepared by the usual cycles of 1.5 keV Ar^+ ion sputtering at grazing incidence followed by annealing to $\sim 550°$C. The resulting clean Cu(110) surface was judged contaminant free by Auger electron spectroscopy, and deemed well-ordered by LEED (Low Energy Electron Diffraction).

Alanine powder, of 99% purity and consisting solely of the S-enantiomer was obtained from Sigma-Aldrich and mounted in an UHV evaporation source. This source was attached via an externally pumped line to the sample preparation chamber, with the alanine vapour introduced to the sample via a gate valve. The source and gate valve were mounted in such a way as to ensure a direct line-of-sight between the sample and the source. The evaporation source itself comprised a glass tube housed within a ceramic cylinder; this was heated by the passage of a current through a copper wire wrapped around the cylinder itself. This ceramic tube had the effect of improving the homogeneity of the heating, with the evaporation rate controlled by monitoring the temperature of tantalum caps on both ends of the source via thermocouple. The initial complex $\begin{pmatrix} 2 & -2 \\ 5 & 3 \end{pmatrix}$ saturation coverage phase [129] was formed by exposing the clean Cu(110) surface, held at $\sim 103^\circ$C, to a regulated flux of L-alanine characterised by a partial pressure of 3.0×10^{-8} mbar, for a duration of 45 minutes. This existence of this phase having been confirmed by LEED, the sample was then flash-annealed to a temperature of 170°C, leading to a LEED pattern characteristic of the (3×2) phase.

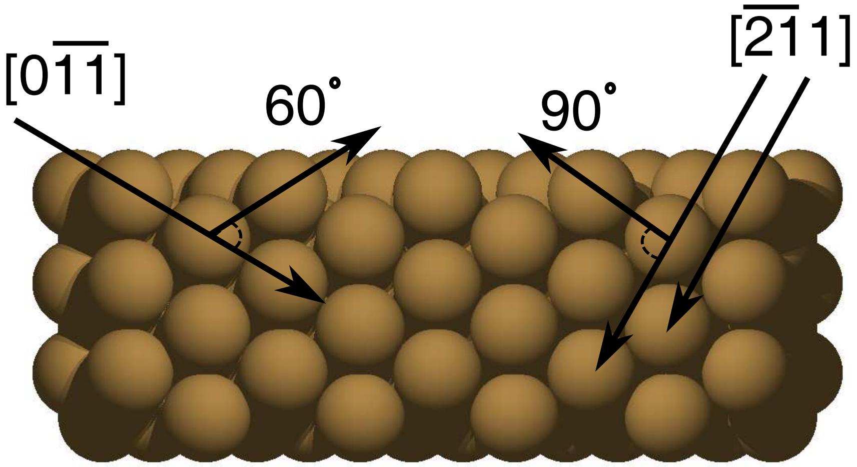

Figure 6.2: A side view of the Cu(110) crystal, showing the scattering plane used in the experiment together with the two distinct ion incidence directions, namely the $[0\overline{1}\overline{1}]$ and $[\overline{2}\overline{1}1]$ directions, which illuminate the uppermost 1 and 2 atomic layers respectively. Also shown are the directions which lead to major blocking of the backscattered ions.

MEIS data were collected on both the Cu(110)(3×2)-alaninate phase and the clean Cu(110) surface using 100 keV H^+ ions in two distinct scattering geometries. These geometries, shown in figure 6.2, involved ions incident in the $[0\overline{1}\overline{1}]$ and $[\overline{2}\overline{1}1]$ directions, leading to the nominal illumination of only the uppermost 1 and 2 atomic layers, respectively. Data were collected over a wide range of scattering angles with care being taken to limit the incident ion dose on any particular region of the surface to $4\,\mu$C (as measured by the tungsten wire mesh in the path of the beam described in section 2.4). No evidence of beam-induced surface damage was seen in either the MEIS data or in LEED patterns obtained after the main scattering experiment. Experimental scattered ion yields were calibrated absolutely in terms of visible atomic layers using the signal from the clean Cu(110) surface and VEGAS yield simulations of the well-characterised structure associated with this surface.

6.2.3 Results and discussion

The experimental blocking curves resulting from the MEIS investigation of the both the clean and (3×2)-alaninate covered Cu(110) surfaces are shown in figure 6.3. It is immediately apparent, upon visual inspection, that the overall scattering signal measured from the S-alanine dosed surface is identical, within the bounds of statistical error, to that measured from the clean surface, this being true in both of the scattering geometries. The shapes and sizes of the blocking features indicative of the positions of the surface atoms are also in very good agreement, although there are some differences. Perhaps the largest disparity is a modest local yield difference in the blocking dips in the region of the $[\overline{2}\overline{1}1]$ incidence blocking curve corresponding to the scattering of ions through an angle of $\sim$ 80°. Another disagreement is manifest in the relative position and depth of the large blocking dip at a scattering angle of $\sim$ 60° in the nominal 1-layer illumination geometry ($[0\overline{1}\overline{1}]$ incidence). Here the dip from the dosed surface is slightly deeper ($\sim$ 0.1 atomic layers), with a yield minimum centred on 60°, as opposed to the dip from the clean surface, which is located at 59°, a shift of approximately 1°. Whether such a small movement is of any significance is a question which will be addressed shortly. What is clearly obvious, however, is the lack of a large overall increase (indeed any increase) in the scattered ion signal expected for alaninate-induced modification of the Cu(110) surface. This being said, however, it will subsequently be shown that given some reasonable assumptions regarding the amplitudes of both the surface Cu atom thermal vibrations and the relaxations of the Cu(110) layers perpendicular to the surface, a case can be made for the existence of a small amount of movement of the surface Cu atoms.

The results of a simulation of the clean Cu(110) surface are also shown in figure 6.3. As mentioned in the previous section, it is the yield from these simulated blocking curves which has been used as an absolute calibration for the experimental yield from both clean and dosed surfaces. Thus the absolute yields in visible atomic layers expressed in figure 6.3 are strongly influenced not only by the clean surface relaxations, but also by the surface vibrational amplitudes of the clean Cu(110) surface. The root-mean-square (rms) vibrational amplitudes in the subsurface layers were set to 0.079 Å (consistent with the bulk Debye temperature), with the vibrations in the surface layer enhanced

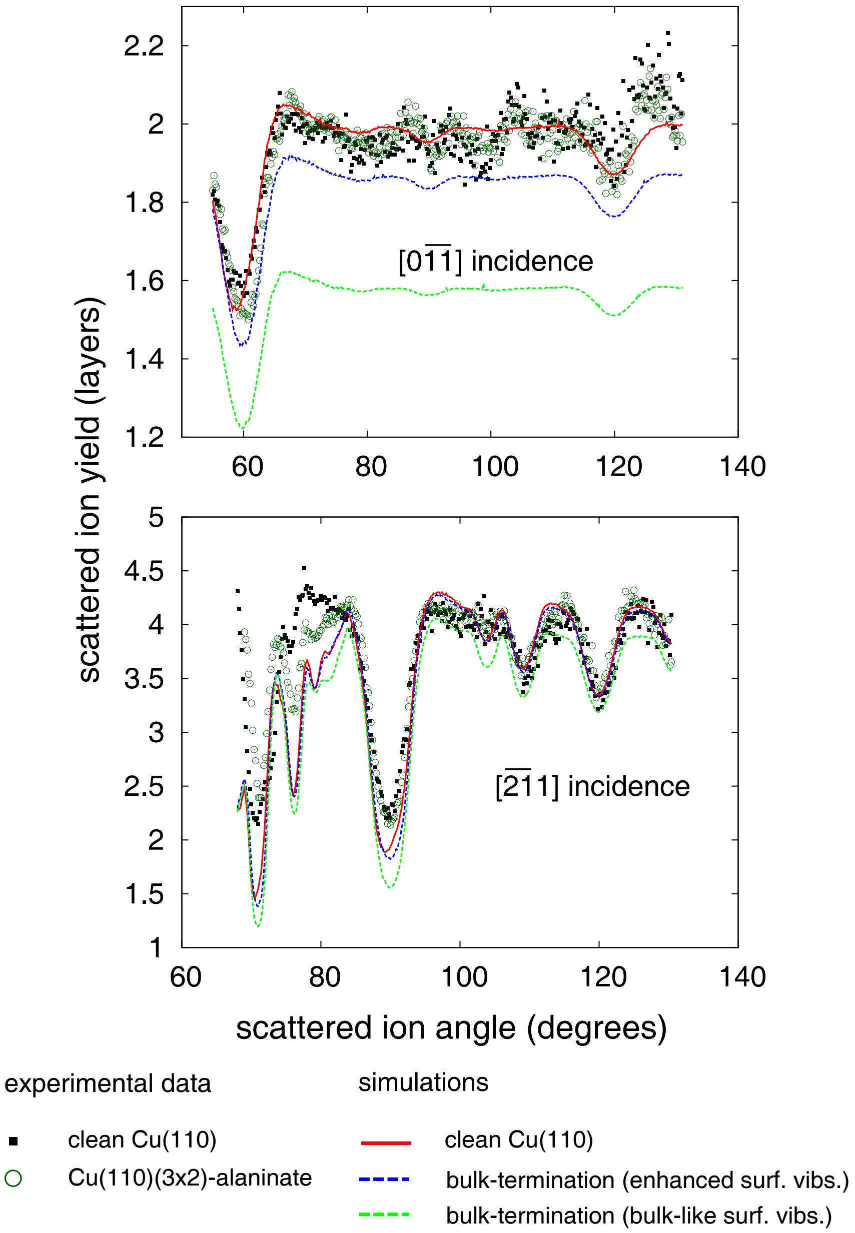

Figure 6.3: MEIS experimental blocking curves for 100 keV H$^+$ ions backscattered from the clean Cu(110) and Cu(110)(3 × 2)-alaninate surfaces. Blocking curves are included for ions incident in both the $[0\bar{1}\bar{1}]$ and $[\bar{2}11]$ directions, corresponding to a nominal illumination of 1 and 2 surface layers, respectively. Simulations for the relaxed and unrelaxed clean Cu(110) surfaces are also shown.

(isotropically) by a factor of $\sqrt{2}$. The outermost inter-layer spacing was contracted by 7.5%, whilst the spacing between the 2nd and 3rd atomic layers was expanded by 2.5%. These surface relaxations are those found in an earlier MEIS study of the clean Cu(110) surface [135].

Also included in figure 6.3 are simulated blocking curves from an unrelaxed surface, with the surface atoms occupying bulk-continuation sites, and with the thermal vibrations of the atoms treated as those in the clean Cu(110) model, including the surface $\sqrt{2}$ enhancement. In comparison to the clean surface simulations, this results in a yield drop of of roughly 0.1 layers in the $[0\overline{1}\overline{1}]$ incidence geometry, with a somewhat smaller yield decrease evident in the $[\overline{2}\overline{1}1]$ geometry. Note that although the apparent lowering of yield in the $[\overline{2}\overline{1}1]$ geometry is very small, this is partially due to the much greater range of the ordinate axis in this geometry. The overall yield increase when moving from the unrelaxed surface to the clean one is as expected, and can be entirely attributed to the addition of surface relaxations. These relaxations involve movements of the surface Cu atoms away from the bulk-like positions in which they shadowed the layers below, resulting in an increase in the visibility of the subsurface layers. Notice that the introduction of surface relaxations in the simulations also shifts the position of the major blocking dips in both geometries, with the contraction of the outermost inter-layer spacing of 7.5% giving rise to a shift to lower scattering angle of $\sim 1°$.

Whilst it is clear that the MEIS data do not show a significant increase in scattering signal upon adsorption of the alaninate as expected for a significant adsorbate-induced surface reconstruction, it might be expected that such an adsorption would result in the modification of the relaxed surface inter-layer spacings, as found to be the case in many other cases involving adsorbates on coinage metal surfaces. Indeed, the signal from the alaninate dosed Cu(110) surface is increased by ~ 0.1 layers from that predicted for the unrelaxed surface (simulated blocking curves shown in blue in figure 6.3), implying either a small degree of Cu surface atom movement or a small increase in the (already enhanced) amplitude of the Cu surface atom vibrations. The (3×2) phase structural model used by Rankin and Sholl [131] has a molecular coverage of 0.33 ML, with each molecule bonding to three different surface Cu atoms, thus every surface Cu atom is bonded to an adsorbate atom. As such, the outermost layer of Cu atoms are no longer at the solid/vacuum interface, and this could lead to a pinning of the otherwise enhanced atomic vibrations in this layer. Evidently this would have the effect of *reducing* the scattering signal from the lower atomic layers and so reducing the overall yield, as made clear in the final set of VEGAS simulated blocking curves included (shown in green in figure 6.3), which result from a unreconstructed Cu(110) surface with no $\sqrt{2}$ enhancement in the surface Cu atom vibrations, these instead taking the bulk vibrational amplitudes.

Thus, if we reasonably assume both that the surface Cu atom vibrations become pinned upon alaninate adsorption and that this adsorption has the effect of removing the small surface inter-layer relaxations, the overall mismatch between the experimental scattering signal and that predicted by the theory is a more substantial increase of ~ 0.4 layers in both scattering geometries. Such a yield increase would account for a modest degree of movement of the Cu surface atoms away from their bulk-termination positions.

To the author's knowledge the only detailed model previously proposed in the literature for an alaninate-induced Cu surface reconstruction in the (3×2) phase is that proposed by Rankin and Sholl [131]. The atomic coordinates which define this model have been kindly provided by Rankin & Sholl, and the resultant simulated blocking curves are shown in figure 6.4. Given the important role that the thermal vibrations of the outermost Cu atoms play in determining the absolute scattering yield, two simulations based on the DFT minimum energy structure are shown. The first is characterised by a $\sqrt{2}$ enhancement of the outermost Cu atom vibrations with respect to those of the bulk (as is usual for atoms at the vacuum interface) and the second is without this enhancement, as has been previously suggested to be likely given the high coverage of adsorbed alaninate species. Both models are otherwise identical and involve a relatively small degree of movement of the outermost Cu atoms, both laterally and perpendicular to the surface. The alaninate species are bonded in a heterochiral triangular footprint geometry through the two oxygen atoms and the nitrogen atom as shown in figure 6.1. All of these atoms are removed from bulk-continuations sites, thus we expect the adsorbed alaninate molecules to contribute very little to the scattering signal from the Cu surface in the form of shadowing. In this way the MEIS is sensitive only to the small degree of movement of the outermost Cu atoms. It is clear from figure 6.4 that, if we sensibly assume that the outermost Cu atoms have their otherwise enhanced vibrations pinned to the values of those in the bulk, the movement of the Cu atoms proposed by the DFT is insufficient to account for the experimentally observed yield. If, however, the enhancement is not removed, the yield predicted for the DFT model is in much better agreement with experiment, although it is noteworthy that in the otherwise relatively insensitive 2 layer illumination $[\overline{11}2]$ geometry the predicted yield is somewhat higher than that seen experimentally. It is also clear that these models account for the small angular shift seen in the major blocking dip at 60° scattering in the $[0\overline{11}]$ geometry. In considering the validity of the Rankin and Sholl DFT model, then, it would seem that although the blocking features of both simulation and experiment are in good agreement, given reasonable assumptions concerning the thermal vibrations of the outermost Cu atoms, the movement of these atoms is less than is the case in reality, as shown by MEIS.

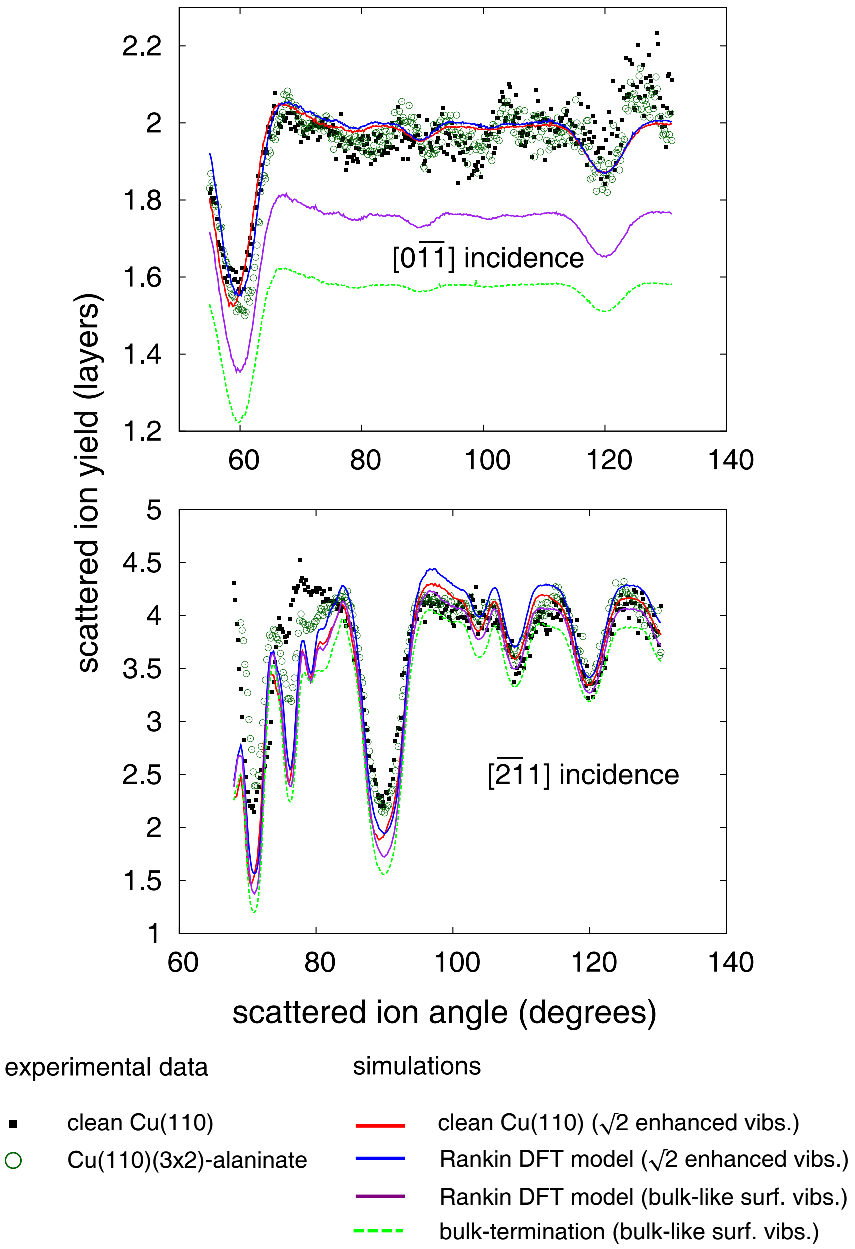

Figure 6.4: MEIS experimental blocking curves for 100 keV H$^+$ ions backscattered from the clean Cu(110) and Cu(110)(3×2)-alaninate surfaces. Blocking curves are included for ions incident in both the $[0\bar{1}\bar{1}]$ and $[\bar{2}11]$ directions, corresponding to a nominal illumination of 1 and 2 surface layers, respectively. Simulations of scattering from the DFT model proposed by Rankin & Sholl [131] and the relaxed and unrelaxed clean Cu(110) surfaces are also shown.

It is clear that in order to gain further insight into the nature of the alaninate-induced reconstruction, further work must be undertaken. This work would need to focus on characterising the general nature of the reconstruction, so that MEIS could then be used to accurately determine the structural details.

6.2.4 Conclusions

MEIS has been used to investigate the possibility of a reconstruction of the outermost surface atomic layers in the Cu(110)(3 × 2)-alaninate system. The data do not show any increase in the overall Cu scattering signal upon adsorption of the alaninate species, and at first inspection this might be taken as evidence of little or no movement of the Cu surface atoms away from their positions on the clean Cu(110) surface. However, if one reasonably concludes that the adsorbed alaninate pins the vibrational amplitudes of the outermost Cu atoms, then the observed Cu scattering yield from the Cu(110)(3 × 2)-alaninate surface is consistent with a modest reconstruction of the surface Cu atoms. The extent of this reconstruction seems larger than that involved in the only structural model proposed to date, that found to give the minimum energy in DFT calculations by Rankin and Sholl.

6.3 Methylthiolate induced reconstruction on the Pd(111) surface

6.3.1 Introduction

Self-assembled monolayers (SAMs), which are formed by the interaction of n-alkanethiols ($CH_3(CH_2)_{n-1}SH$) with metal surfaces, have long been of the subject of scientific investigations [63–67], as such SAM systems have a range of actual and potential applications (e.g. [68–70]). The SAMs in such systems form when the n-alkanethiol deprotonates to form a thiolate ($CH_3(CH_2)_{n-1}S$) which then bonds to the metal surface through the S head-group. These systems are also fortuitously easy to prepare in both solution and under ultra-high-vacuum (UHV) conditions, with the latter conditions allowing the use of a whole armoury of surface science techniques to investigate the properties of these systems. Whilst the majority of this research has focused on the coinage (or noble) metals, in part due to the low reactivity of these surfaces with respect to possible contaminant species, some interest has been directed at other transition metal surfaces. One such surface is that of palladium, popular in part due to its known affinity for sulphur-containing compounds [136].

There is a lack of early experimental studies of n-alkanethiols on palladium, with the first treatment of this system being an ab-initio theoretical consideration of methylthiolate (n = 1) bonded on Pd(111) [137]; this study found that the S head-group preferred to bond in a 3-fold coordinated hollow site. More recently, experiments have been undertaken to characterise the structure of SAMs formed on thin Pd films using n-alkanethiols for a range of n values [138]. This investigation utilised optical ellipsometry, reflection absorption infrared spectroscopy (RAIRS) and X-ray photoelectron spectroscopy (XPS). The films themselves were produced by evaporation, with the resulting poly-crystalline films showing a strong (111) texture. The SAMs of thiolate species were formed either through exposure within solution or by micro-contact printing. The authors found evidence for the existence of a thin PdS interphase of a thickness no more than $10-20\,\text{Å}$ upon which the S head-groups of the thiolate species were adsorbed. The ratio of the thiolate to the sulphide species was found to be between 1 : 1 and 1 : 2, with the extra S required for this interphase proposed to be sourced by the clean excision of S atoms from the excess adsorbate in the solution. The thiolate packing density was found to agree well with that of the ubiquitous 0.33 ML $(\sqrt{3}\times\sqrt{3})\text{R}30^\circ$ high coverage phase formed by n-alkanethiolates on Au(111) single crystals. To our knowledge there are no experimental studies of n-alkanethiolates bonded on the single-crystal Pd(111) surface, but such surfaces have been exposed to H_2S to to form ordered phases of atomic sulphur [139]. Scanning-tunneling microscopy (STM) and low-energy electron diffraction (LEED) showed low coverage phases with a $(\sqrt{7}\times\sqrt{7})\text{R}19.1^\circ$ surface periodicity and at higher coverages a $(\sqrt{3}\times\sqrt{3})\text{R}30^\circ$ phase was formed with a characteristic S coverage of 0.33 ML.

Here we present the results of a medium energy ion scattering (MEIS) study of the Pd(111)-CH_3S surface, with a view to answering the question of whether there exists a thiolate-induced reconstruction of the Pd(111) surface atomic layers, as has been found to be the case for many SAM/Metal single crystal interfaces (see chapters 3 and 4).

6.3.2 Experimental details

The experiments were performed at the Daresbury Laboratory, UK, in the national MEIS facility. The Pd(111) sample was formed by spark-machining from a single crystal bar, followed by a series of mechanical polishes using successively smaller grades of diamond paste. The sample was prepared in situ. via the normal methods, involving cycles of 1.5 keV Ar^+ ion bombardment followed by annealing to $\sim 600^\circ$C. This resulted in a clean and well ordered surface, as judged by Auger electron spectroscopy and LEED. Methylthiolate was adsorbed on the clean Pd(111) surface via exposure to a vapour of dimethyldisulphide (DMDS - $CH_3S\text{-}SCH_3$). This molecule is known to break up in the presence such metal surfaces via the scission of the S-S bond to form two methylthiolate species, which then bond to the surface through the S head-group. DMDS is used in preference to methylthiol due to its lower toxicity and greater ease of handling. The DMDS vapour was introduced to the sample through a leak valve connected to a glass ampoule containing the DMDS in liquid form, with the external section containing the ampoule having been previously purified by several freeze/thaw pumping cycles. Two different exposures were conducted, the first involving a DMDS partial pressure of 1×10^{-8} mbar and an exposure time of 15 minutes, the second characterised by a 10 minute exposure at a partial pressure of 1×10^{-7} mbar. In both cases the Pd(111) sample was held at room temperature. LEED was not used to characterise the periodicity/long-range-order of the the resulting Pd(111)-CH_3S surfaces, due to the known high cross-section for electron irradiation damage associated with such thiolate surfaces. LEED was used on the surface formed by the first exposure after this surface had been investigated with MEIS, but no diffraction pattern was seen, indicating a lack of an ordered periodic structure associated with the thiolate overlayer.

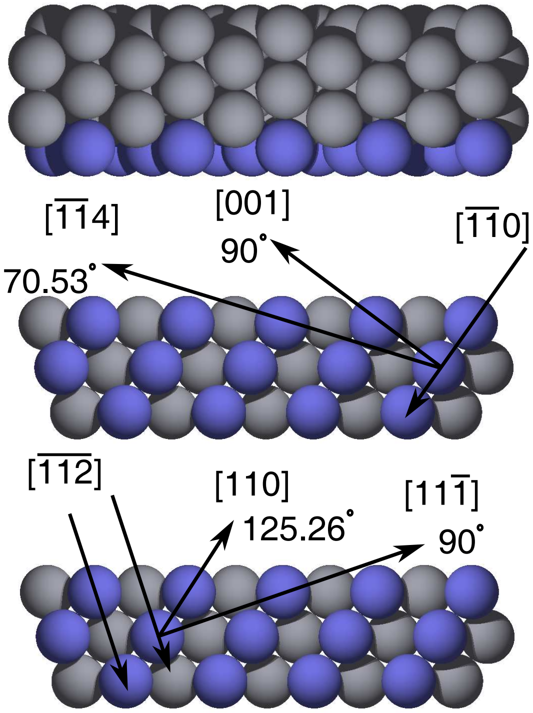

Figure 6.5: Plan and side views of a Pd(111) surface showing the incidence directions used in this investigation. Ions incident in the [$\overline{11}0$] direction will nominally illuminate only the surface layer, whilst those incident along the [$\overline{112}$] direction nominally illuminate the top two layers. The main outgoing directions and associated scattering angles along which backscattered ions experience atomic blocking are also shown.

Both the clean Pd(111) and Pd(111)-CH_3S surfaces were then exposed to 100 keV

H^+ ions incident in two distinct directions, so as to obtain MEIS blocking curves. These directions were the $[\overline{1}\overline{1}0]$ and $[\overline{1}\overline{1}2]$, such that the incident ions would illuminate only the top or the top two atomic layers for a surface with atoms in bulk-continuation sites, and without the presence of atomic thermal vibrations. In reality, of course, neither of these conditions are met, with lower atomic layers contributing significantly to the backscattering yield, but the use of such major crystallographic directions ensures that most of the scattering signal is from ions scattered in the surface region, as the atoms of the bulk lie within the shadow cones cast by those in the first few atomic layers. Figure 6.5 shows these two scattering geometries, including the outgoing directions along which ions are expected to be strongly blocked by atoms in the top few layers.

Absolute calibration of the experimental scattering signal was achieved by comparing the yield associated with scattering from the Pd(111) surface to the yield predicted from VEGAS simulations of scattering from the clean Pd(111) surface.

6.3.3 Results and discussion

Figure 6.6 shows the experimental blocking curves obtained for both the clean Pd(111) and Pd(111)-CH_3S surfaces. Shown alongside the clean experimental blocking curves are those resulting from a VEGAS simulation of the clean surface. As mentioned previously, it is this simulation which has been used to arrive at an absolute yield calibration for the experimental blocking curves in terms of visible atomic layers. The VEGAS model for the clean Pd(111) surface includes an outward expansion of both the first and second inter-layer spacings by 4.3% and 2.0% respectively, values found in a previous study of the clean surface by Tensor LEED [140]. The amplitudes of the bulk root-mean-square (rms) vibrations were set to a value of 0.074 Å, a value consistent with the bulk Debye temperature, with the vibrations in the surface layer isotropically enhanced by a factor of $\sqrt{2}$.

The Pd(111)-CH_3S experimental blocking curves in figure 6.6 both show a large increase in the scattering signal compared to that of the clean surface. This yield increase of ~ 0.6 layers in both geometries can only be caused by a significant degree of atom movement in the outermost 1 or 2 atomic layers of Pd(111), or a significant enhancement of the surface atom vibrational amplitudes over those of the clean surface. Given that the clean surface vibrations are already characterised by a significant amplitude enhancement with respect to those of the bulk, the latter cause seems highly unlikely. Therefore we infer that the adsorption of methylthiolate on the Pd(111) surface is accompanied by a significant reconstruction of the outermost Pd atomic layers. The remaining question is whether the MEIS data allow us insight into the details of this reconstruction, be it in terms of general characterisation or more quantitative detail.

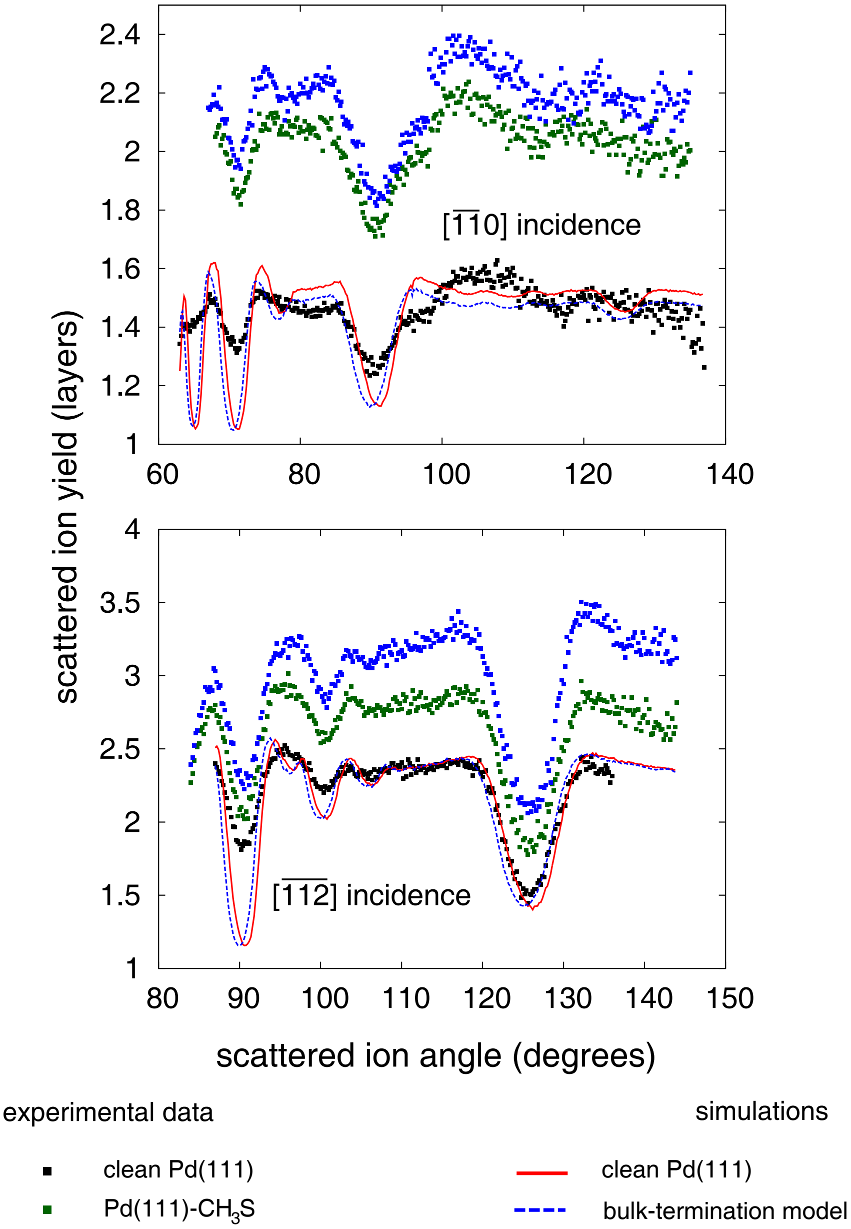

Figure 6.6: The blocking curves resulting from the investigation of the clean and methylthiolate covered Pd(111) surfaces using MEIS, with 100 keV H^+ ions incident in two distinct directions, namely the [$\bar{1}\bar{1}0$] and [$\bar{1}\bar{1}2$] directions. In both geometries the large increase in the scattering signal upon adsorption of the methylthiolate species is indicative of a significant reconstruction of the Pd surface layers.

Unfortunately, there is a lack of information within the literature pertaining to the details of the structural phases of Pd(111)-CH_3S, including whether any of these phases exhibit any long range order, this knowledge being necessary in order to accurately determine surface structural details using MEIS.

In addition to its role as a probe of surface structure, analysis of the intensities of the scattering signals from multiple surface elements can serve to determine the composition of the surface region. In this way the coverage of methylthiolate species has been estimated from the ratio of the areas of the characteristic peaks in energy in the MEIS data which correspond to scattering from S and Pd. So as to minimise the background signal contributed by ions backscattered by Pd atoms in deeper layers, this peak ratio determination was undertaken using the signal obtained in a so-called 'double alignment' geometry (namely ions incident along the $[\overline{1}\overline{1}0]$ direction and exiting along the [001] direction). This leads to an estimated methylthiolate species coverage of $\sim 0.38\,\mathrm{ML}$. Due to the difficulty in extracting the area of the S energy peak, a function of the extremely poor signal to noise ratio for a light element such as S, this coverage estimate is not very precise. Difficulties also arose when attempting to fully subtract the Pd scattering background signal. For this reason the coverage estimate given above should be treated as an upper estimate, with the true coverage expected to be somewhat lower. As such the coverage found in this investigation is consistent with the 0.33 ML saturation coverage seen for methylthiolate on Au(111).

6.3.4 Conclusions

An investigation of the Pd(111)-CH_3S surface using MEIS has been carried out. The data show a large adsorbate-induced increase in the Pd scattering signal, consistent with a considerable amount of atomic movement on the Pd(111) surface. MEIS has also been used to probe the composition of the surface region, with the adsorbate coverage found to be 0.38 ML.

Chapter 7

Concluding remarks

In this thesis, the experimental technique of medium energy ion scattering (MEIS) has been used to investigate the structural details of adsorbate-induced surface reconstructions for a range of adsorbate species and single crystal metal substrates. The surface systems studied fall into two different categories, with the first comprising well-studied surface systems for which some degree of uncertainty remains; here MEIS has been used to provide additional quantitative insight to help answer outstanding questions. By contrast, the systems in the second category are characterised by a much lower level of background structural information within the literature, information that is necessary for the kind of quantitative analysis undertaken on the first set of systems. For this second type of system, MEIS has nonetheless been able to provide insight into the more general properties of the surface reconstructions.

An investigation of the Cu(410)-O stepped surface was undertaken using 100 keV medium energy H^+ ions, incident in six distinct geometries. These geometries were selected so as to nominally illuminate either 1, 2 or 3 atomic layers in both the 'up-step' and 'down-step' directions. These directions, whilst equivalent with respect to the (100) terraces, are rendered inequivalent on the reduced-symmetry (410) surface. A series of surface relaxation models proposed previously by surface X-ray diffraction (SXRD) and density functional theory (DFT) were tested by comparing the simulated blocking curves for these models with those of the experiment. None of the models provided a complete description of the data, and so an optimisation was undertaken using the IFFCO optimisation routine. Each of the initial models involved the use of 16 distinct parameters to define the surface structure. Although it was deemed computationally and fundamentally not feasible to simultaneously optimise all sixteen (potentially coupled) parameters, it was found to be possible to optimise the eight key structural parameters which defined the positions of the Cu atoms at the solid/vacuum interface. This resulted in a best-estimate structure which was broadly similar in its detail to the literature models, although some significant quantitative differences remain.

The possibility of an adsorbate-induced surface lateral radial distortion on the Cu(100)(2 × 2)-CH_3S surface, suggested on the basis of a pseudo-(100) reconstruction found for methylthiolate on Cu(111), was investigated using MEIS. The (2 × 2) structural phase involves 0.25 ML of thiolate species which bond through the S head-group, situated in a 4-fold coordinated hollow site. One possible mechanism to relieve the lateral stress imposed on the Cu surface by the adsorbed thiolates would involve a lateral radial outward expansion of the four Cu atoms surrounding each S head-group. Data were gathered in three distinct incidence geometries, including normal incidence, and the resultant blocking curves were compared with simulations for lateral radial distortions of a range of magnitudes. Small perpendicular relaxations of the outermost Cu atoms were also considered along with the possibility of adsorbate induced changes to the surface Cu atom vibrational amplitudes. The optimal value for the outward radial lateral Cu atom movement was determined as 0.12 ± 0.04 Å, and this was found to be accompanied by and outward expansion of the first Cu layer spacing of 0.08 ± 0.04 Å.

MEIS has been used in an attempt to ascertain the structure adopted by the surface in the Au(111)($\sqrt{3} \times \sqrt{3}$)R30°-CH_3S system. Although this system has been much studied, there are two distinct surface structure models proposed, namely the Au-adatom-monothiolate (AAM) and the Au-adatom-dithiolate (AAD). The former model involves a thiolate-Au moiety, in which the S head-group bonds to the Au adatom, which then bonds to the Au(111) surface in a 3-fold coordinated hollow site. This moiety bonds on the surface such that the thiolate species resides in a local atop site. In the AAD model, a thiolate-Au-thiolate moiety exists with the thiolates again bonding to the Au adatom through the S head-group. This exists on the surface with the Au adatom occupying a 2-fold coordinated bridge site, with the moiety oriented such that the S head-group atoms again exist in a local atop site, albeit atop an underlying Au(111) surface atom in the AAD model as opposed to the Au adatom for the AAM model. The fact that the local bonding sites of the S head-group atoms are very similar for these two models has made it difficult for more commonly used structural techniques to distinguish these two possible structures. Thus the MEIS study was carried out, as the MEIS technique offers a way to determine the coverage of Au adatoms, which is 0.33 ML for the AAM model but only 0.17 ML for the AAD model. The presence of the adsorbed thiolate was found to lift the well-known 'herringbone' reconstruction which characterises the clean Au(111) surface, and the observation that the Au scattering signal from the thiolate-dosed surface was higher than that expected for an unreconstructed surface led to the conclusion that a significant number of Au adatoms were present at the buried thiolate/surface interface.

Furthermore, simulations of scattering from the two different surface structures proposed were compared to experiment. Uncertainties concerning some details of the two different models, such as the exact height of Au adatoms above the surface, together with the confidence limits associated with experimental yield calibration had the effect of clouding the conclusions somewhat, nonetheless we found in favour of the AAD model.

MEIS data were gathered on the Cu(110)(3×2)-alaninate system, where the chiral amino acid (comprising solely one enantiomer) bonds to the surface as an alaninate species in an arrangement in which the footprint geometries of the molecule are heterochiral, despite the fact that the molecule itself is homochiral. It has been suggested that the outermost Cu layers might undergo some degree of reconstruction or distortion upon adsorption, and the MEIS data were found to be consistent with a small degree of reconstruction. The only detailed structure proposed in the literature involves a level of surface distortion found to be too small to account for the scattering yield seen in the MEIS data. Before this structure may be fully understood, more basic work must be done to characterise the broad details of this structural phase.

The Pd(111)-CH_3S system was studied using MEIS, and strong evidence for a large adsorbate-induced reconstruction was found via analysis of the backscattering yields. However, the lack of any previous detailed characterisation of this system limited the ability to produce further insight concerning the details of this structure.

To conclude, the technique of MEIS has been used throughout this thesis as a tool for gaining a greater understanding of the structures adopted by surfaces in a range of surface science systems, including the much studied SAM systems.

Bibliography

[1] D. P. Woodruff, Journal of Physics-Condensed Matter **22**, 084016 (2010).

[2] J. F. van der Veen, Surface Science Reports **5**, 199 (1985).

[3] E. J. Williams, Rev. Mod. Phys. **17**, 217 (1945).

[4] H. Goldstein, *Classical Mechanics* (Addison-Wesley, 2002), 3rd ed.

[5] E. Rutherford, Philosophical Magazine **21**, 669 (1911).

[6] M. Ángel Muñoz Márquez, Ph.D. thesis, University of Warwick (2005).

[7] D. J. O'connor and J. P. Biersack, Nuclear Instruments and Methods in Physics Research Section B **15**, 14 (1986).

[8] G. Molière, Z Naturforsch A **2**, 133 (1947).

[9] O. B. Firsov, Soviet Journal of Experimental and Theoretical Phyiscs **6**, 534 (1958).

[10] J. L'Ecuyer, J. A. Davies, and N. Matsunami, Nuclear Instruments & Methods **160**, 337 (1979).

[11] S. R. Lee and R. R. Hart, Nuclear Instruments & Methods B **79**, 463 (1993).

[12] H. A. Bethe, Ann. Physik **5**, 325 (1930).

[13] N. Bohr, Philosophical Magazine **25**, 10 (1913).

[14] J. F. Ziegler, J. P. Biersack, and U. Littmark, *The stopping and range of ions in solids*, vol. 1 (Pergamon Press, 1985).

[15] W. K. Chu, Physical Review A **13**, 2057 (1976).

[16] Q. Yang, D. J. Oconnor, and Z. G. Wang, Nuclear Instruments & Methods B **61**, 149 (1991).

[17] N. Bohr, Kgl. Danske Videnskab. Selskab, Mat-fys. Medd. **18**, 8 (1948).

[18] Y. Kido and T. Koshikawa, Journal of Applied Physics **67**, 187 (1990).

[19] J. B. Marion and F. C. Young, *Nuclear reaction analysis - graphs and tables* (North Holland Amsterdam, 1968).

[20] D. S. Gemmell, Reviews of Modern Physics **46**, 129 (1974).

[21] O. S. Oen, Surface Science **131**, L407 (1983).

[22] J. W. M. Frenken, R. M. Tromp, and J. F. vander Veen, Nuclear Instruments & Methods in Physics Research B **17**, 334 (1986).

[23] R. M. Tromp and J. F. van der Veen, Surface Science **133**, 159 (1983).

[24] J. F. van der Veen, J. B. Sanders, and F. W. Saris, Surface Science **77**, 337 (1978).

[25] R. M. Tromp, M. Copel, M. C. Reuter, M. H. von Hoegen, J. Speidell, and R. Koudijs, Review of Scientific Instruments **62**, 2679 (1991).

[26] I. Antcheva, M. Ballintijn, B. Bellenot, M. Biskup, R. Brun, N. Buncic, P. Canal, D. Casadei, O. Couet, V. Fine, et al., Computer Physics Communications **180**, 2499 (2009).

[27] T. C. Q. Noakes, P. Bailey, and D. P. Woodruff, Nuclear Instruments & Methods B **136**, 1125 (1998).

[28] D. P. Woodruff, D. Brown, P. D. Quinn, T. C. Q. Noakes, and P. Bailey, Nuclear Instruments & Methods B **183**, 128 (2001).

[29] P. R. Bevingtion and D. K. Robinson, *Data reduction and error analysis for the physical sciences* (McGraw-Hill, 2003), 3rd ed.

[30] G. S. Parkinson, M. A. M. noz Márquez, P. D. Quinn, M. J. Gladys, R. E. Tanner, and D. P. Woodruff, Physical Review B **73**, 245409 (2006).

[31] P. Quinn, D. Brown, D. P. Woodruff, T. C. Q. Noakes, and P. Bailey, Surface Science **491**, 208 (2001).

[32] G. S. Parkinson, Ph.D. thesis, University of Warwick (2006).

[33] R. Fletcher, *Practical methods of optimisation* (Wiley, Chichester, 1987), 2nd ed.

[34] P. E. Gill, W. Murray, and M. H. Wright, *Practical optimisation* (Academic Press, London, 1981).

[35] P. Gilmore and C. T. Kelley, SIAM Journal on Optimization **5**, 269 (1995).

[36] C. Davisson and L. H. Germer, Physical Review **30**, 705 (1927).

[37] D. P. Woodruff and T. A. Delchar, *Modern Techniques of Surface Science* (Cambridge University Press, 1994), 2nd ed.

[38] M. A. V. Hove, W. H. Weinberg, and C. M. Chan, *Low energy electron diffraction* (Springer-Verlag Berlin Heidelberg, 1986).

[39] M. Thompson, M. D. Baker, A. Christie, and J. F. Tyson, *Auger electron spectroscopy* (John Wiley & Sons, 1985).

[40] H. Wagner, *Solid Surface Physics* (Springer Berlin/Heidelberg, 1979), chap. Physical and chemical properties of stepped surfaces, Springer Tracts in Modern Physics.

[41] G. Rhead, Surface Science **68**, 20 (1977).

[42] P. Knight, S. Driver, and D. Woodruff, Journal of Physics-Condensed Matter **9**, 21 (1997).

[43] G. Lloyd and D. Woodruff, Surface Science **285**, L503 (1993).

[44] J. Perdereau and G. Rhead, Surface Science **24**, 555 (1971).

[45] S. Reiter and E. Taglauer, Surface Science **367**, 33 (1996).

[46] I. Robinson, E. Vlieg, and S. Ferrer, Physical Review B **42**, 6954 (1990).

[47] M. Sotto, Surface Science **260**, 235 (1992).

[48] L. Trepte, C. Menzel-Kopp, and E. Menzel, Surface Science **8**, 223 (1967).

[49] P. J. Knight, S. M. Driver, and D. P. Woodruff, Surface Science **376**, 374 (1997).

[50] P. J. Knight, S. M. Driver, and D. P. Woodruff, Chemical Physics Letters **259**, 503 (1996).

[51] A. Chaika and S. Bozhko, JETP Letters **82**, 416 (2005).

[52] S. Murphy, K. Radican, I. V. Shvets, A. N. Chaika, V. N. Semenov, S. S. Nazin, and S. I. Bozhko, Physical Review B **76**, 245423 (2007).

[53] K. Thompson and C. Fadley, Surface Science **146**, 281 (1984).

[54] C. Cohen, A. L'Hoir, J. Moulin, D. Schmaus, M. Sotto, J. L. Domange, and J. C. Boulliard, Surface Science **339**, 41 (1995).

[55] E. Vlieg, S. M. Driver, P. Goedtkindt, P. J. Knight, W. Liu, J. LÃijdecke, K. A. R. Mitchell, V. Murashov, I. K. Robinson, S. A. de Vries, et al., Surface Science **516**, 16 (2002).

[56] D. A. Walko and I. K. Robinson, Surf. Rev. Lett. **6**, 851 (1999).

[57] D. A. Walko and I. K. Robinson, Physical Review B **59**, 15446 (1999).

[58] M. Asensio, M. Ashwin, A. Kilcoyne, D. Woodruff, A. Robinson, T. Lindner, J. Somers, D. Ricken, and A. Bradshaw, Surface Science **236**, 1 (1990).

[59] M. Kittel, M. Polcik, R. Terborg, J. T. Hoeft, P. BaumgÃďrtel, A. M. Bradshaw, R. L. Toomes, J. H. Kang, D. P. Woodruff, M. Pascal, et al., Surface Science **470**, 311 (2001).

[60] W. Liu, K. Wong, H. Zeng, and K. Mitchell, Prog. Surf. Sci. **50**, 247 (1995).

[61] H. Zeng, R. McFarlane, and K. Mitchell, Surface Science **208**, L7 (1989).

[62] A. Atrie, U. Bardi, G. Casalone, G. Rovida, and E. Zanazzi, Vacuum **41**, 333 (1990).

[63] L. H. Dubois and R. G. Nuzzo, Annual Review of Physical Chemistry **43**, 437 (1992).

[64] J. C. Love, L. A. Estroff, J. K. Kriebel, R. G. Nuzzo, and G. M. Whitesides, Chemical Reviews **105**, 1103 (2005).

[65] F. Schreiber, Progress in Surface Science **65**, 151 (2000).

[66] A. Ulman, Chemical Reviews **96**, 1533 (1996).

[67] C. Vericat, M. E. Vela, and R. C. Salvarezza, Physical Chemistry Chemical Physics **7**, 3258 (2005).

[68] R. A. van Delden, M. K. J. ter Wiel, M. M. Pollard, J. Vicario, N. Koumura, and B. L. Feringa, Nature **437**, 1337 (2005).

[69] L. M. Demers, D. S. Ginger, S. J. Park, Z. Li, S. W. Chung, and C. A. Mirkin, Science **296**, 1836 (2002).

[70] T. Otsubo, Y. Aso, and K. Takimiya, Journal of Materials Chemistry **12**, 2565 (2002).

[71] D. P. Woodruff, Physical Chemistry Chemical Physics **10**, 7211 (2008).

[72] N. P. Prince, D. L. Seymour, D. P. Woodruff, R. G. Jones, and W. Walter, Surface Science **215**, 566 (1989).

[73] S. M. Driver and D. P. Woodruff, Surface Science **457**, 11 (2000).

[74] G. S. Parkinson, M. A. M. noz Márquez, P. D. Quinn, M. J. Gladys, D. P. Woodruff, P. Bailey, and T. C. Q. Noakes, Surface Science **598**, 209 (2005).

[75] S. M. Driver and D. P. Woodruff, Langmuir **16**, 6693 (2000).

[76] H. Rieley, G. K. Kendall, A. Chan, R. G. Jones, J. Ludecke, D. P. Woodruff, and B. C. C. Cowie, Surface Science **392**, 143 (1997).

[77] D. P. Woodruff, Journal of Physics-Condensed Matter **6**, 6067 (1994).

[78] A. Ferral, E. M. Patrito, and P. Paredes-Olivera, Journal of Physical Chemistry B **110**, 17050 (2006).

[79] A. Soon, L. Wong, M. Lee, M. Todorova, B. Delley, and C. Stampfl, Surface Science **601**, 4775 (2007).

[80] A. Imanishi, S. Takenaka, T. Yokoyama, Y. Kitajima, and T. Ohta, Journal de Physique IV **7**, 701 (1997).

[81] M. S. Kariapper, C. Fisher, D. P. Woodruff, B. C. C. Cowie, and R. G. Jones, Journal of Physics-Condensed Matter **12**, 2153 (2000).

[82] H. Kondoh, N. Saito, F. Matsui, T. Yokoyama, T. Ohta, and H. Kuroda, Journal of Physical Chemistry B **105**, 12870 (2001).

[83] T. Tsuduki, A. Imanishi, K. Isawa, S. Terada, F. Matsui, M. Kiguchi, T. Yokoyama, and T. Ohta, Journal of Synchrotron Radiation **6**, 787 (1999).

[84] F. Allegretti, F. Bussolotti, D. P. Woodruff, V. Dhanak, M. Beccari, V. D. Castro, M. G. Betti, and C. Mariani, Surface Science **602**, 2453 (2008).

[85] F. Allegretti, D. P. Woodruff, V. R. Dhanak, C. Mariani, F. Bussolotti, and S. D'Addato, Surface Science **598**, 253 (2005).

[86] S. M. Driver and D. P. Woodruff, Surface Science **488**, 207 (2001).

[87] Q. T. Jiang, P. Fenter, and T. Gustafsson, Physical Review B **44**, 5773 (1991).

[88] H. L. Davis and J. R. Noonan, Surface Science **126**, 245 (1983).

[89] S. Walter, V. Blum, I. Hammer, S. Muller, K. Heinz, and M. Giesen, Surface Science **458**, 155 (2000).

[90] C. C. Bahr, J. J. Barton, Z. Hussain, S. W. Robey, J. G. Tobin, and D. A. Shirley, Physical Review B **35**, 3773 (1987).

[91] H. C. Zeng, R. A. McFarlane, and K. A. R. Mitchell, Canadian Journal of Physics **68**, 353 (1990).

[92] H. C. Zeng, R. A. McFarlane, and K. A. R. Mitchell, Physical Review B **39**, 8000 (1989).

[93] E. Vlieg, I. K. Robinson, and R. McGrath, Physical Review B **41**, 7896 (1990).

[94] Q. T. Jiang, P. Fenter, and T. Gustafsson, Physical Review B **42**, 9291 (1990).

[95] H. Grönbeck, A. Curioni, and W. Andreoni, Journal of the American Chemical Society **122**, 3839 (2000).

[96] H. Sellers, A. Ulman, Y. Shnidman, and J. Eilers, Journal of the American Chemical Society **115**, 9389 (1993).

[97] M. Tachibana, K. Yoshizawa, A. Ogawa, H. Fujimoto, and R. Hoffmann, Journal of Physical Chemistry B **106**, 12727 (2002).

[98] Y. Yourdshahyan, H. K. Zhang, and A. M. Rappe, Physical Review B **63**, 081405 (2001).

[99] J. Gottschalck and B. Hammer, Journal of Chemical Physics **116**, 784 (2002).

[100] T. Hayashi, Y. Morikawa, and H. Nozoye, Journal of Chemical Physics **114**, 7615 (2001).

[101] M. C. Vargas, P. Giannozzi, A. Selloni, and G. Scoles, Journal of Physical Chemistry B **105**, 9509 (2001).

[102] Y. Akinaga, T. Nakajima, and K. Hirao, Journal of Chemical Physics **114**, 8555 (2001).

[103] Y. Morikawa, T. Hayashi, C. C. Liew, and H. Nozoye, Surface Science **507**, 46 (2002).

[104] H. Kondoh, M. Iwasaki, T. Shimada, K. Amemiya, T. Yokoyama, T. Ohta, M. Shimomura, and S. Kono, Physical Review Letters **90**, 066102 (2003).

[105] M. G. Roper, M. P. Skegg, C. J. Fisher, J. J. Lee, V. R. Dhanak, D. P. Woodruff, and R. G. Jones, Chemical Physics Letters **389**, 87 (2004).

[106] P. Maksymovych, D. C. Sorescu, and J. J. T. Yates, Physical Review Letters **97**, 146103 (2006).

[107] M. Yu, N. Bovet, C. J. Satterley, S. Bengio, K. R. J. Lovelock, P. K. Milligan, R. G. Jones, D. P. Woodruff, and V. Dhanak, Physical Review Letters **97**, 166102 (2006).

[108] F. P. Cometto, P. Paredes-Olivera, and V. A. M. E. M. Patrito, Journal of Physical Chemistry B **109**, 21737 (2005).

[109] H. Grönbeck and H. Häkkinen, Journal of Physical Chemistry B **111**, 3325 (2007).

[110] A. Chaudhuri, D. C. Jackson, T. J. Lerotholi, R. G. Jones, T. L. Lee, B. Detlefs, and D. P. Woodruff, Physical Chemistry Chemical Physics **12**, 3229 (2010).

[111] D. C. Jackson, A. Chaudhuri, T. J. Lerotholi, D. P. Woodruff, R. G. Jones, and V. R. Dhanak, Surface Science **603**, 807 (2009).

[112] A. Chaudhuri, M. Odelius, R. G. Jones, T. L. Lee, B. Detlefs, and D. P. Woodruff, Journal of Chemical Physics **130**, 124708 (2009).

[113] A. Chaudhuri, T. J. Lerotholi, D. C. Jackson, D. P. Woodruff, and V. Dhanak, Physical Review Letters **102**, 126101 (2009).

[114] A. Chaudhuri, T. J. Lerotholi, D. C. Jackson, D. P. Woodruff, and V. R. Dhanak, Surface Science **604**, 227 (2010).

[115] H. Grönbeck and M. Odelius, Physical Review B **82**, 085416 (2010).

[116] O. Voznyy, J. J. Dubowski, J. J. T. Yates, and P. Maksymovych, Journal of the American Chemical Society **131**, 12989 (2009).

[117] F. Li, L. Tang, W. Zhou, and Q. Guo, Journal of the American Chemical Society **132**, 13059 (2010).

[118] N. A. Kautz and S. A. Kandel, Journal of the American Chemical Society **130**, 6908 (2008).

[119] F.-S. Li, W. Zhou, and Q. Guo, Physical Review B **79**, 113412 (2009).

[120] J. V. Barth, H. Brune, G. Ertl, and R. J. Behm, Physical Review B **42**, 9307 (1990).

[121] U. Harten, A. M. Lahee, J. P. Toennies, and C. Woll, Physical Review Letters **54**, 2619 (1985).

[122] K. G. Huang, D. Gibbs, D. M. Zehner, A. R. Sandy, and S. G. J. Mochrie, Physical Review Letters **65**, 3313 (1990).

[123] G. S. Parkinson, A. Hentz, P. D. Quinn, A. J. Window, D. P. Woodruff, P. Bailey, and T. C. Q. Noakes, Surface Science **601**, 50 (2007).

[124] A. N. Collins, G. N. Seldrake, and J. Crosby, *Chirality in industry: the commercial manufacture andapplications of optically active compounds* (John Wiley & Sons, 1992).

[125] R. Raval, Cattech **5**, 12 (2001).

[126] S. M. Barlow and R. Raval, Surface Science Reports **50**, 201 (2003).

[127] M. O. Lorenzo, C. J. Baddeley, C. Muryn, and R. Raval, Nature **404**, 376 (2000).

[128] R. Raval, Chemical Society Reviews **38**, 707 (2009).

[129] S. M. Barlow, S. Louafi, D. L. Roux, J. Williams, C. Muryn, S. Haq, and R. Raval, Surface Science **590**, 243 (2005).

[130] S. M. Barlow, K. J. Kitching, S. Haq, and N. V. Richardson, Surface Science **401**, 322 (1998).

[131] R. B. Rankin and D. S. Sholl, Surface Science **574**, L1 (2005).

[132] D. I. Sayago, M. Polcik, G. Nisbet, C. L. A. Lamont, and D. P. Woodruff, Surface Science **590**, 76 (2005).

[133] S. Haq, A. Massey, N. Moslemzadeh, A. Robin, S. M. Barlow, and R. Raval, Langmuir **23**, 10694 (2007).

[134] S. Haq, A. Massey, N. Moslemzadeh, A. Robin, S. M. Barlow, and R. Raval (2010), *in preparation*.

[135] M. Copel, T. Gustafsson, W. R. Graham, and S. M. Yalisove, Physical Review B **33**, 8110 (1986).

[136] J. C. Love, D. B. Wolfe, M. L. Chabinyc, K. E. Paul, and G. M. Whitesides, Journal of the American Chemical Society **124**, 1576 (2002).

[137] H. Sellers, Surface Science **264**, 177 (1992).

[138] J. C. Love, D. B. Wolfe, R. Haasch, M. L. Chabinyc, K. E. Paul, G. M. Whitesides, and R. G. Nuzzo, Journal of the American Chemical Society **125**, 2597 (2003).

[139] S. Speller, T. Rauch, J. Bomermann, P. Borrmann, and W. Heiland, Surface Science **441**, 107 (1999).

[140] P. J. Rous, M. A. V. Hove, and G. A. Somorjai, Surface Science **226**, 15 (1990).